

Idiopathic pulmonary fibrosis: quantitative methods to compare structure and function to the normal lung

Yuwen Zhang

A thesis submitted in fulfilment of the requirements for the degree of Doctor of
Philosophy in Bioengineering.

This thesis is for examination purposes only and is confidential to the examination
process.

Auckland Bioengineering Institute

The University of Auckland

2018

Abstract

Idiopathic pulmonary fibrosis (IPF), the most aggressive and frequent form of idiopathic interstitial pneumonias (IIPs), is a chronic and life-threatening disease of unknown cause. It is characterised by progressive worsening of dyspnea and other lung function and is associated with a poor prognosis. IPF occurs primarily in middle-aged and elderly adults, and is more frequent in males than females. Even worse, the aetiology of IPF remains elusive, and its progression is variable and unpredictable, hence there are no biomarkers that can indicate the likely progression of the disease. A quantification scheme that allows recognition of disease consistently across radiology, pulmonary and pathology disciplines remains difficult. In this study, a combination of quantitative information extracted from high resolution computed tomography (HRCT), clinical knowledge, and computational modelling was used to help develop a better understanding of the progression of IPF.

First, an automatic lung lobe segmentation method from HRCT images was developed, which is guided by a statistical shape model that can predict the likely region of fissure locations. This new method was able to estimate the fissure location in 100% of cases including both normal healthy and IPF subjects, whereas two comparison segmentation softwares that use anatomy-based methods fail in several cases. Second, tissue abnormalities in a cohort of IPF lungs were classified, and then mapped to a statisti-

cal shape model, and quantitative approaches were used to analyse lung shape, tissue density, tissue volume, the spatial distribution of abnormalities, and regional changes in tissue over time. Fibrosis was found to present predominantly basally and peripherally in the lung. In contrast, emphysema in these subjects was mostly located in the upper lobes. The first principal statistical shape mode (explaining > 20% of the shape variation in normal lungs) is significantly different between IPF and normal and is strongly correlated with fibrosis extent in IPF. Finally, a computational model of lung function was developed which integrates quantification analysis from volumetric CT and pulmonary function test data to understand differences between IPF and normal older lungs. Ventilation (\dot{V}), perfusion ((\dot{Q})) and gas exchange models were parameterized to simulate \dot{V} and \dot{Q} distributions and O_2 and CO_2 exchange. The computational model can reasonably predict the patient-specific ventilation, perfusion and gas exchange in IPF lung, and quantify the difference of lung function between IPF patients and older normal people. However, abnormalities on volumetric CT imaging may be not able to provide enough information to explain the decline of lung function in IPF patient, and an individual impaired gas exchange appears to happen in not only abnormally tagged region but also in CT-visualized 'normal' tissues.

IPF is a complex and progressive disease that has multifarious physiological processes and significant individual differences. The methods and models presented in this thesis provide a basis for application to research in IPF lung function, and furthers investigations into the underlying relationship between physiological mechanisms and disease progression of IPF.

Acknowledgements

I would like to use this opportunity to express my gratitude to everyone who contributed to this research and supported me throughout my PhD.

First and foremost, I would like to express my sincere gratitude to my supervisor Professor Merryn Tawhai, Dr Alys Clark and Dr Haribalan Kumar for the tremendous patience, motivation, enthusiasm, and immense knowledge. Their continuous guidance helped me in all the time of research and writing of this thesis. This thesis would not be completed without their valuable advice and unfailing trust. It is my great honour to be their student and to have worked under their supervision.

I would like to thank Brian Bartholmai from Mayo Clinic for providing CALIPER classification data, and thank Dr David Milne and Dr Margaret Wilsher from Auckland Hospital for providing the CT image data of IPF patients. Without their constant assistance, this research would not have been possible.

I am also great thankful for the amazing people of lung and placenta groups: Mahyar, Hamed, Zay, Amir, Luca, Behdad, Toby, Kelly, Kerry, Rojan, Win, Mabelle and Izza. My special thanks goes to my lovely friends: Nancy, Wendy and Si. Thank you for giving me so much help, warm and happiness during my PhD.

A big thank to my family for supporting me spiritually throughout my life. Last but not the least, my deepest gratitude to my beloved husband, Xinjian. Thanks for

accompanying me, encouraging me, supporting me and loving me. Words would never say how grateful I am to you. Thank you!

Table of Contents

Abstract	iv
Acknowledgement	vi
Table of Contents	ix
List of Figures	xvii
List of Tables	xx
List of Abbreviations	xxiii
1 Introduction	1
1.1 Motivation	1
1.2 Thesis objectives	2
1.3 Thesis overview	3
2 Background	7
2.1 Introduction to idiopathic pulmonary fibrosis	7
2.1.1 Definition	7
2.1.2 Disease classification	8

2.2	Epidemiology, etiology and pathogenesis	10
2.2.1	Epidemiology	10
2.2.2	Pathogenesis and potential contributors to aetiology	10
2.3	Diagnosis	12
2.3.1	Clinical presentations	13
2.3.2	Radiographic features	14
2.3.3	Histopathology	15
2.3.4	Diagnostic criteria	17
2.4	Clinical course	19
2.4.1	Slow and rapid progressive course	20
2.4.2	Acute exacerbations of IPF	20
2.5	Complications and comorbidities	21
2.5.1	IPF and emphysema	22
2.5.2	IPF and pulmonary hypertension	23
2.6	Physiological alterations	24
2.6.1	Alterations in the mechanical properties of the lung	24
2.6.2	Alterations in pulmonary gas exchange	29
2.7	Summary	32
3	Pulmonary lobar segmentation from CT scans	35
3.1	Background	36
3.1.1	Pulmonary lobar anatomy	36
3.1.2	High resolution computed tomography	37
3.1.3	The importance of pulmonary lobar segmentation	38

3.1.4	Challenges of automatic pulmonary lobar segmentation from CT scans	39
3.2	Review of current published methods for pulmonary lobar segmentation	40
3.2.1	Lung segmentation	41
3.2.2	Fissure detection	47
3.3	Methods: automatic statistical shape model based lobar segmentation method	53
3.3.1	Lung segmentation	55
3.3.2	Statistical finite element models of lung and fissure shape	55
3.3.3	Initial prediction of lobar location in an individual	62
3.3.4	Multi-scale Hessian-based fissure detection	65
3.3.5	Interactive user control interface	72
3.4	Results for SMM segmentation	78
3.4.1	Testing CT dataset	78
3.4.2	Test and results	78
3.5	Discussion	88
3.6	Summary	92
List of References		93

List of Figures

- 2.1 Classification of the interstitial lung diseases. IPF belongs to the family of interstitial lung disease (ILD), and belongs to a subgroup known as idiopathic interstitial pneumonia (IIP) (Troy and Corte, 2012). 9
- 2.2 HRCT images of UIP pattern from two patients. The first is from a woman with progressive cough and dyspnoea, showing her upper (a), lower (b) lung zones and a sagittal plane of the lungs (c). These images show lower lobe-predominant peripheral honeycomb change (b and c, arrows), which is typical of UIP pattern. This patient had no systemic disease or exposures that would exclude idiopathic disease: the diagnosis of IPF is certain. In contrast, the second is a woman with progressive breathlessness, who could be diagnosed with possible IPF. The upper (d), lower (e) lung zones and sagittal image of the lungs (f) demonstrate peripheral, basilar-predominant, reticular densities with traction bronchiectasis (e and f, arrows) consistent with fibrosis. Surgical lung biopsy is suggested. Reproduced from (Martinez et al., 2017). 15

2.3 Surgical lung biopsy specimens of UIP pattern. (A) Scanning power microscopy showing a patchy process with honeycomb spaces (thick arrow), some preserved lung tissue regions (thin arrow), and fibrosis extending into the lung from the subpleural regions. (B) Adjacent to the regions of more chronic fibrosis (arrow) is a fibroblast focus (asterisk), recognized by its convex shape and composition of edematous fibroblastic tissue, suggestive of recent lung injury. Reproduced from (Raghu et al., 2011).	16
2.4 Diagnostic algorithm for IPF. Patients with suspected IPF (i.e., patients with unexplained dyspnea on exertion and/or cough with evidence of ILD) should be carefully evaluated for identifiable causes of ILD. In the absence of an identifiable cause for ILD, an HRCT demonstrating UIP pattern is diagnostic of IPF. In the absence of UIP pattern on HRCT, IPF can be diagnosed by the combination of specific HRCT and histopathological patterns. The accuracy of the diagnosis of IPF increases with multidisciplinary discussion (MDD) among ILD experts. Reproduced from (Raghu et al., 2011).	18
2.5 Schematic representation of potential clinical courses of IPF. A sub-clinical period of disease progression exists during which only radiographic evidence of disease may be noted. This is followed by a symptomatic phase comprising clinical stages (both pre-diagnosis and post-diagnosis). The rate of deterioration and progression to death may be fast (line A), mixed (line B), or slow (lines C and D), with phases of relative disease stability interspersed with acute decline (asterisks). Reproduced from (Ley et al., 2011).	21

3.3 Illustration of the performance of conventional 3D thresholding lung segmentation methods on pathological lungs. Lung borders are not recognized accurately because of the higher densities of the abnormalities compared to the normal tissues. Reproduced from (Van Rikxoort and Van Ginneken, 2013).	45
3.4 (a) Segmented volumes of the vascular tree. There are no large vessels in the vicinity of lobar fissures. (b) Anatomically labeled airway tree showing lobar subtrees. The airway tree can be classified corresponding to five lobes. Reproduced from (Ukil and Reinhardt, 2009).	49
3.5 Flow diagram of the lobar segmentation process.	54
3.6 Lung segmentation result using the common thresholding method. (a) Raw CT image. (b) Segmented lungs.	55
3.7 Finite element modeling of lung lobe shape. (a) Lung surface data extracted from segmented lung masks (purple points for left lung, blue points for right lung). (b) Manual digitized fissure points in 2D sagittal image of right lung (purple points for right oblique fissure, blue points for right horizontal fissure). (c) Manual digitized fissure points shown in 3D (pink points for left oblique fissure, purple points for right oblique fissure, blue points for right horizontal fissure). (d) Lobe shape fitting with lung surface data and digitized fissure data of right lung.	60
3.8 Statistical shape model construction based on principal component analysis. (a) Procrustes aligned meshes of 50 subjects. (b) Average shape model of 50 training subjects. All the weight values are zero for this shape model.	63

3.9 Fissure prediction results compared to ground truth fissure points for one subject. The fissure surface meshes are estimated fissure locations and the red points are manual tracing fissure points by an expert. (a) Left lung. (b) Right lung.	64
3.10 The three eigenvectors of the Hessian matrix representing plane-like structure (fissure). λ_1 and λ_2 are parallel to fissure plane, λ_3 is perpendicular to fissure plane.	69
3.11 The three eigenvectors of the Hessian matrix representing tube-like structure (vessel). λ_1 is parallel to vessel tube, λ_2 and λ_3 are perpendicular to vessel tube.	71
3.12 Hessian-based multiscale fissure detection results. (a) Hessian-based plane-like structure enhancement filter. (b) Remove vessel voxels (tube-like structures). (c) Selected search regions for fissure detection based on SSM initial fissure prediction. (d) 2D and 3D eigenvector based connected component filter. (e) Fissure candidate points. (f) β -spline curve fissure surface fitting.	73
3.13 PTK User interactive interface. It consists of data input section, image visualization section, user plugin section and toolbar section.	75
3.14 Fissure detection results before and after control the search regions. (a) Fissure detection result with a search distance of default 20 voxels. (b) Fissure detection result after setting a specific search distance depending on the accuracy of initial fissure guessing.	76

3.15 Manual correction on automatic fissure detection results (a) Manually select a set of landmarks on real fissure lines shown in raw images to correct automatic fissure detection results (red landmarks are for left oblique fissure, green landmarks are for right oblique fissure, blue landmarks are for right horizontal fissure). (b) Corrected fissure detection results shown with raw images. The corrected fissure lines can match the real fissure locations.	77
3.16 Sagittal, axial, and coronal views illustrating raw image, SSM based initial fissure guessing and final automatic fissure detection results of a normal healthy subject. (a), (d), (g) are sagittal, axial and coronal raw images. (b), (e), (h) are sagittal, axial and coronal SSM based initial fissure guessing results. (c), (f), (i) are sagittal, axial and coronal automatic fissure detection results.	79
3.17 Sagittal, axial, and coronal views illustrating raw image, SSM based initial fissure guessing and automatic fissure detection results of an IPF subject. (a), (d), (g) are sagittal, axial and coronal raw images. (b), (e), (h) are sagittal, axial and coronal SSM based initial fissure guessing results. (c), (f), (i) are sagittal, axial and coronal automatic fissure detection results.	80
3.18 The spatial distribution of error between the gold-standard and semi-automatic methods for three representative subjects, highlighting localized regions of low accuracy.	83

List of Tables

2.1	Alterations of lung function tests in idiopathic pulmonary fibrosis (IPF) Reproduced from (Plantier et al., 2018)	25
3.1	Summary of lung segmentation methods	42
3.2	Summary of fissure detection methods	48
3.3	Summarized demographics for the AGING and HLA datasets.	57
3.4	Possible structures on images in 2D and 3D, and its corresponding eigenvalues λ_k . H and L describe the absolute value of λ_k , H is high, L is low, +/- indicate the sign of the eigenvalue. The eigenvalues relationship here is: $ \lambda_1 \leq \lambda_2 \leq \lambda_3 $.	67
3.5	Summary of interactive user control parameters	74
3.6	Mean error and percentile accuracy of normal healthy and IPF subjects (mean value \pm standard deviation).	82
3.7	Mean error and percentile accuracy of left oblique fissure for each subject	85
3.8	Mean error and percentile accuracy of right horizontal fissure for each subject	86
3.9	Mean error and percentile accuracy of right oblique fissure for each subject	87

3.10 Mean square error (MSE) (mm) and percentile accuracy(%) of seg- mented left oblique (LO), right horizontal (RH), and right oblique (RO) fissures before and after manual correction	88
--	----

List of Abbreviations

FEV₁/FVC ratio of the forced expiratory volume in the one second to the forced vital capacity of the lungs.

ADHB Auckland District Health Board.

AGING human aging cohort.

ATS American Thoracic Society.

CPFE "combined pulmonary fibrosis and emphysema".

CT computed tomography.

DLCO diffusion capacity for carbon monoxide.

DoF degrees of freedom.

DPLD diffuse parenchymal lung diseases.

ERS European Respiratory Society.

FRC functional residual capacity.

FVC forced vital capacity.

GER gastroesophageal reflux.

GPA General Procrustes Alignment.

HDEC Health and Disability Ethics Committees.

HLA Human Lung Atlas.

HRCT high resolution computed tomography.

I-Clic Iowa Comprehensive Lung Imaging Center.

IIP idiopathic interstitial pneumonia.

ILD interstitial lung disease.

IPF idiopathic pulmonary fibrosis.

KCO carbon monoxide transfer coefficient.

PCA principal component analysis.

PFTs pulmonary function tests.

PVV pulmonary vessel volume.

QOL quality of life.

RMS root mean square.

RV pulmonary functional test.

SFeaL Statistical Finite element analysis of Lobe.

SSM statistical shape model.

TLC total lung capacity.

UIP usual interstitial pneumonia.

Chapter 1

Introduction

1.1 Motivation

Idiopathic pulmonary fibrosis (IPF) is a lethal fibrosing lung disorder that typically affects adults in the sixth to seventh decade of life (Meltzer and Noble, 2008; King Jr et al., 2011). IPF is more frequent in males than females, and is associated with environmental factors such as smoking or dust exposure, but as its name suggests does not have a clear aetiology. There is no known cure, although some very new therapies have been suggested to slow the rate of physiologic decline (Raghu et al., 2011). IPF belongs to the family of interstitial lung disease (ILD), and is the most frequently diffuse occurring interstitial lung disease (Meltzer and Noble, 2008). In IPF lungs, healthy tissues are gradually replaced by an abnormal and excessive deposition of collagen (fibrosis), which may lead to a reduction in lung volumes, decreased lung compliance, mismatching of ventilation and perfusion, impaired gas exchange, and ultimately respiratory failure and death (Richeldi et al., 2017).

Diagnosis of IPF relates to a histopathological or radiological pattern typical of usual

interstitial pneumonia (UIP) (Raghu et al., 2011; Xaubet et al., 2017). UIP pattern is usually associated with honeycombing (subpleural cystic airspaces with well-defined walls), reticular opacities and ground-glass abnormalities (Raghu et al., 2011; Richeldi et al., 2017). These abnormalities in IPF typically develop preferentially in the posterior-basal lung regions, and often co-exist with emphysema, which causes a progressive and irreversible decline in lung function. Currently it is not clear how - or whether - the spatial distribution of tissue abnormalities in IPF (including classifications of tissue type) correlate with pulmonary function tests (PFTs). In addition, the progression of IPF is variable between individuals, and no established quantitative tools exist to assess its development and how the tissue abnormality changes over time contribute to lung function. Therefore, developing a computational model of lung function in IPF that can be parameterised to different time points, and presents a potential novel way of investigating strategies for patient-specific diagnosis and treatment planning for IPF patients.

1.2 Thesis objectives

The blood aim of this thesis is to contribute toward developing a new quantitative tool that integrates data from volumetric imaging, PFTs, and computational models for lung function, as a step towards predicting the development of IPF over time, and to understand differences, including lung shape and lung function, between IPF and normal older lungs.

The specific objectives of this thesis are:

Objective 1: Develop an automatic lung lobe segmentation method for HRCT images that can consistently estimate lobar boundaries even if the boundary is not clear along its entire length. The method needs to be tested on both healthy subjects and IPF subjects. Ideally the algorithm will be automatic, or semi-automatic.

Objective 2: Classify and quantify tissue abnormalities from HRCT scans of IPF lungs. Analyse the density, volume, spatial distribution, and their change over time.

Objective 3: Quantify the difference of lung shape between IPF and older normal lungs, and explore the correlation of lung shape change in IPF with the extent of fibrosis.

Objective 4: Integrate the image-based tissue quantification, pulmonary function tests and computational modelling to simulate lung function in IPF, and compare with simulated lung function in older normal people, and use these tools to estimate the impact of radiological features of IPF on lung function.

1.3 Thesis overview

Chapter 2 In order to quantitatively explore the link between structure and lung function of patients with IPF, some background knowledge of this disease is summarized in this chapter. The first part provides a basic introduction to IPF, including its epidemiology, aetiology, pathogenesis, diagnosis, clinical course and comorbidities. The second part describes some physiological alterations in IPF lungs. The changes in the mechanical properties of the lungs in IPF and the changes in pulmonary gas exchange are discussed in detail.

Chapter 3 Automatic identification of pulmonary lobes from imaging is important for image-based analysis of lung function and disease progression. In order to overcome current difficulties in identifying pulmonary fissures, especially in disease, a statistical finite element shape model of the lobes is applied to guide lobar segmentation in this chapter. By deforming a principal component analysis-based statistical shape model (SSM) onto an individual's lung shape, the likely region of fissure locations is predicted to initialize the search region for fissures. Then, an eigenvalue of Hessian matrix analysis and a connected component eigenvector-based analysis are used to determine a set of fissure-like candidate points. A smooth multi-level B-spline curve is fitted to the most fissure-like points (those with high fissure probability) and the fitted fissure plane is extrapolated to the lung boundaries. The method is tested on 20 inspiratory and expiratory CT scans, and compared with existing algorithms in healthy young subjects and older subjects with IPF. This chapter has been published as a conference paper:

- Yuwen Zhang., Mahyar Osanlouy., Alys Clark., Haribalan Kumar., Margaret Wilsher., David Milne., Eric Hoffman., and Merryn Tawhai. (2019, February). Pulmonary lobar segmentation from computed tomography scans based on a statistical finite element analysis of lobe shape. In: SPIE Medical Imaging, International conference. San Diego, USA.

Chapter 4 This chapter details a quantitative analysis of IPF disease features in HRCT scans, including both tissue abnormality quantification and lung lobe shape analysis, to provide consistent tissue-level (distribution of abnormalities) and organ-level (shape) bio-markers that can be used as additional information to track the progression of the disease over time. Lung tissues are classified as normal, reticular, ground glass, or emphysema using CALIPER (Computer-Aided Lung Informatics for Pathology Evalu-

ation and Ratings) software. The classified data is then mapped to a SSM, which allows a reliable comparison between different patients or within one patient at different time points. Quantitative approaches are used to analyse tissue density, tissue volume, the spatial distribution of abnormalities, and regional changes in tissue over time. A principal component analysis (PCA) based SSM is used to understand lung shape differences between IPF and the lungs of normal subjects aged > 50 years through quantifying principal modes of shape variation of both IPF and normal subjects. The results of the chapter have been presented at two conferences:

- Yuwen Zhang., Alys Clark., Haribalan Kumar., Brian Bartholmai, and Merryn Tawhai. (2017, November). Quantitative analysis of idiopathic pulmonary fibrosis abnormality from CT imaging. In: 13th Engineering Mathematics and Applications Conference, International conference. Auckland, New Zealand.
- Yuwen Zhang., Alys Clark., Haribalan Kumar., David Milne., Margaret Wilsher., Brian Bartholmai, and Merryn Tawhai. (2018, March). High resolution CT-based characterization analysis of idiopathic pulmonary fibrosis. In: the Thoracic Society of Australia & New Zealand (TSANZ) conference, International conference. Adelaide, Australia.

Chapter 5 In this chapter, data from volumetric imaging, quantitative tissue-level and shape-level features, and PFTs are integrated to guide a patient-specific computational models of lung function in IPF. In order to compare lung function between IPF patients and normal older controls, for each patient, a subject-specific lung mesh that represents the lung shape of a normal individual with the same age, BMI and pulmonary function data is predicted using an SSM. Anatomically-based models of the airway and blood

vessel trees are generated from the HRCT images, and are matched to both the IPF lung mesh and the corresponding normal control lung mesh. \dot{V} , \dot{Q} and gas exchange models are then used to simulate \dot{V} and \dot{Q} distributions and gas transport in normal and IPF lungs. Part of this chapter has been presented as a conference poster:

- Yuwen Zhang., Alys Clark., Haribalan Kumar., Margaret Wilsher., David Milne., Brian Bartholmai, and Merryn Tawhai. (2018, March). Idiopathic pulmonary fibrosis: a study using volumetric imaging and functional data in a computational lung model, International conference. San Diego, USA.

Chapter 6 Key findings of this thesis are summarized in this chapter, with discussion of the main methods, models and outcomes. Potential future directions that need to be addressed to develop the modelling framework are also discussed.

Chapter 2

Background

To quantitatively explore the link between lung structure and function of patients with idiopathic pulmonary fibrosis (IPF), some background knowledge of the disease is required. This chapter provides an introduction to IPF epidemiology, aetiology, pathogenesis, diagnosis, clinical course, comorbidities, and physiological alterations.

2.1 Introduction to idiopathic pulmonary fibrosis

2.1.1 Definition

Idiopathic pulmonary fibrosis is a chronic, progressive, irreversible, and lethal lung disease of unknown cause. It usually manifests over several years during which progressive scarring occurs in the supporting structural framework (interstitium) of the lung tissue (Meltzer and Noble, 2008; Raghu et al., 2011). It is the scarring of the tissue that is termed fibrosis. This fibrotic condition is generally thought to result from abnormal wound healing after repeated pulmonary tissue damage (King Jr et al., 2011). Several causes of alveolar injury have been implicated in IPF, including cigarette smoke, envi-

ronmental exposure to toxins (e.g. asbestos, avian toxins), gastro-oesophageal reflux, viral infection, and internal mechanisms such as autoimmunity, genomic instability or telomerase length (Raghu et al., 2011; Ahluwalia et al., 2014).

In IPF patients' lungs, some healthy tissues are replaced by altered extracellular matrix and a destroyed alveolar architecture, which leads to decreased lung compliance, disrupted gas exchange, and ultimately respiratory failure and death (Richeldi et al., 2017). The fibrosing areas are generally observed to arise first at the basal and peripheral region of the lungs, and then gradually progress to involve all lung tissues (Martinez et al., 2017). The prominent symptoms of IPF are exercise-induced breathlessness and chronic dry cough (Meltzer and Noble, 2008), which will eventually have a devastating effect on a patient's quality of life (QOL) (Kim et al., 2015). IPF usually affects middle-aged and elderly adults (median age at diagnosis 66 years, range 55-75 years). The disease is isolated to the lungs, and is associated with the radiological and/or histological pattern of UIP (King Jr et al., 2011; Raghu et al., 2011; Xaubet et al., 2017). A typical UIP pattern is usually characterised by 'honeycombing', traction bronchiectasis, and peripheral alveolar septal thickening (Martinez et al., 2017), which will be introduced briefly in Section 2.3.2.

2.1.2 Disease classification

IPF belongs to the family of interstitial lung disease (ILD) or, more accurately, the diffuse parenchymal lung diseases (DPLD). All ILDs result in damage to the lung interstitium, with varying patterns of inflammation and fibrosis. Within the broad category of ILDs, IPF belongs to a subgroup known as idiopathic interstitial pneumonia (IIP) (Meltzer and Noble, 2008). By definition, the aetiology of IIPs is unknown. The

distinction between IPF and other kinds of IIP is particularly important (Corte et al., 2015; Troy and Corte, 2012), as the prognosis for other IIPs is generally much more favourable than that for IPF (Meltzer and Noble, 2008). Over the past decade, IIPs have been classified into seven distinct diseases, differentiated by specific clinical features and pathological patterns, which includes: idiopathic pulmonary fibrosis, non-specific interstitial pneumonia, cryptogenic organising pneumonia, acute interstitial pneumonia, respiratory bronchiolitis-interstitial lung disease, desquamative interstitial pneumonia, and lymphocytic interstitial pneumonia (Katzenstein and Myers, 1998; Troy and Corte, 2012) (Figure 2.1).

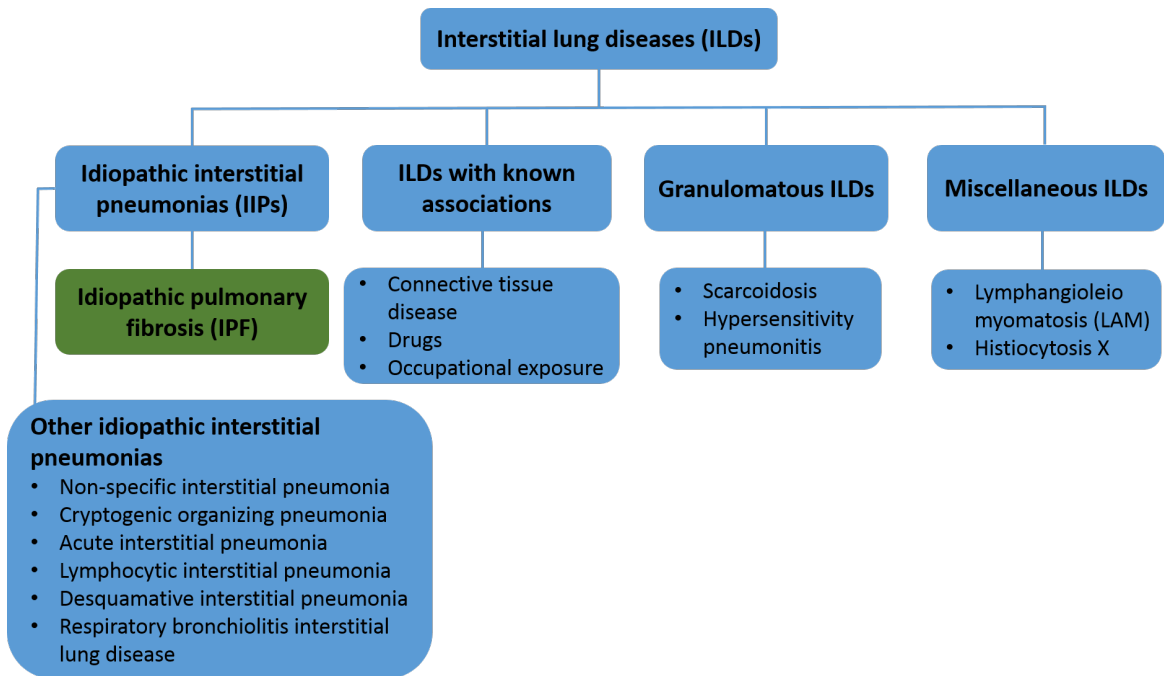


Figure 2.1: Classification of the interstitial lung diseases. IPF belongs to the family of interstitial lung disease (ILD), and belongs to a subgroup known as idiopathic interstitial pneumonia (IIP) (Troy and Corte, 2012).

2.2 Epidemiology, etiology and pathogenesis

2.2.1 Epidemiology

Although IPF is considered a rare disease, this disease is the most common form of IIP (Travis et al., 2013). The incidence of IPF is similar to that of stomach, brain, and testicular cancers and has recently been demonstrated to be rising over time (Richeldi et al., 2017). A cohort study including patients diagnosed with ILDs at Aarhus University Hospital showed that IPF was the most common diagnosis (28%) followed by connective tissue disease-related ILD (14%), hypersensitivity pneumonitis (7%) and non-specific interstitial pneumonia (NSIP) (7%) (Hyldgaard et al., 2014). Although there is little data available estimating worldwide incidence, a recent study showed that in Europe and North America, the prevalence of IPF is estimated to range between 2.8 and 18 cases per 100,000 people per year, and this value might be lower in Asia and South America, where it is estimated to range from 0.5 to 4.2 cases per 100,000 individuals per year (Richeldi et al., 2017). IPF is more likely to affect men than women, and is rare in people younger than 50 years (Raghu et al., 2011, 2006). The incidence is estimated to be 13 cases/100,000 in women and 20 cases/100,000 in men (Xaubet et al., 2017). In addition, the incidence of IPF increases with age (Meltzer and Noble, 2008). The reason that incidence has increased in recent years is most likely because of improved diagnostic methods and increased life expectancy (Xaubet et al., 2017).

2.2.2 Pathogenesis and potential contributors to aetiology

Historically, IPF was considered a chronic inflammatory disorder, which gradually progressed to established fibrosis (Richeldi et al., 2017). Now IPF is generally regarded as

a consequence of multiple interacting factors, in which repetitive local micro-injuries to an ageing alveolar epithelium plays an important role (Richeldi et al., 2017). These micro-injuries initiate aberrant epithelial-fibroblast communication, the induction of matrix-producing myofibroblasts, and considerable extracellular matrix accumulation and remodelling of lung interstitium (Richeldi et al., 2017). Although the aetiology of IPF is unknown, currently, environmental exposures and genetic factors have been supported by some researchers as providing important inducement (Taskar and Coultas, 2006; Meltzer and Noble, 2008; Xaubet et al., 2017; Richeldi et al., 2017). In addition, gastroesophageal reflux (GER), exposure to silica, brass, steel and wood dust, livestock and agriculture work, and the construction of wooden houses are also potential risk factors for the pathogenesis of IPF (Taskar and Coultas, 2006; Xaubet et al., 2017).

Environmental exposures

The relationship between environmental exposures and IPF has been consistently demonstrated by case studies. Asbestosis, for example, is a case in which environmental material is associated with pulmonary fibrosis (Meltzer and Noble, 2008). There are studies indicating that the pathogenesis and progression of IPF are influenced by particulate inhalation, which is supported by the fact that the development of IPF consistently relates to cigarette smoking history in most patients (Baumgartner et al., 1997; Richeldi et al., 2017). Additionally, other environmental factors including metal and wood dusts, agriculture and farming, viruses, and stone and silica have also been proposed (Raghu et al., 2011; Taskar and Coultas, 2006).

Genetic factors

Increasing evidence indicates that genetic predisposition plays an essential part in the development of IPF (Xaubet et al., 2017; Richeldi et al., 2017). This evidence is based on the existence of familial forms of the disease, and it has been shown that around 2.2% to 3% of IPF cases are familial (Xaubet et al., 2017). The most likely mode of genetic transmission of pulmonary fibrosis in familial cases is autosomal-dominant with variable penetrance (Steele et al., 2005; Allam and Limper, 2006; Lee et al., 2005; Musk et al., 1986). Rare genetic variants have been identified in cases where ILDs affect two or more members of the same biological family, including genes associated with alterations in host defence (MUC5B, ATP11A, TOLLIP), telomere maintenance (TERT, TERC, PARN, RTEL, OBFC1), surfactant dysfunction (SFTPC, SFTPA2) and epithelial barrier function (DSP, DPP9) (Alder et al., 2008; Raghu et al., 2011; Seibold et al., 2011; Xaubet et al., 2017). Among them, MUC5B, a promoter site of an airway mucin gene, is the most strongly associated with development of both familial and sporadic IPF (Richeldi et al., 2017). MUC5B encodes a mucin-5B precursor protein that contributes to airway mucous production and might have an important role in lung host defence. It has also been noted that members of the same biological family may be affected by different types of ILDs, such as non-specific interstitial pneumonia and cryptogenic organizing pneumonia (Xaubet et al., 2017).

2.3 Diagnosis

The diagnosis of IPF often requires a multidisciplinary discussion, involving pulmonologists, chest radiologists, and chest pathologists experienced in the field of ILDs (Flaherty et al., 2004; King Jr et al., 2011; Raghu et al., 2011). This multidisciplinary

approach has been accepted in consensus guidelines all over the world and has helped to standardize IPF diagnosis (Raghu et al., 2011; Richeldi et al., 2017). Usually, IPF is diagnosed by identification of a pattern of UIP on the basis of radiological or histological criteria in patients without evidence of an alternative cause. The biggest challenge of diagnosis for clinicians is how to exclude other idiopathic interstitial pneumonias, fibrotic nonspecific interstitial pneumonia, and interstitial lung disease associated with occupational or environmental exposure, connective tissue disease, and drugs (King Jr et al., 2011; Richeldi et al., 2017). This differential diagnosis is really important, since typical UIP is not exclusive to IPF, but may associate with some other conditions, such as chronic hypersensitivity pneumonitis and asbestosis. Many patients have a history of environmental exposures or medical treatments which clinicians need to take into consideration for diagnosis (Richeldi et al., 2017).

2.3.1 Clinical presentations

Patients with IPF usually suffer from unexplained progressive dyspnea on exertion and chronic dry cough, bibasilar inspiratory crackles, and finger clubbing. Bibasilar inspiratory crackles are heard on chest auscultation and finger clubbing is found in about 30% of patients (Raghu et al., 2011; King Jr et al., 2011; Richeldi et al., 2017). Chest pain, fatigue, malaise, and weight loss are also typical symptoms for IPF patients (Douglas et al., 2000; King Jr et al., 2001). These clinical presentations might initially be attributed to ageing or some comorbidities such as cardiovascular disease, or obesity (Richeldi et al., 2017). Therefore, in order to avoid diagnostic delays, it is necessary for primary care physicians to have clinical suspicion of IPF. Some patients may present with acute respiratory exacerbations usually accompanied by fever and

influenza-like symptoms within a few days or weeks from the first clinical symptom. In these cases, clinicians require careful diagnostic distinction from other forms of acute ILDs (Richeldi et al., 2017). Pulmonary function tests (PFTs) from IPF patients usually show a restricted pattern with low percent predicted total lung capacity (TLC) and diffusion capacity for carbon monoxide (DLCO). But for some patients with early disease, PFT results might be normal or mildly abnormal (Douglas et al., 2000; Raghu et al., 2006).

2.3.2 Radiographic features

HRCT of the chest has become an essential tool for the diagnosis of IPF, which is usually associated with identification of a UIP pattern. The presence of UIP pattern on HRCT is characterised by appearance of honeycombing cysts, reticular opacities and ground-glass abnormalities (Figure 2.2) (King Jr et al., 2011; Raghu et al., 2011; Richeldi et al., 2017). Honeycombing is common, and essential for a definite diagnosis (Raghu et al., 2011). On HRCT, honeycombing is presented as clustered cystic airspaces with a typical diameter of 3-10 mm but occasionally as large as 2.5 cm, and in a predominantly subpleural and posterior basal distribution (Hansell et al., 2008; Richeldi et al., 2017). Reticular opacities are often associated with traction bronchiectasis (Nishimura et al., 1992; Johkoh et al., 1999). Ground-glass is a common characteristic of UIP pattern, although it is sometimes less extensive than reticular. The distribution of abnormalities are often basal, peripheral and patchy (Raghu et al., 2011). If patients show micronodules, air-trapping, non-honeycomb cysts, extensive ground glass opacities, consolidation, or a peribronchovascular-predominant distribution, alternative diagnosis should be taken into account (Hwang et al., 2009; Souza et al., 2006). If patients show reticular ab-

normalities located in subpleural and basal regions, but no honeycombing appearance, possible UIP patterns should be taken into consideration, then a surgical lung biopsy is suggested to make a definite diagnosis (Raghu et al., 2011; Richeldi et al., 2017).

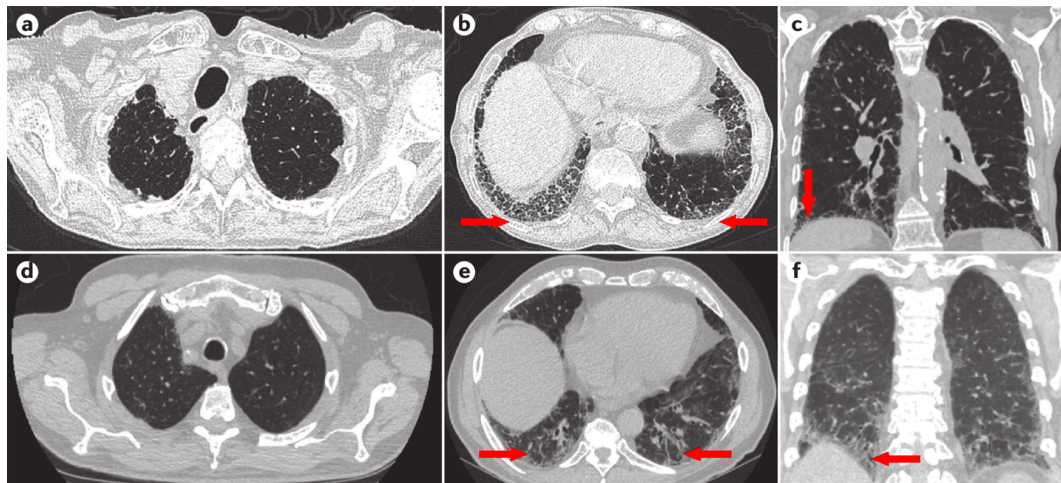


Figure 2.2: HRCT images of UIP pattern from two patients. The first is from a woman with progressive cough and dyspnoea, showing her upper (a), lower (b) lung zones and a sagittal plane of the lungs (c). These images show lower lobe-predominant peripheral honeycomb change (b and c, arrows), which is typical of UIP pattern. This patient had no systemic disease or exposures that would exclude idiopathic disease: the diagnosis of IPF is certain. In contrast, the second is a woman with progressive breathlessness, who could be diagnosed with possible IPF. The upper (d), lower (e) lung zones and sagittal image of the lungs (f) demonstrate peripheral, basilar-predominant, reticular densities with traction bronchiectasis (e and f, arrows) consistent with fibrosis.

Surgical lung biopsy is suggested. Reproduced from (Martinez et al., 2017).

2.3.3 Histopathology

When HRCT features are not enough for a certain diagnosis of IPF, surgical lung biopsy is suggested (Richeldi et al., 2017). The main histopathologic hallmarks of UIP pattern is characterized by a heterogeneous appearance, best seen at low magnification, with areas of subpleural fibrosis and honeycomb (i.e. cystic fibrotic airspaces lined by bronchiolar epithelium and often filled by mucin and variable numbers of inflammatory cells),

alternating with areas of less affected or normal parenchyma (Society et al., 2000; Travis et al., 2002) (Figure 2.3). Small areas of active fibrosis (fibroblast foci) are present in the background of collagen deposition, and they reflect the temporal heterogeneity and indicate current ongoing disease (King Jr et al., 2011). Another feature of UIP pattern is that the inflammation is often absent or mild and consists of a patchy interstitial infiltrate of lymphocytes and plasma cells (Raghu et al., 2011; King Jr et al., 2011). Although surgical lung biopsy is essential for a correct diagnosis, careful consideration is required for every patient to estimate whether the risks of surgical lung biopsy outweigh the potential benefits of the histopathologic information. For older patients with comorbidities or clinically significant physiological impairment, it is suggested to avoid surgical lung biopsy (Richeldi et al., 2017).

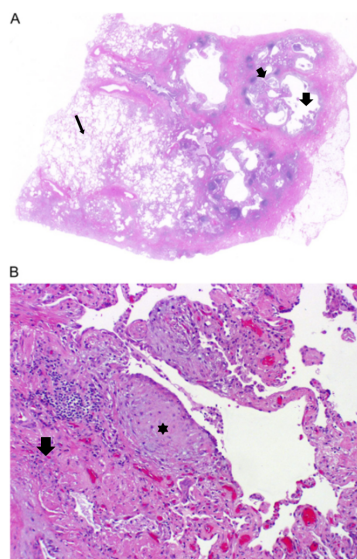


Figure 2.3: Surgical lung biopsy specimens of UIP pattern. (A) Scanning power microscopy showing a patchy process with honeycomb spaces (thick arrow), some preserved lung tissue regions (thin arrow), and fibrosis extending into the lung from the subpleural regions. (B) Adjacent to the regions of more chronic fibrosis (arrow) is a fibroblast focus (asterisk), recognized by its convex shape and composition of edematous fibroblastic tissue, suggestive of recent lung injury. Reproduced from (Raghu et al., 2011).

2.3.4 Diagnostic criteria

”Gold standard” diagnostic criteria for IPF have been developed by the American Thoracic Society (ATS) and the European Respiratory Society (ERS) in a statement of published guidelines (Raghu et al., 2011). These criteria are:

1. Exclusion of other known causes of ILD (e.g. domestic and occupational environmental exposures, connective tissue disease, and drug toxicity).
2. The presence of a UIP pattern on HRCT in patients not subjected to surgical lung biopsy.
3. Specific combinations of HRCT and surgical lung biopsy pattern in patients subjected to surgical lung biopsy.

Beyond that, minor criteria have also been set for the diagnosis of IPF in the absence of a surgical lung biopsy (Raghu et al., 2011):

1. Age > 50 years.
2. Insidious onset of otherwise unexplained dyspnea on exertion.
3. Duration of illness being over 3 months.
4. Bibasilar inspiratory crackles (dry or ”Velcro” type).

Figure 2.4 shows the diagnostic workflow for adult patients with ILD and suspected IPF. If the high-quality HRCT evidence is sufficient enough for the recognition of histopathologic UIP pattern, surgical lung biopsy is not essential (Hunninghake et al., 2001; Raghu et al., 1999; Flaherty et al., 2003; Quadrelli et al., 2010). However,

a multidisciplinary discussion among experienced clinical, radiologic and histopathologic experts is particularly important when the radiologic and histopathologic patterns are discordant (e.g., HRCT is inconsistent with UIP and histopathology suggests UIP) (Raghu et al., 2011). Radiologic or pathologic UIP pattern is not 100% specific to IPF (Lynch et al., 2006; Trahan et al., 2008; Silva et al., 2008a).

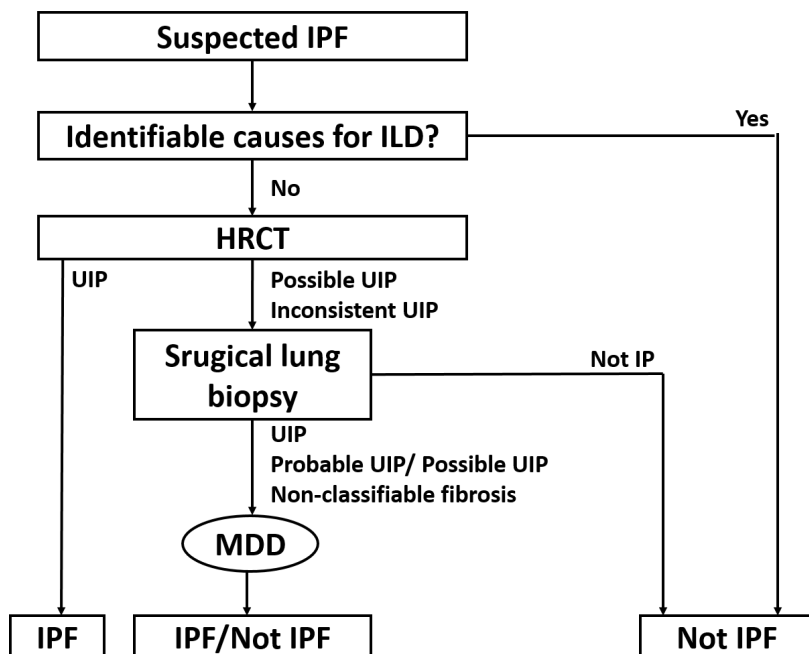


Figure 2.4: Diagnostic algorithm for IPF. Patients with suspected IPF (i.e., patients with unexplained dyspnea on exertion and/or cough with evidence of ILD) should be carefully evaluated for identifiable causes of ILD. In the absence of an identifiable cause for ILD, an HRCT demonstrating UIP pattern is diagnostic of IPF. In the absence of UIP pattern on HRCT, IPF can be diagnosed by the combination of specific HRCT and histopathological patterns. The accuracy of the diagnosis of IPF increases with multidisciplinary discussion (MDD) among ILD experts. Reproduced from (Raghu et al., 2011).

2.4 Clinical course

Some studies indicate that IPF patients have median survival time between two and three years from the time of diagnosis (Bjoraker et al., 1998; Flaherty et al., 2002; Nicholson et al., 2000; Rudd et al., 2007; KING JR et al., 2001; King Jr et al., 2011). For most IPF patients, the clinical course has been described as a general decline in pulmonary function until eventual death from respiratory failure or complicating comorbidity (Carrington et al., 1978; Tukiainen et al., 1983; Gross and Hunninghake, 2001), however, the individual disease progression can be highly variable (Kim et al., 2006b; Meltzer and Noble, 2008). It appears that there are several possible clinical courses for patients with IPF (shown in Figure 2.5) (Raghu, 1987): slow and gradual progression over many years (the most common) (Ryu et al., 2014; Meltzer and Noble, 2008; Raghu et al., 2011); rapid and accelerated decline (Kim et al., 2006b; Selman et al., 2007); and acute exacerbations (King Jr et al., 2011; Xaubet et al., 2017). It is difficult to predict the natural history of disease progression for a given patient at the time of the diagnosis (Raghu et al., 2011). Whether the different clinical courses are influenced by geographic, ethnic, cultural, racial, or other factors remains unknown. But some evidence has been suggested that worsening prognosis may be associated with older people (> 70 years old), smoking history, low body mass index (BMI), severe physiological impairment, and large radiological extent of disease (Ley et al., 2011). Other comorbidities such as emphysema and pulmonary hypertension may also have an impact on the disease course (Mejía et al., 2009; Wells et al., 2003; Lettieri et al., 2006). While prediction of the likely course of disease is currently not possible, it would be very beneficial to enable clinicians to make an appropriate and optimal treatment plan as early as possible.

2.4.1 Slow and rapid progressive course

Most IPF patients deteriorate relatively slowly, and their pulmonary function usually decreases gradually over months to years after the first clinical symptoms (cough and progressive dyspnoea) (Ryu et al., 2014; Meltzer and Noble, 2008; Raghu et al., 2011). Patients usually experience reduction of lung volumes, and hypoxaemia at rest that worsens with exercise. This is accompanied by a decline of forced vital capacity (FVC) by a mean of 0.13 L to 0.21 L per year (Ley et al., 2011). In contrast, a subgroup of patients with IPF, mainly male cigarette smokers, experience a rapid worsening of symptoms, and insufficiency of pulmonary function (Kim et al., 2006b; King Jr et al., 2011), known as accelerated IPF. The patients with rapid progression have reduced survival time relative to those with a slowly progressive clinical course.

2.4.2 Acute exacerbations of IPF

“Acute exacerbation” was first proposed by Japanese physicians to describe acute, unexpected worsening of respiratory functions and severe hypoxaemia in patients with IPF, without a clear trigger (Kondoh et al., 1993; Gross, 1962). The rapid deterioration occurs in a small minority of patients with IPF (about 5-10%), with absence of infection, heart failure, pneumothorax, or pulmonary embolism (Azuma et al., 2005; King Jr et al., 2011; Raghu et al., 2011). The prognosis for patients with acute exacerbations is poor, and it may happen at any stage in the course of IPF (Kim et al., 2006a; Parambil et al., 2005; Sakamoto et al., 2009; Kondoh et al., 2010). Patients with acute exacerbation usually experience poor respiratory decline, worsened cough, fever and increased sputum production (Ambrosini et al., 2003; Kim et al., 2006a). The mortality rate for patients with acute exacerbations is over 60% (Wootton et al., 2011; Lettieri et al., 2006); for

cases requiring mechanical ventilation, the mortality is close to 100% (King Jr et al., 2011; Xaubet et al., 2017).

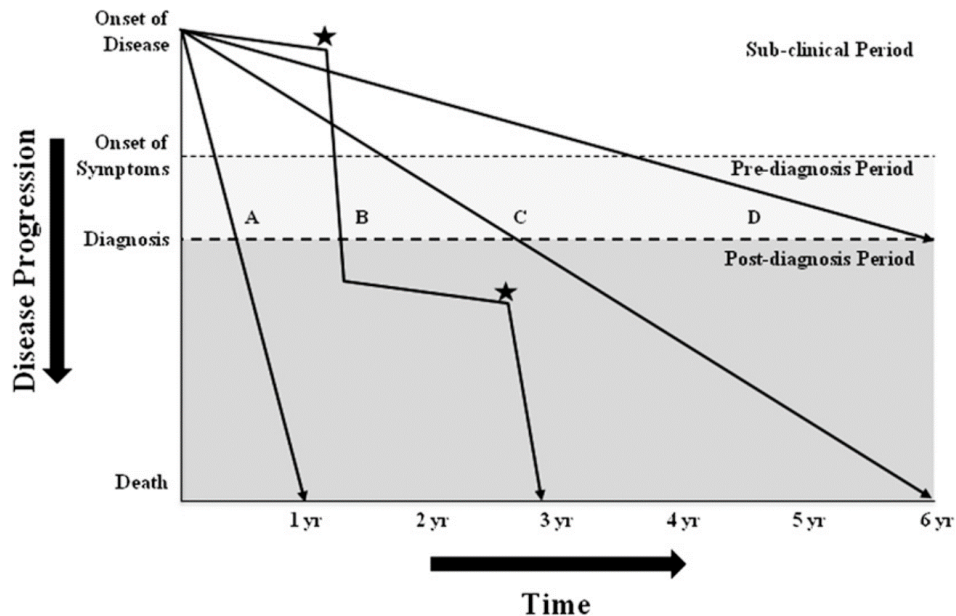


Figure 2.5: Schematic representation of potential clinical courses of IPF. A sub-clinical period of disease progression exists during which only radiographic evidence of disease may be noted. This is followed by a symptomatic phase comprising clinical stages (both pre-diagnosis and post-diagnosis). The rate of deterioration and progression to death may be fast (line A), mixed (line B), or slow (lines C and D), with phases of relative disease stability interspersed with acute decline (asterisks). Reproduced from (Ley et al., 2011).

2.5 Complications and comorbidities

Complications and comorbidities can occur in patients with IPF that may influence the clinical course and prognosis (Xaubet et al., 2017; King and Nathan, 2017; Martinez et al., 2017). It is reported that only 12% of patients with IPF have no comorbid illness, and most patients have comorbidities (Raghu et al., 2011; Kim et al., 2015; Harari et al., 2016; Kreuter et al., 2016). Emphysema and pulmonary hypertension are both important

comorbid conditions in IPF patients (Raghu et al., 2015; Martinez et al., 2017), and are briefly outlined here.

2.5.1 IPF and emphysema

Several research groups have described a syndrome in which IPF coexists with pulmonary emphysema (Wells et al., 1997, 2003; Cottin et al., 2005; Meltzer and Noble, 2008). In 2005, Cottin et al. (2005) presented a syndrome named "combined pulmonary fibrosis and emphysema" (CPFE). Both IPF and emphysema are associated with a significant smoking history, and CPFE is strongly associated with exercise hypoxaemia, severe dyspnea on exertion, upper lobe emphysema and lower lobe fibrosis, unexpected subnormal lung volumes, and severe reduction of carbon monoxide transfer (Silva et al., 2008b; Mejía et al., 2009; Cottin et al., 2010; King Jr et al., 2011; Lin and Jiang, 2015). Currently, whether CPFE is a distinct clinical entity or not remains unknown, i.e. whether this is just the presence of two different diseases running in parallel is unclear (King Jr et al., 2011; Lin and Jiang, 2015). Some researchers suggest that CPFE should be regarded as a distinct clinical entity, since it has a characteristic pulmonary function feature and unique natural history that is different from pure emphysema or IPF alone (Cottin et al., 2005; Lin and Jiang, 2015; Xaubet et al., 2017). CPFE occurs more frequently in males than in females and its prevalence is about 30% to 47% in patients with IPF (Xaubet et al., 2017). It is often associated with a significant drop of DLCO and severe hypoxaemia during exercise due to the additive effect of emphysema and fibrosis (Xaubet et al., 2017).

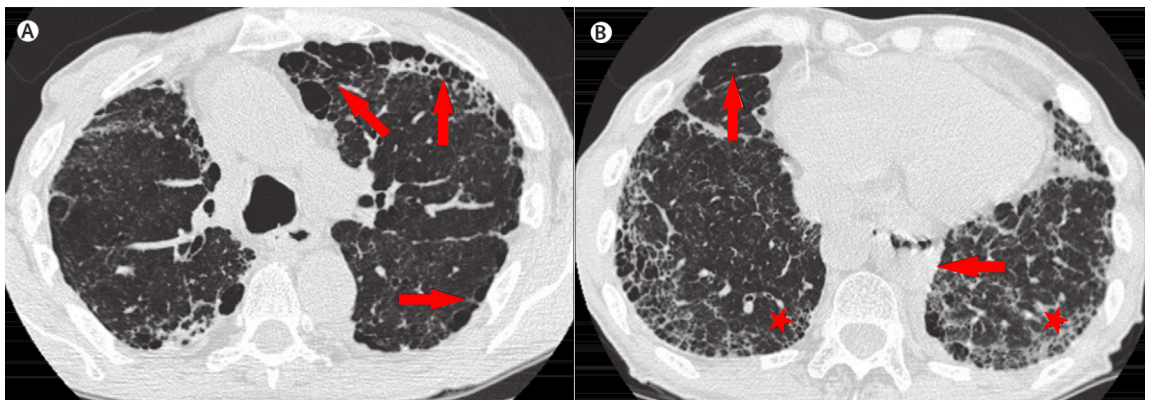


Figure 2.6: Combined pulmonary fibrosis and emphysema. High-resolution CT shows emphysematous lesions (arrows) in the upper lobes (in Figure A), emphysema (arrow) and usual interstitial pneumonia-like lesions (stars) in the lower lobes (in Figure B). Reproduced from (King Jr et al., 2011).

2.5.2 IPF and pulmonary hypertension

Pulmonary hypertension (PH), defined as a mean pulmonary artery pressure of > 25 mmHg at rest, is a frequent form of comorbid condition in patients with IPF and is the main determinant of poor prognosis (Raghu et al., 2011; Xaubet et al., 2017). It is estimated that the incidence of pulmonary hypertension is around 30% to 50% in IPF patients (King and Nathan, 2017). In general, pulmonary hypertension occurs due to several factors, with chronic hypoxia-induced vasoconstriction and destruction of the pulmonary capillary bed induced by fibrosis being the two main causes (Hayes Jr et al., 2016). The presence and development of pulmonary hypertension is associated with significant dyspnea, functional impairment (particularly in DLCO) and decreased exercise capacity, and may increase risk of mortality for patients with IPF (Mejía et al., 2009; Lettieri et al., 2006; Nadrous et al., 2005). Some studies have shown that combined pulmonary fibrosis and pulmonary hypertension has a significantly negative effect on the survival in patients with IPF alone, probably caused by the increased pulmonary

vascular resistance (Raghu et al., 2011; King Jr et al., 2011). Currently, whether IPF with pulmonary hypertension represents a distinct clinical entity (IPF–PH) is still unclear (Raghu et al., 2011).

2.6 Physiological alterations

The clinical presentation of IPF is related to a number of physiological alterations of the lung (Crystal et al., 1976; Plantier et al., 2018). These alterations have a complex and negative impact on all compartments of the respiratory system, from lung volume and compliance to gas exchange, from conducting airways to lung vasculature (Plantier et al., 2018). In general, patients with IPF usually have reduced lung volumes, reduced lung compliance, reduced diffusing capacity, increased ratio of the forced expiratory volume in the one second to the forced vital capacity of the lungs (FEV₁/FVC), and arterial hypoxaemia that worsens with exercise (Crystal et al., 1976; Society et al., 2000; Cortes-Telles et al., 2014; Plantier et al., 2018). These alterations in lung physiology are summarized in Table 2.1.

2.6.1 Alterations in the mechanical properties of the lung

Reduction in lung compliance

IPF disease often results in reduction in lung compliance (i.e. an increase in lung tissue stiffness). Studies have shown that the reduced lung compliance is caused by a reduction in the compliance of the lung extracellular matrix and by alterations in pulmonary surfactant (Plantier et al., 2018). In patients with IPF, surfactant shows alterations in its lipid profile (Gunther et al., 1999; Schmidt et al., 2002), which leads to severely im-

Table 2.1: Alterations of lung function tests in IPF Reproduced from (Plantier et al., 2018)

	Mild IPF	Moderate to severe IPF
Static lung volumes		
- TLC	Normal	Decreased
- FRC	Normal	Decreased
Spirometry		
- FVC	Normal	Decreased
- FEV ₁ /FVC	Normal or increased	Normal or increased
Airways		
- Cough reflex	Increased	Increased
- Airway resistance	Decreased	Decreased
Blood gases at rest		
- P_aO_2	Normal	Decreased
- P_aCO_2	Normal	Decreased
Carbon monoxide transfer		
- DLCO	Decreased	Decreased
- V_A	May be normal	Decreased
- K_{CO}	May be normal	Decreased
Exercise physiology		
- Peak V_{O_2}	May be normal	Decreased
- V_D/V_T	Increased	Increased
- V_E/V_{CO_2}	Increased	Increased
- PAP at exercise	Increased	Increased
- $P_{A-a}O_2$ at exercise	Increased	Increased
Pulmonary haemodynamics at rest		
- PAP	May be increased	Frequently increased
- PCWP	Normal	May be increased

FVC: forced vital capacity; FEV₁ : forced expiratory volume in 1 s; TLC: total lung capacity; FRC: functional residual capacity; P_aO_2 : arterial oxygen tension; P_aCO_2 : arterial carbon dioxide tension; DLCO : diffusing capacity of the lung for carbon monoxide; V_A : alveolar volume; K_{CO} : transfer constant of carbon monoxide; PAP: pulmonary artery pressure; PCWP: pulmonary capillary wedge pressure; V_{O_2} : oxygen uptake; V_D/V_T : ratio of dead space volume to tidal volume; V_E/V_{CO_2} : ratio of minute ventilation to carbon dioxide elimination; $P_{A-a}O_2$: alveolar–arterial oxygen tension difference.

paired surface activity (Gunther et al., 1999). The reduction in lung compliance may happen from an early stage of IPF (Plantier et al., 2018). A study of 31 IPF patients from (Zielonka et al., 2010) showed that the static lung compliance was consistently and significantly reduced (by $44 \pm 6\%$). A similar result was found by in another study (Orens et al., 1995), where all of the measured IPF patients had abnormal static lung compliance, which suggests that measurement of lung compliance could help with the early diagnosis of IPF.

The alterations of lung compliance in IPF patients appear to be strongly correlated with the degree of lung fibrosis as assessed by scoring of lung biopsies (Fulmer et al., 1979; Plantier et al., 2018). Nava and Rubini (1999) measured the dynamic lung compliance in seven patients with end-stage IPF, which showed that the reduction in lung compliance may be correlated with the progress of the disease. Currently, whether the reductions in lung compliance relate to clinical presentations (e.g. dyspnoea) remains unclear, but it is highly likely that the lung compliance has a strong relationship with the respiratory muscles and thus has an impact on the work of breathing (Plantier et al., 2018). In addition, as the distribution of disease is heterogeneous in IPF lungs, lung compliance is expected to be uneven between different lung regions (Organ et al., 2015), but more evidence is needed to understand the implications of disease distribution outcomes.

Reduction of lung volumes

The restriction of lung volumes (total lung capacity (TLC), functional residual capacity (FRC), forced vital capacity (FVC), and pulmonary functional test (RV)) is typical in patients with IPF. This restriction of lung volumes often occurs at some time point in the clinical course of IPF (Society et al., 2000; Plantier et al., 2018). However, some-

times lung volumes may be normal in the early stage of IPF, especially for patients with superimposed chronic obstructive pulmonary disease (Martinez and Flaherty, 2006). Cherniack et al. (1995) studied 96 patients with biopsy-confirmed IPF. The range of TLC was from 42% to 125% predicted and the range of FVC was from 26% to 112% predicted. A reduction in lung volumes consistently relates to an increased risk of death (Martinez and Flaherty, 2006), and is weakly associated with dyspnoea or quality of life (Du Bois et al., 2011). However, whether the reduced lung volumes reflects the disease progression of IPF is still unknown (Plantier et al., 2018). Interestingly, patients with CPFE have higher RV and TLC compared to the patients with IPF alone (Mura et al., 2006), which may be caused by the effects of comorbid pulmonary emphysema on lung compliance (Doherty et al., 1997).

Alterations in the conducting airways

Some evidence suggests that alterations also occur in conducting airways in patients with IPF, including increased airway epithelial cell proliferation (Vuorinen et al., 2008) and differentiation (Plantier et al., 2016), and increased numbers of visible bronchioles in the distal regions (Chilosi et al., 2002). A reduction in conducting airway resistance was found in IPF lungs compared with normal, which may contribute to an increased ratio of FEV_1 to FVC (Pastre et al., 2015). Plantier et al. (2016) used volumetric capnography to estimate the volume of conducting airways in patients with IPF, patients with other ILDs, and healthy people. The results showed that conducting airway volume was significantly higher in IPF lungs in comparison with non-IPF ILD lungs and healthy lungs. However, this change in airway volume was not associated with the severity of alveolar lesions, dyspnea, cough or quality of life (Plantier et al., 2016). The increase in airway volume in IPF may reflect dilation of airways consistent with bronchiectasis that

can be characteristic of this disease, and a commonly accepted view is that bronchiectasis in IPF may be caused by fibrotic retraction of peribronchiolar alveolar attachments and subsequent airway dilation (Sumikawa et al., 2008). However, a recent study found that bronchiectasis had a weak relationship with total fibrosis extent observed from CT imaging (Walsh et al., 2015), which means the remodelling of conducting airways in IPF may be dissociated from alveolar fibrosis (Plantier et al., 2016). Patients with IPF usually have more rapid breaths with the progression of disease (Kornbluth and Turino, 1980; Renzi et al., 1982), and have a relatively increased flow rate in the conducting airways due to the increased static elastic recoil (Society et al., 2000). Additionally, it has been suggested that at least part of the ventilation abnormalities seen in IPF is associated with small airways disease with peribronchiolar fibrosis and inflammation, and 70% of IPF patients have narrowed small airways (Crystal et al., 1976).

Alterations in the lung vasculature

Vascular lesions are observed in the pulmonary vasculature in patients with IPF, and often lead to disproportionate increases in the pulmonary vascular resistance and pulmonary hypertension (Plantier et al., 2018). The tissues adjacent to the areas of fibrosis have been shown to have an increase in vessel profusion, whereas the fibrotic tissue itself demonstrates a reduced number of blood vessels (Cosgrove et al., 2004; Ebina et al., 2004). Jacob et al. (2016a) explored the relationship between pulmonary vessel volume (PVV) and ILD extent (includes ground glass, reticular and honeycomb patterns). It was found that PVV had a strong relationship with ILD extent ($R^2 = 0.73$, $P < 0.0001$) when using linear regression analysis. Furthermore, PVV was demonstrated to be an independent predictor of mortality, and a stronger predictor of mortality than all the other traditional CT features and pulmonary functional variables (Jacob et al., 2016a).

The increase in PVV seen in more advanced fibrosis may be caused by the vascular capacitance of spared lung (the upper and middle lobes in patients with IPF, which is a predominantly basal disease), and may also relate to the increased negative intrathoracic pressure which non-compliant fibrotic lungs need to generate during inspiration (Jacob et al., 2016b).

2.6.2 Alterations in pulmonary gas exchange

IPF is associated with multiple pathophysiological changes in pulmonary gas exchange. The lesions of the alveolar-capillary membrane in IPF lungs will impair both the diffusion capacity and ventilation/perfusion (V/Q) relationship, increase dead space ventilation and alveolar-arterial oxygen tension difference ($P_{A-a}O_2$), and finally cause chronic arterial hypoxaemia (Crystal et al., 1976; Plantier et al., 2018; Society et al., 2000).

Reduced diffusing capacity of the lung

The diffusing capacity of oxygen is considered to be reduced in almost all patients with IPF. However, in clinical examination, this diffusing capacity is technically very difficult to measure. Therefore, clinical tests actually measure the diffusing capacity of carbon monoxide (DLCO) which provides an estimate of the gas-exchange function of the whole lungs (Plantier et al., 2018). DLCO is a measure of the conductance of gas transfer from inspired gas to the red blood cells, and is usually tested in a single breath where the partial pressure difference between inspired and expired carbon monoxide is recorded (Rosenberg, 1996; Plantier et al., 2018). The carbon monoxide transfer coefficient (KCO) is an index of the efficiency of alveolar transfer of carbon monoxide. It can be referred to as DLCO/VA, where VA is the alveolar volume where gas exchange

takes place (Graham et al., 2017).

It has been shown that DLCO is reduced compared with normal values in 98% of IPF patients at initial diagnosis, although 27% of patients have normal TLC volumes, and 56% have normal FVC (Cortes-Telles et al., 2014). Interestingly, KCO is within the normal range in up to 30% of IPF patients (Wallaert et al., 2012), particularly in patients with moderately reduced DLCO (Pastre et al., 2015). But a normal KCO value in IPF patients does not mean that pulmonary gas exchange is normal (Plantier et al., 2018). It has been noted that both DLCO and KCO are significantly associated with the degree of IPF measured from CT scans (Wells et al., 1997), but DLCO correlates more strongly with exertional increases in $P_{A-a}O_2$ (Agustí et al., 1994) and highly relates to both dyspnoea (Swigris et al., 2012) and survival time (Hamada et al., 2007).

Dead space ventilation

Increased physiologic dead space ventilation (increased ratio of dead space volume to tidal volume V_D/V_T) is an important characteristic of lungs with fibrosis and happens in most IPF patients both at rest and at exercise (Fulmer et al., 1976; Crystal et al., 1976; Agustí et al., 1991; Miki et al., 2009). The increased dead space is mainly caused by two physiologic features: the first is the increased anatomical dead space, which is a result of the dilation of conducting airways in IPF as discussed in Section 2.6.1 (Plantier et al., 2016); the second is the regional ventilation-perfusion mismatch (increased variation in regional ventilation-perfusion ratio, V/Q), which increases the physiologic dead space. In IPF lungs, the fibrotic (i.e. honeycomb or reticular) areas that are not perfused or poorly perfused but still receive ventilation will have an increased regional V/Q ratio (Strickland et al., 1993; Plantier et al., 2018). An early paper indicated that patients with IPF will often have a V_D/V_T ratio of greater than 0.4 compared with a normal

person (approximate 0.3 for normal) (Crystal et al., 1976). In normal individuals the efficiency of ventilation improves with exercise (that is the V_D/V_T falls) (Jones et al., 1966; Wasserman and Whipp, 1975), but in more than 90% of IPF patients V_D/V_T stays constant or may increase (Crystal et al., 1976).

Ventilation-perfusion mismatching

It is generally thought that the hypoxemia of IPF is related to V/Q mismatching (Wagner et al., 1976; Crystal et al., 1976; Society et al., 2000). This V/Q mismatching may be associated with abnormalities both in ventilation and perfusion (Crystal et al., 1976; Strickland et al., 1993). Crystal et al. (1976) showed an equilibrium picture of ^{127}Xe distribution, which was used to determine regional ventilation, and showed that patients with IPF have patchy, non-segmental areas of decreased ventilation where airway obstruction or alveolar destruction occurred. As for perfusion, a shift of perfusion was observed to the upper lobes (reflecting pulmonary hypertension) due to the basal distribution of fibrotic lesions, so that areas of relatively low V/Q ratios mostly presented in the upper zones of the lung (Crystal et al., 1976). However, Strickland et al. (1993) indicated that the CT based cystic air spaces (i.e. honeycomb) were observed as poorly perfused (probably due to vascular obliteration) but were usually normally ventilated, which explains the increase in physiologic dead space seen at rest and with exercise. Thus, a higher V/Q ratio can be seen in areas where fibrosis and cystic air spaces are dominant, which could be used to distinguish IPF from emphysema (Strickland et al., 1993). In addition, an increased minute ventilation was found in most patients with IPF during exercise. This is mainly due to the increased respiratory frequency, and in part relates to an increase in dead space ventilation (Society et al., 2000).

Arterial hypoxaemia

Alterations in the mechanical properties of the lungs, impairment of diffusion capacity and ventilation-perfusion mismatch will finally lead to early-onset exertional chronic arterial hypoxaemia and later-onset resting chronic arterial hypoxaemia in IPF (Hempleman and Hughes, 1991; Hughes et al., 1991; Plantier et al., 2018). Some studies support that the major cause of arterial hypoxaemia in a large proportion of IPF patients is not the diffusion barrier to oxygen or the anatomic shunts, as was originally suspected, but is due to ventilation-perfusion mismatching (Finley et al., 1962; Wagner et al., 1976; Society et al., 2000). The alveolar-arterial oxygen gradient ($P_{A-a}O_2$), which is calculated from arterial oxygen tension (P_aO_2) and alveolar oxygen tension (P_AO_2) may increase, resulting from the reduced ventilation-perfusion ratio, right-to-left shunting, or impairment of oxygen diffusion (Plantier et al., 2018). The increase in $P_{A-a}O_2$ reflects hypoxaemia in IPF (Agustí et al., 1991). In a study of 29 IPF patients, the measured average resting P_aO_2 was 69.3 mmHg, and four patients had normal resting P_aO_2 . However, although the resting P_aO_2 can be normal in some IPF patients, the resting $P_{A-a}O_2$ is invariably abnormal (in about 97% of the patients with IPF) (Crystal et al., 1976).

2.7 Summary

IPF is a devastating lung disease characterized by an irreversible decline of lung function, and its incidence increases with years of age. The current efforts of studies in IPF mostly focus on the accurate identification and diagnosis of early IPF, underlying mechanisms of pathogenesis and potential bio-markers that can indicate the patient-specific clinical course. The presence of IPF is variable in most patients, but some common characteristics and progressions can be summarized, although this is challenging. The

clinical and physiological features of IPF reviewed in this chapter provides background information for further quantitative analysis (Chapter 4) and computational modelling of patients with IPF (Chapter 5).

Chapter 3

Pulmonary lobar segmentation from CT scans

Identification of pulmonary lobes is of great importance for image-based analysis of lung function and disease progression. Segmentation of lobes can facilitate intra-patient image registration for localizing and tracking fibrosis disease progression over time, since lobes are important structural landmarks (Lassen et al., 2011). Also, knowing the lobar distribution of pulmonary fibrosis disease is helpful to understand the pathophysiology of the disease and to guide a patient-specific functional simulation. However, the pulmonary lobar fissure is usually difficult to segment fully automatically, especially for diseased lungs, as fissures are thin, usually of fuzzy appearance and incomplete, and can be obscured by or confused with features of disease (Ukil and Reinhardt, 2009). The following chapter outlines the development of an automatic pulmonary lobar segmentation method using a statistical finite element shape model of the lungs and lobar fissures to guide segmentation. Unlike 'deep learning' methods, this approach requires relatively few subject images as a training set. Development of this method was motivated

by the poor reliability of existing methods for a guaranteed estimate of fissure location, particularly in volumetric images of IPF, or when only thin-slice CT (non-volumetric images) are available.

3.1 Background

3.1.1 Pulmonary lobar anatomy

Within the thorax, the lungs are enclosed by the ribs, and the base of the lungs rests on the diaphragm. The space in between the two lungs is called the mediastinum, and contains the heart, major blood vessels, the esophagus, the trachea, main bronchi, and several other thoracic structures. The airways, blood vessels and nerves enter the lungs from the mediastinum at the hilum. The lungs themselves comprise airways, vessels and a connective tissue framework referred to as the interstitium.

Human lungs are divided into five distinct anatomical regions, which are called pulmonary lobes. These lobes are each supplied by separate airway and vascular branches, and are largely anatomically independent regions. The separating junctions between these lobes are called the lobar fissures. The left lung consists of the left upper lobe and left lower lobe, which are separated by the left oblique fissure (major fissure). The right lung consists of the right upper lobe, right middle lobe and right lower lobe, which are separated by the right oblique fissure (major fissure) and right horizontal fissure (minor fissure). These fissures contain pleural fluid and provide separation between the lobes while permitting some movement relative to one another. In general, the functions of these lobes are relatively independent from each other since there are no major airways and vessels crossing the lobar fissures (Lassen et al., 2010; Doel et al., 2015; Ukil and

Reinhardt, 2009). Figure 3.1 shows a schematic diagram of the lungs. The lungs are bounded by two layers of membrane (pleura) separated by a thin layer of lubricating pleural fluid.

Diagram of the Human Lungs

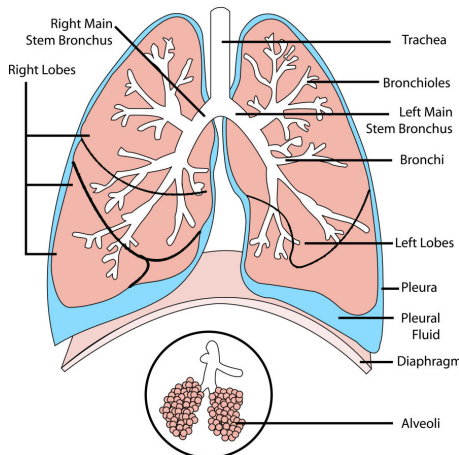


Figure 3.1: Schematic diagram of anatomical lung structure, showing the major airways, lobes and major fissures. The lungs are subdivided into the right upper (RU), right middle (RM), right lower (RL), left upper (LU), and left lower (LL) lobe. The pleural cavity which surrounds the lung consists of a double membrane layer (visceral pleura and parietal pleura) separated by a thin layer of pleural fluid. The inner membrane (visceral pleural) folds inwards between the lobes, creating fissures. Reproduced from (Doel et al., 2015).

3.1.2 High resolution computed tomography

CT imaging is a typical image modality used in diagnosis and management of IPF. It acquires multiple X-ray images at different orientations and reconstructs these images to obtain tomographic views in the region of interest (Zhang et al., 2011). This kind of imaging modality is typically used in clinical applications and research regarding pulmonary structure-function relationships (Hoffman and McLennan, 1997), including detection of both acute and chronic changes in the lung parenchyma. It is particularly

relevant here because normal two-dimensional X-rays can not show subtle defects. For evaluation of chronic interstitial processes (emphysema, fibrosis, and so forth), thin sections with high spatial frequency reconstructions are used (Coxson, 2007). Scans are often performed both in inspiration and expiration. This special technique is called HRCT. With the help of HRCT scans, a series of high-resolution chest sections can be acquired with slice thickness as low as 0.5 mm (Naidich, 2005), which can provide high visibility of the lung boundaries and pulmonary fissures. By making use of some advanced image processing technologies, a wide variety of features can be detected from these images such as density of the lung (Coxson, 2007), volumes of the lung (Hu et al., 2001), the regions of lung disease distributions (El-Baz et al., 2013; Ley-Zaporozhan et al., 2008), airway trees (Graham et al., 2010; Zhu et al., 2010; Diaz et al., 2010) and blood vessels (Shikata et al., 2009). Computed tomography (CT) images acquired at different stages in the breathing cycle can also be used to study lung mechanics and estimate regional lung ventilation (Hoffman et al., 2006; Yamamoto et al., 2011).

3.1.3 The importance of pulmonary lobar segmentation

The extraction of pulmonary lobes from CT scans is of great importance for lung disease assessment and treatment planning. For clinical applications, the distribution and location of pulmonary disease are beneficial information for doctors to recognize pathogenesis, guide therapy and have further value in surgical planning. That is, because many pulmonary diseases are more prevalent in specific anatomic regions of the lung, often acting at a lobar level. For example, emphysema (Jeffery, 1998), postprimary tuberculosis (Leung, 1999) and silicosis (Rees and Murray, 2007) usually affect the upper lobes, while idiopathic pulmonary fibrosis is commonly present in the lower lobes (Lin

and Jiang, 2015). However, there is currently a lack of quantitative and objective methods for the regional assessment of lung disease. Therefore, it is important to develop techniques that can identify the location, shape and volume of the lobes so that lung disease can be measured at a lobar level and the severity can be assessed accurately.

3.1.4 Challenges of automatic pulmonary lobar segmentation from CT scans

The most commonly used method to segment lobes from computed tomography (CT) is through manual assessment by an experienced pulmonary radiologist. However, the process of determining the lobar boundaries is extremely laborious and a time-consuming task, typically taking hours for one patient. This is because a 3D HRCT image may contain a large number of axial slices which makes the manual segmentation very time consuming. Therefore, doctors rarely use manual lobe segmentation in clinical diagnosis and treatment in practice, and most clinicians use subjective visual observation. For this reason, an automatic (no user interaction) or semi-automatic (minimal user interaction) lobe segmentation technique is urgently needed in clinical applications and this has attracted great interest from researchers all over the world (Van Rikxoort and Van Ginneken, 2013; Pu et al., 2009a; Ukil and Reinhardt, 2009).

However, to find an effective and time-saving automatic lobe segmentation method is a challenging task because of anatomical variation and the possibility of incomplete fissures. Lobar structures vary significantly between subjects, and the anatomical variation in lobe structure is usually associated with age, sex and body type. Pathologies of diseased lungs usually deform the lobar shape abnormally and result in fuzzy appearance of fissures on CT images, in particular when abnormalities are present near the

fissures, which makes fissure segmentation challenging. Even in patients with healthy lung parenchyma, fissures are sometimes incomplete (Gülsün et al., 2006; Doel et al., 2015) (see Figure 3.2).

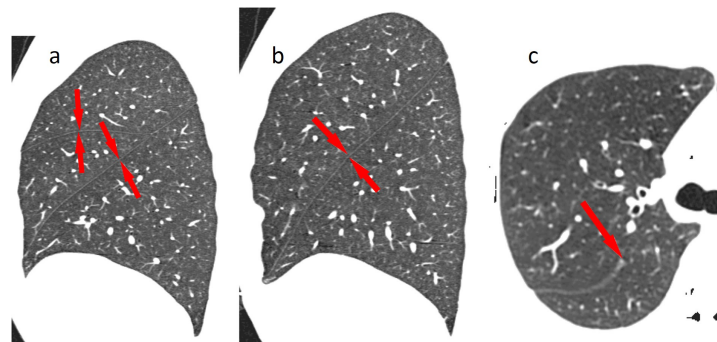


Figure 3.2: Slices of lung CT images illustrating the left and right fissures. Fissures are visible as white lines of high density tissue crossing the low density lung parenchyma. (a) Sagittal slice from the right lung showing the right oblique and horizontal fissures, the horizontal fissure is oriented horizontally. (b) Sagittal slice from the left lung showing the left oblique fissure. (c) Transverse slice from a different data set that show an incomplete right oblique fissure. Reproduced from (Ukil and Reinhardt, 2009).

3.2 Review of current published methods for pulmonary lobar segmentation

In a broad sense, existing lobe segmentation methods usually consist of two steps: the segmentation of lungs, and the detection of the three main pulmonary fissures (Van Rikxoort and Van Ginneken, 2013). Currently, a number of lung segmentation methods are available and most produce reliable results for normal lung at end-inspiration (Hu et al., 2001; Ukil and Reinhardt, 2005; Sun et al., 2006; Pu et al., 2008; Wang et al., 2009). In contrast, most challenges of automated lobar segmentation lie in the fissure detection, and currently no method has yet been demonstrated to be robust and effective across a

wide range of clinical imaging parameters and pathology experienced in clinical practice. Lung lobe segmentation is a complex multi-stage process that cannot be addressed by a simple algorithm (Van Rikxoort and Van Ginneken, 2013; Pu et al., 2009a; Ukil and Reinhardt, 2009). However, to some extent, lung segmentation and fissure detection are two independent parts and can be improved separately. That is, it should be possible to change lung segmentation in one way or another without affecting the fissure detection result dramatically. In the following section, existing work is discussed to highlight the key challenges of lobe segmentation algorithms, focusing on these two parts of the process. Then, a new approach to lung and lobe segmentation is presented.

3.2.1 Lung segmentation

Segmentation of lung is a prerequisite for the accomplishment of lobe segmentation, as it provides a boundary condition for subsequent fissure detection, allows estimation of lung volumes, and helps to detect and quantify abnormalities within the lungs. While not precisely defined, the lung region is usually considered to be the volume enclosed within the pleura, including the lung parenchyma, airways and vessels, but excluding those parts of the major airways and vessels which extend the pleural boundary. In this section, published methods for lung segmentation are briefly discussed. These methods are summarized in Table 3.1.

Conventional lung segmentation methods

In CT scans from healthy subjects, the air-filled lung parenchyma usually has a lower attenuation level compared to surrounding high-density tissue at the pleura. For this reason, many conventional lung segmentation algorithms adopt a thresholding approach to

Table 3.1: Summary of lung segmentation methods

Authors	Algorithms	Notes
Kalender et al. (1991); Kemerink et al. (1998); Leader et al. (2003)	2D thresholding method	1. May cause discontinuity between slices; 2. Time consuming
Keller et al. (1981); Heddlund et al. (1982); Hoffman et al. (1983); Hoffman and Ritman (1985)	Early-stage 3D thresholding method combined with manual interaction	Causes too many intra-operator errors
Hu et al. (2001)	1. Automatically choose thresholding value; 2. Separate left and right lung 3. Morphological lung boundary smoothing	First group to apply fully automatic 3D thresholding method
Ukil and Reinhardt (2005)	1. Bounding box defined around mediastinum; 2. Extract left and right main stem bronchi; 3. 3D Morphological boundary closing	Automatic method using air-way tree information
Sun et al. (2006)	1. Anisotropic filtering; 2. Wavelet transform-based interpolation to construct 3D data; 3. Adaptive 3D region growing combined seed-locating to detect lung region; 4. Fuzzy logic algorithm and 3D morphological to fill hole	3D method using signal-to-noise ratio
Kitasaka et al. (2003)	1. Affine transformation to fit a contour shape model to individual images; 2. Active contour model to refine initial segmentations in 3D	Solves the problem of lesions adjacent to the chest wall and mediastinum
Pu et al. (2008)	1. 3D initial thresholding processing; 2. Adaptive border marching	Minimizes oversegmentation of adjacent regions such as abdomen and mediastinum
Pu et al. (2011)	1. Principal curvature analysis to eliminate noise; 2. Radius basis function to smooth lung in 3D	Solves the problems of disease, noise or artifacts
Prasad et al. (2008)	1. 3D thresholding algorithm; 2. Adapt lung curvature using rib curvature; 3. Morphologic operation	1. Uses rib curvature information to define lung borders; 2. Solves the problem of error detection for lung pathologies
Wang et al. (2009)	1. 3D thresholding processing; 2. Texture analysis to identify abnormal regions; 3. 2D hole filling	Texture feature analysis to segment ILD lungs
Sun et al. (2012)	1. Active shape model to roughly find lung outlines; 2. Optimal surface finding to adapt final segmentations	3D method using rib information

search for a large connected region of the air-like values within the image. Threshold values are acquired from grey level histogram analysis and then an initial lung region is detected. A region growing method for the airways is usually applied subsequently to exclude the trachea and major airway branches. Some thresholding algorithms, especially older studies, were developed in 2D space, which means each axial section of CT imaging needs to be analysed separately (Kalender et al., 1991; Kemerink et al., 1998; Leader et al., 2003; Armato and Sensakovic, 2004). A 2-D method is a logical choice in the case of thick-slice CT data, but it may cause discontinuity between slices. Therefore, as higher resolution isotropic data became available, improved 3D processing methods were developed to avoid slice inconsistencies and reduce time for segmentation (Hu et al., 2001; Ukil and Reinhardt, 2005; Sun et al., 2006).

Most early 3D thresholding-based lung segmentation methods (Keller et al., 1981; Hedlund et al., 1982; Hoffman et al., 1983; Hoffman, 1985; Hoffman and Ritman, 1985) required significant manual interaction. This interaction included manually selecting threshold values or seed points for region growing, and separating left and right lungs manually. This leads to a process that is consuming and is subject to intra-operator errors. Hu et al. (2001) was the first group to apply a threshold-based algorithm in a fully automatic lung segmentation method. In their study, the lung region was firstly extracted from the CT images by gray-level thresholding processing. Instead of a fixed threshold value, an optimal thresholding method was used to automatically choose a threshold value that reflects the grey-scale characteristics of a specific dataset. The left and right lungs were then separated by identifying the anterior and posterior junctions by dynamic programming. Finally, a sequence of morphological operations was used to smooth the irregular boundary along the mediastinum.

Ukil and Reinhardt (2005) developed an improved automatic lung segmentation

method to smooth lung boundaries in 3D using information from the segmented airway trees. A bounding box was first defined around the mediastinum for each lung using information from the segmented human airway trees, and all operations were then performed within the bounding box. After that, all generations of the airway distal branches were defined to the left and right main stem bronchi to be part of the respective lungs, and all the other segmented structures could be excluded. Finally, a fast morphological closing with an ellipsoidal kernel was performed to smooth the surface of the lung. This method solved the problem of irregular and inconsistent lung boundary of the regions near the mediastinum by using a common threshold algorithm.

Sun et al. (2006) presented a 3D-based method for segmenting lungs with improved accuracy. An anisotropic filtering method was first applied on CT slices to enhance the signal-to-noise ratio. A wavelet transform-based interpolation method was subsequently used to construct the 3D volumetric CT slice data with volume rendering. After that, an adaptive 3D region-growing algorithm was developed to detect the lung region, combined with automatic seed-locating methods. Fuzzy logic algorithms and 3D morphological closing approaches were finally used to refine the lung volume and fill the holes in it. The method was effective and, in general, robust with an average accuracy rate of 88.5%.

Specially designed lung segmentation methods for abnormal lungs

Although conventional threshold-based methods are fast, robust and typically accurate for healthy subjects, they may fail to perform well for scans containing physiologic abnormalities, which often results in segmentation errors and requires manual editing of the results (see in Figure 3.3). Currently, specially designed lung segmentation methods mostly focus on a single lung disease and therefore can not get a good result across

a large population (Kitasaka et al., 2003; Sluimer et al., 2005; Pu et al., 2008, 2011; Prasad et al., 2008; Korfiatis et al., 2008; Wang et al., 2009; van Rikxoort et al., 2009; Sun et al., 2012).

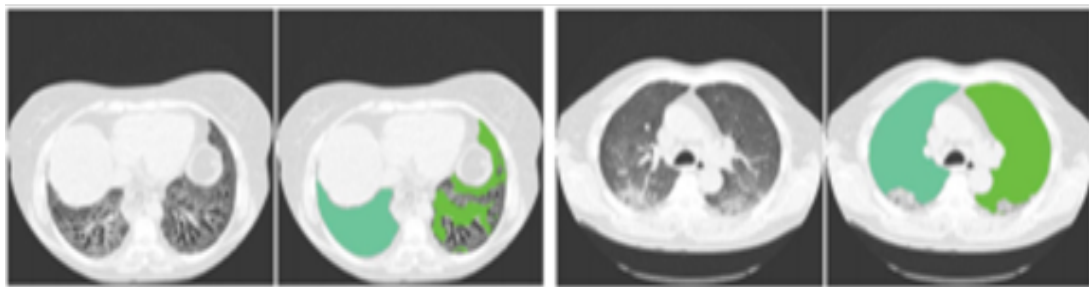


Figure 3.3: Illustration of the performance of conventional 3D thresholding lung segmentation methods on pathological lungs. Lung borders are not recognized accurately because of the higher densities of the abnormalities compared to the normal tissues. Reproduced from (Van Rikxoort and Van Ginneken, 2013).

To deal with the problem of lesions adjacent to the chest wall and mediastinum, (Kitasaka et al., 2003) developed a lung area extraction method using a shape model. A contour shape model using a Bézier surface was fitted to the contour surface of the individual input images with an affine transformation method. Then, an active contour model was utilized to refine the initial segmentation. The results showed that most lesions could be identified accurately using this method. However, as the lung apex and base were not included in the model, lesions adjacent to the lung apex or diaphragm could result in segmentation errors.

Pu et al. (2008) presented a lung segmentation algorithm based on adaptive border marching (ABM) to include juxtapleural nodules in the lung region since these nodules may be excluded from the results calculated by a conventional threshold-based algorithm. The adaptive border marching algorithm could smooth the lung borders after an initial thresholding processing and minimize over-segmentation of adjacent regions

such as the abdomen and mediastinum. The method was tested on 20 datasets and the results demonstrated that this method could re-include all juxtapleural nodules in the lung regions. An average over-segmentation ratio of this method was 0.43% which was lower than the reference standard average segmentation determined by an expert. In order to deal with the problem of different types of lung disease, image noise or artefacts, and individual anatomical variety, Pu et al. (2011) developed a shape analysis strategy termed "break-and-repair". A principal curvature analysis was applied to eliminate the problematic regions and then radial basis function (RBF) based implicit surface fitting was used to get a smooth lung surface.

To overcome the error in detection of the lung boundaries for lung pathologies, Prasad et al. (2008) made use of rib curvature information to help with finding the lung borders. The method was based on a threshold-based algorithm followed by a morphologic operation. The core principle of the method was to adapt the threshold value to an individual subject by making the curvature of lung along the ribs be similar to the curvature of the ribs. These curvatures were both represented by polynomial interpolation even though there was minimal deviation from this representation. The results showed that the performance of the rib segmentation method was better than the same method without guidance from rib segmentation.

Wang et al. (2009) proposed a texture analysis-based method to segment ILD lungs. The lung region including normal and mild ILD lung parenchyma was first segmented by a CT value thresholding technique and then texture-feature images derived from the co-occurrence matrix was used to identify abnormal lung regions with severe ILD from the initial results. 2D hole filling was applied to smooth the final lung segmentation. The overlap rate, volume agreement, mean absolute distance (MAD), and maximum absolute distance between the automatically segmented lungs and the reference lungs

(delineated manually by a medical physicist) were employed to evaluate the performance of the segmentation method, and showed accurate lung segmentation results for abnormal CT scans with severe ILD.

On the basis of the previous studies, (Sun et al., 2012) developed a further approach for segmentation of lungs with high-density pathologies. The method had two main steps. In the first step, a robust active shape model (RASM) matching method was utilized to roughly find the outline of the lungs. To initialize the shape model of RASM, detected rib information was used. In the second step, an optimal surface finding approach was applied to further adapt the initial segmentation result to the lung. The method was evaluated on both normal and abnormal subjects and had a better performance compared to two commercially available lung segmentation approaches.

3.2.2 Fissure detection

The currently published fissure detection methods can be, for the most part, classified into two categories: anatomical knowledge based analysis methods and shape based analysis methods. Anatomical knowledge based methods usually depend on either local or global knowledge of the anatomy of lung structure based on two pulmonary anatomical features. The first feature is the fact that there should not be any large vessels in the vicinity of lobar fissures, so fissures should locate in the gaps between airway and vessel trees. Another feature is that the airway bronchi can be classified into five lobar branches using an edge detection method (Figure 3.4). Shape based analysis methods commonly make use of gray-level information and shape information to detect the fissures. Published fissure detection methods are summarized in Table 3.2.

Table 3.2: Summary of fissure detection methods

Authors	Algorithms	Notes
Kuhnigk et al. (2003, 2005)	Watershed transformation method to analyze anatomical structures to help with fissure detection	First group to use lobar airways and vasculature into fissure detection ¹
Ukil and Reinhardt (2009)	1. Watershed transform guided cost image to define initial fissures; 2. Construct ROI; 3. Structure tensor analysis combined with optimal surface detection to find fissure surface; 4. Fast marching method to detect incomplete fissures	1. Improved on Kuhnigk's method; 2. Can detect incomplete fissures ¹
Lassen et al. (2010)	Watershed transformed anatomical structure based method	An extension of Kuhnigk's method ¹
Zhou et al. (2004); Saita et al. (2006)	1. Edge detection to class vessels and bronchi; 2. Hough transform to detect curve surface	Take advantage of linear appearance of fissures ¹
Wang et al. (2004, 2006)	1. Identify initial fissure ROI; 2. "Ridge map" based transformation to enhance initial fissure; 3. Shape-based curve growing to get the final fissures.	2D shape based method ²
Frangi et al. (1998)	Hessian matrix based analysis to extract local image structures	The first paper to apply Hessian matrix analysis on image segmentation in 3D ²
Wiemker et al. (2005)	Combine first derivative and second derivative of image gray values to find fissures	An early paper using Hessian matrix on fissure detection ²
Ochs et al. (2007); van Rikxoort et al. (2008)	Use pattern recognition approach and Hessian matrix and classification operation to detection fissure	An improved Hessian based method ²
Lassen et al. (2011, 2013)	1. Use anatomical structures to acquire initial fissure; 2. Hessian matrix surrounding initial guessing areas; 3. Morphological operations to filter noise	Combine both anatomical information and gray-level information ^{1,2}
Doel et al. (2012)	1. Use both anatomy knowledge and Hessian matrix to find fissure candidate points; 2. Multi-level B-spline curve to get the final fissure surface.	Combine both anatomical information and gray-level information ^{1,2}
Ross et al. (2010, 2013)	1. Particle system combined with Hessian matrix to get candidate fissure points; 2. Maximum a posterior method to remove noise points; 3. Thin plate spline to form final fissure surface.	Effective for lung lobe segmentation in absence of complete anatomical structures on CT imaging ²

¹ Anatomy knowledge based method.

² Shape based analysis method.

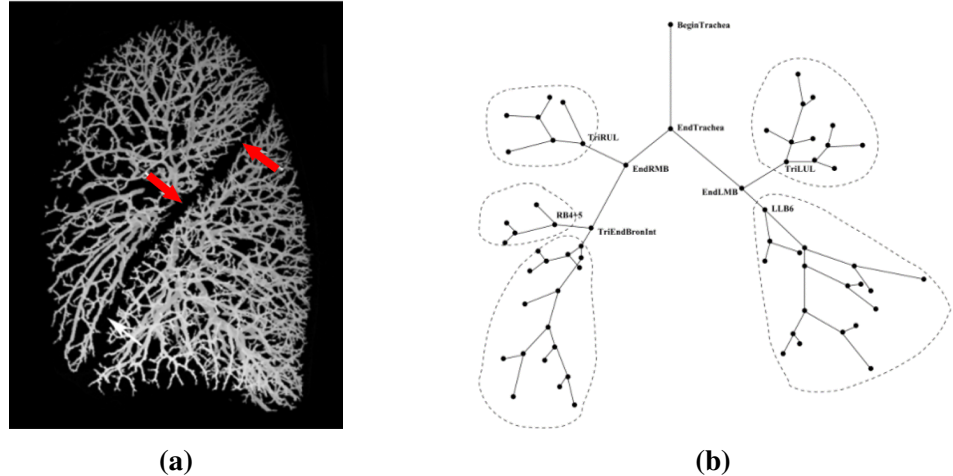


Figure 3.4: (a) Segmented volumes of the vascular tree. There are no large vessels in the vicinity of lobar fissures. (b) Anatomically labeled airway tree showing lobar subtrees. The airway tree can be classified corresponding to five lobes. Reproduced from (Ukil and Reinhardt, 2009).

Anatomical knowledge based method

Methods that aim to detect the lobar fissures usually start by finding an approximate location of the lobar borders based on prior anatomical knowledge of lung structures in order to narrow the search area for fissure detection (Kuhnigk et al., 2003, 2005; Zhou et al., 2004; Saita et al., 2006; Zhang et al., 2006; Ukil and Reinhardt, 2009; Pu et al., 2009a; Lassen et al., 2010; Doel et al., 2012). These methods are developed mainly based on two pulmonary anatomical features. A number of published papers use the segmentation results of airways and vessels to help localize fissures. Usually, the vascular segmentation provides more accurate estimation of lobar fissure locations than the airway trees, since more vessel generations can be detected from CT scans. These vessels span the entire lung volume which can help to find complete gaps between lobes. However, airways also play an important part in initial estimation of fissures, since airways trees can be more reasonably divided into lobes based on branching structure,

while the structure of vasculature branching is more complicated to extract from images and some connections are hard to separate accurately. Therefore, a lot of studies make use of both vessel and airway information to guide fissure detection (Ukil and Reinhardt, 2009; Lassen et al., 2010; Doel et al., 2012).

Kuhnigk et al. (2003, 2005) was an early group to present a framework of taking both lobar airways and vasculature into account for automatic fissure detection. A watershed transformation method has been used to take an analysis of these anatomical structures and this method was widely used and improved by other researchers, but the results calculated by this simple algorithm were not accurate enough even for some clearly visible fissures.

Ukil and Reinhardt (2009) developed Kuhnigk's fissure detection method which used a distance transform to combine segmented vessels, lobar airways, and original chest CT scan as a cost image to guide initial fissure guessing. They found that the improved watershed transform algorithm could provide a close initial approximation to the lobar fissures. Subsequently, a refinement method was used to construct a region of interest (ROI) which encompasses the fissures. A 3D optimal surface detection algorithm combined with a 'ridgeness' measurement was then applied to enhance the ROI, and find the optimal surface within the ROI. Finally, incomplete fissures were smoothly extrapolated using a fast-marching method based segmentation of a projection of the optimal surface. This method is able to segment incomplete fissures, and so significantly improved on prior methods.

Lassen et al. (2010) also described a fissure detection method by building a cost image for the watershed transformed segmentation which is an extension of the framework of Kuhnigk. The interactive segmentation method was tested on 25 CT scans comparing to a manual segmentation by a human observer and showed an average error

distance of 1.57 ± 0.3 mm. In addition, Zhou et al. (2004) and Saita et al. (2006) took advantage of the linear appearance of fissures to class the vessels and bronchi into five lobe regions using an edge detection method and used a Hough transform based curved surface detection method.

Shape based analysis method

Generally, lobar fissures can be regarded as bright planes crossing the pulmonary volume because of the higher density value of fissures compared to the surrounding tissues. Based on this information, quite a number of published methods use a local filtering algorithm to detect the voxels which lie on these planes, so that these detected voxel points can construct a continuous fissure surface. In 2D space, the fissure appears as a clear curve, therefore some early papers usually detected fissure points based on gray-level information in 2D space. For example, Wang et al. (2004, 2006) presented a 2D fissure detection method based on shape information. In this paper, the fissure was initially denoted as a curve based on the prior knowledge of the fissure shape to identify the surrounding region of fissure, called "fissure region" for subsequent automatic segmentation. Next an image transformation called "ridge map" was proposed for enhancing the appearance of initial fissures. A shape-based curve-growing method modeled by a Bayesian network could then be applied to this "map" to segment the fissure.

In 3D space, the most commonly used method to detect these pulmonary fissure plane structures is taking an eigenvalue analysis of the Hessian matrix (Frangi et al., 1998; Wiemker et al., 2005; Kitasaka et al., 2006; Ochs et al., 2007; van Rikxoort et al., 2008; Lassen et al., 2011, 2013; Ross et al., 2010; Doel et al., 2012). Frangi et al. (1998) was the first to present an eigenvalue analysis of the Hessian matrix to detect planar structures (fissures) and tube structures (vessels) on CT images. The relationship

between three eigenvalues of the Hessian matrix describes the local image structure and so can be used to determine a fissure probability. Wiemker et al. (2005) also used the Hessian matrix for fissure detection, proposing two 3D filter approaches in this paper. The first filter was based on the first derivatives of the image grey values and utilized the eigenvalues of the local structure tensor. The second filter was based on the second derivatives and utilized the eigenvalues of the local Hessian matrix.

Ochs et al. (2007) and van Rikxoort et al. (2008) used a pattern recognition approach to detect pulmonary fissures combined with eigenvalue analysis of the Hessian matrix as feature and classification was also performed on these fissures. Lassen et al. (2011, 2013) combined both anatomical based and shape based methods which successfully eliminated most false points (points identified as fissure but were not). The first anatomic-based method defined a region of interest, and then the Hessian matrix analysis was used only in this region of interest. The region of interest provides an initial guess for fissure locations. Subsequently, morphological operations such as direction-based connected component analysis were used to further reduce non-fissure points that are incorrectly identified as fissures. Doel et al. (2012) also made use of both an anatomical knowledge based method and the Hessian matrix to find fissure candidate points and constructed a multi-level B-spline smooth curve through the fissure points and extrapolated this curve to the lung borders to get complete fissure surfaces.

Ross et al. (2010, 2013) proposed a particle system that sampled the image domain combined with the Hessian matrix to get a set of candidate fissure locations. A maximum a posteriori (MAP) estimation was then used to eliminate false candidate points, and a post-processing operation was applied to remove remaining noise. A thin plate spline (TPS) interpolating surface fitting method was lastly performed to form the final fissure surfaces. This method is effective for lung lobe segmentation in the absence of

complete anatomical structures on CT imaging.

3.3 Methods: automatic statistical shape model based lobar segmentation method

Here, an SSM guided method is presented to segment pulmonary lobes from CT images.

A three-step approach is followed for the lobe segmentation (shown in Figure 3.5): in the first step, a threshold-based lung segmentation method defines the lung boundary; in the second step, an SSM is deformed to provide a "search region" for fissure locations; in the third step, fissures are located using a Hessian matrix protocol combined with connected component filters and a surface fitting algorithm. The new procedure does not depend on prior segmentation of anatomical structures (airway lobar classification) other than lung shape. A user-interactive interface was also developed for the user to control and visualize the whole segmentation process and to allow do some manual correction on the segmented results, if required.

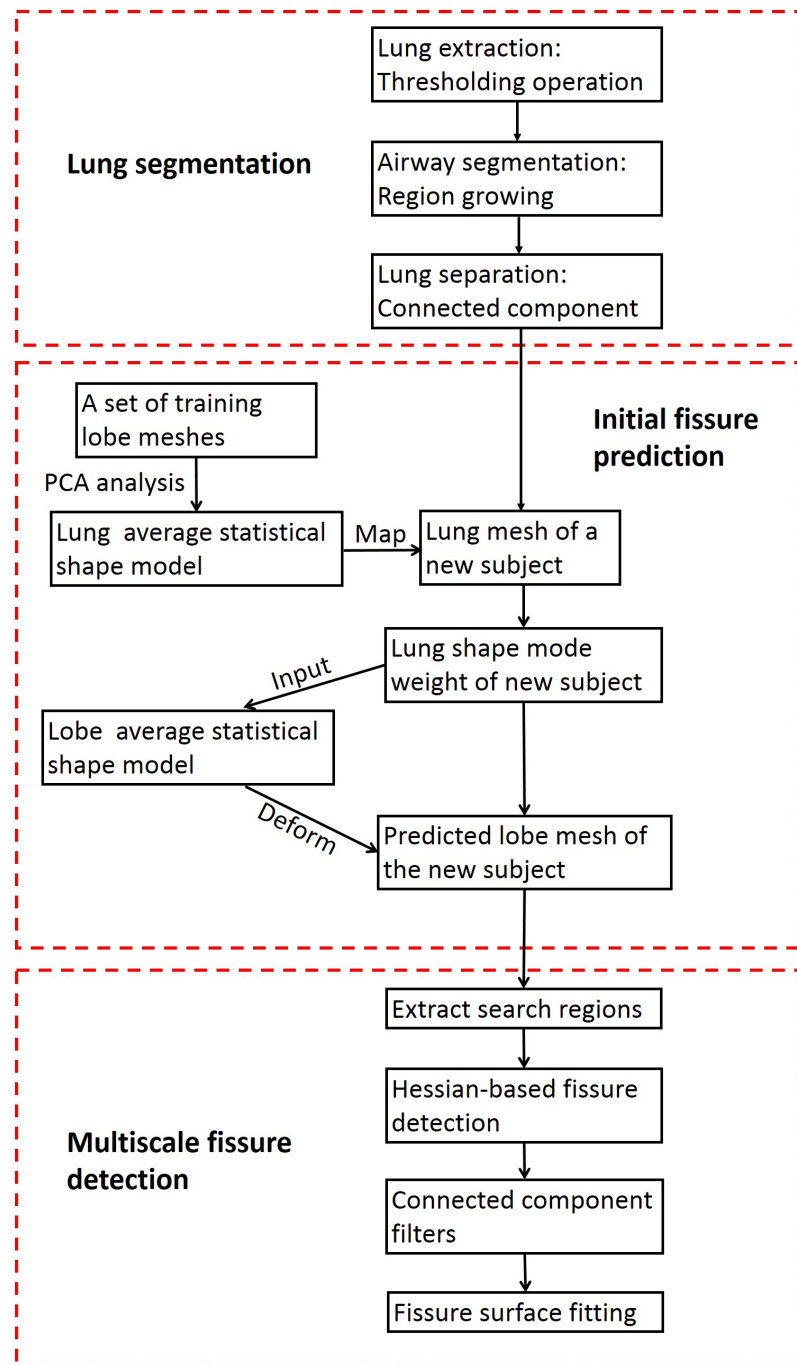


Figure 3.5: Flow diagram of the lobar segmentation process.

3.3.1 Lung segmentation

A good lung segmentation is a prerequisite for lobe segmentation, since all the other segmentations need to be performed inside the two lung regions. Here, a common thresholding method was used to segment the lungs (Ukil and Reinhardt, 2005). The procedure consists of the following steps: 1) uses a thresholding operation (-775 Hounsfield Units) and connected component identification to find the initial lung regions and trachea location, 2) by using the most apical point of the trachea as a starting point, a region growing technique is applied to detect the airway trees, and 3) left and right lungs are separated as the two largest connected components remaining after removing the trachea and main left and right bronchi. Figure 3.6 shows a typical lung segmentation result.

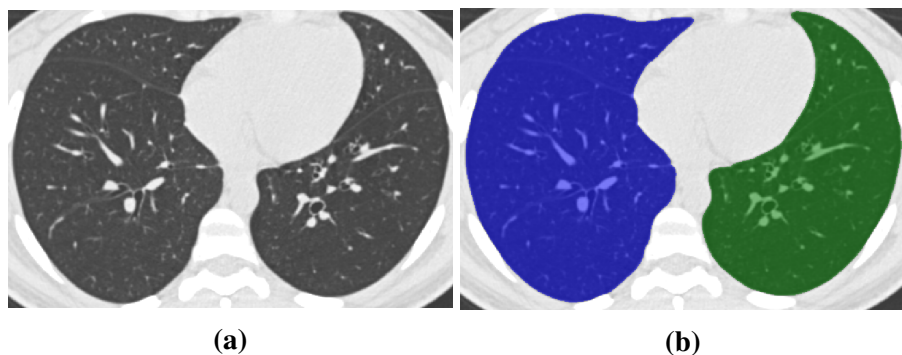


Figure 3.6: Lung segmentation result using the common thresholding method. (a) Raw CT image. (b) Segmented lungs.

3.3.2 Statistical finite element models of lung and fissure shape

For human organs, there is a significant difference in shape and anatomy between different groups of people, such as young and old, male and female, healthy and diseased (Krumpe et al., 1985; Crapo, 1993). This difference is caused by different functional signals and behaviours, leading to organ shape variation across populations. Shape

analysis provides a way to understand the underlying mechanisms of those variations in anatomical and physiological processes. The importance of statistical shape analysis in many kinds of biological studies has been well established (Dryden and Mardia, 1998; Stegmann and Gomez, 2002; Styner et al., 2003; Heimann and Meinzer, 2009), because of its potential to capture morphological variation within and between healthy and pathological structures.

Computational model-based approaches to solve problems in image segmentation have become increasingly popular in the last two decades (Taylor et al., 1995; Kelemen et al., 1999; Tsai et al., 2003; Okada et al., 2008). In these approaches, each new image set was matched to its expected shape of organ for that individual as a guide for segmentation. This potentially reduces the impact of image artefacts and other perturbations associated with traditional low-level algorithms (Ecabert et al., 2008; Zhang, 2013). To account for individual variations in lung shape and location of fissures (including how they vary with lung inflation), one can analyse a series of training shapes using statistical techniques, leading to a statistical shape model. Using this statistical definition of a cohort of individuals, one can begin to predict an individual's organ shape based on characteristics of that individual to help guide segmentation procedures.

Finite element lobar shape modeling

To guide a statistical shape model based segmentation, the first step is to generate a statistical lobar shape mesh using a set of training data. Here, we employ a Statistical Finite element analysis of Lobe (SFeaL) based on an active shape model (ASM) (Cootes et al., 1995). To do this, a training set of segmented lung and fissure surface locations was used to describe a cohort of adults with radiologically normal lungs. This approach employs a finite element shape mesh to specify pulmonary lobar shape which provides an efficient

parameterized representation of lobar boundaries and makes shape constraints available during image analysis. The training set consisted of data from 50 subjects. 35 subjects were selected from a study of healthy subjects aged 50 to 100 years, the human aging cohort (AGING) study and a further 15 subjects were selected from a separate study of younger healthy subjects, the Human Lung Atlas (HLA). All the AGING and HLA subjects are healthy non-smoking subjects including both males and females. In the AGING group, HRCT imaging was acquired at Auckland City Hospital using a Phillips Brilliance 16 scanner, with between 400-700 slices per volumetric image. The study was approved by the Northern A Health and Health and Disability Ethics Committees (HDEC), Ministry of Health on 29 April 2013 through the HDEC-Full Review Pathway - ethics reference 13/NT/41. The HRCT images from HLA cohort were obtained at the Iowa Comprehensive Lung Imaging Center (I-Clic) using a Siemens Sensation 64 MDCT scanner, with between 500-700 slices per volumetric image. The study was approved by the University of Iowa Institutional Review Board. A summarized population demographics of the subjects used for statistical shape model construction is listed in Table 3.3

Table 3.3: Summarized demographics for the AGING and HLA datasets.

	AGING (N=35)	HLA (N=15)
Age (years)	72.3 ± 11.41	22 ± 1.9
Sex(M/F)	18/17	5/10
Height(m)	1.66 ± 0.14	1.7 ± 0.1
Weight(kg)	70.6 ± 11.1	67.6 ± 12.2
BMI(kg/m^2)	25.6 ± 3.0	23.3 ± 2.2
Ethnicity		
- Caucasian	25	14
- Māori(AGING only)	1	N/A
- Asian	2	-
- African-American	-	1
- Unknown	7	-

To define the lung shape, volumetric CT images were segmented using the method described in Section 3.3.1. The segmented lung surface was then digitized into a set of data points as a 3D-space representation of lung shape (Figure 3.7a). Fissure surface segmentation was performed manually using the open-source visualization software CMGUI (<https://www.cmiss.org/cogui>) by an expert user, to provide a gold-standard definition of the fissure location for each subject in the training set (Figure 3.7b, 3.7c). A high order (bi-cubic Hermite) finite element template mesh with the same mesh connectivity for each subject was geometry fitted to the lung and fissure surface data for each subject. The current lung lobe mesh consists of two separate meshes which represent the left and right lung enclosing the lung parenchymal tissue volume.

An initial template mesh was created by selecting some data points to be nodes, and then creating two-dimensional surface elements by joining these node points appropriately. The template mesh for the left lung mesh has 35 nodes and 44 elements which described the left lung surface and left oblique fissure, while the right lung mesh has 50 nodes and 62 elements which defined right lung surface, right oblique fissure and right surface fissure. For fitting to lung and lobe shape data, the template mesh was modelled using bi-cubic Hermite basis functions with C1 continuity. This bi-cubic Hermite mesh has the same mesh connectivity as the template mesh, but it also contains nodal derivative information. Each node has 12 degrees of freedom (DoF)s which store the global coordinates (x, y and z) and first and second nodal derivatives ($\frac{\partial n}{\partial \xi_1}$, $\frac{\partial n}{\partial \xi_2}$, and $\frac{\partial^2 n}{\partial \xi_1 \xi_2}$), where n is x, y and z, and ξ is the local element coordinate. In this lung lobe model they are defined such that ξ_1 is in the anterior-posterior direction while ξ_2 is in the cranio-caudal direction. ξ_1 and ξ_2 have values that range from 0 to 1. Each node of the fitted mesh is either an anatomical landmark (the left/right lung apex, the base vertex, the shape corner and the centre point of the middle line of fissure) or a pseudo-landmark

(e.g. a specific proportion of the arc-length between two anatomical landmarks). These landmarks allow the coordinate of the control points to be defined in consistent positions registered to the geometry of the lung. A least squares fit of the mesh to the lung and fissure surface data was conducted using CMISS (<https://www.cmiss.org>), which is a finite element modelling environment. Specifically, the sum of the distances between each data point and its projection on to the nearest element was minimized during the fitting process. This distance is a function of the element location and shape parameters. In this procedure, the nodal parameters are interpolated to find the projected points. The global coordinates of the projected points are a function of local element coordinates, ξ_1 and ξ_2 , and nodal parameters. Some manual operations were involved to adjust the mesh nodal positions and derivatives to the data cloud, which can help to improve the speed and accuracy of fitting. The average root mean square (RMS) error of this fitting method was 4.79 mm for the 50 training subjects (Figure 3.7d). More details on the fitting procedure can be found in (Bradley et al., 1997; Tawhai and Burrowes, 2003; Fernandez, 2004).

PCA-based statistical shape model construction

A prerequisite of the construction of an SSM is object alignment to remove the orientation and scaling differences between shapes. Here a General Procrustes Alignment (GPA) was selected as a registration method (Dryden and Mardia, 1998; Rohlf, 1999). The GPA algorithm finds the optimal rotation matrix and translation vector which minimizes the overall distance between two sets of points with respect to the Euclidean norm. In this study, a reference lung model sample was randomly chosen from the training set. Then all the other training models were aligned to this reference model. In this process, the volumes of all subjects were normalized to 1 L and any residual rotation and trans-

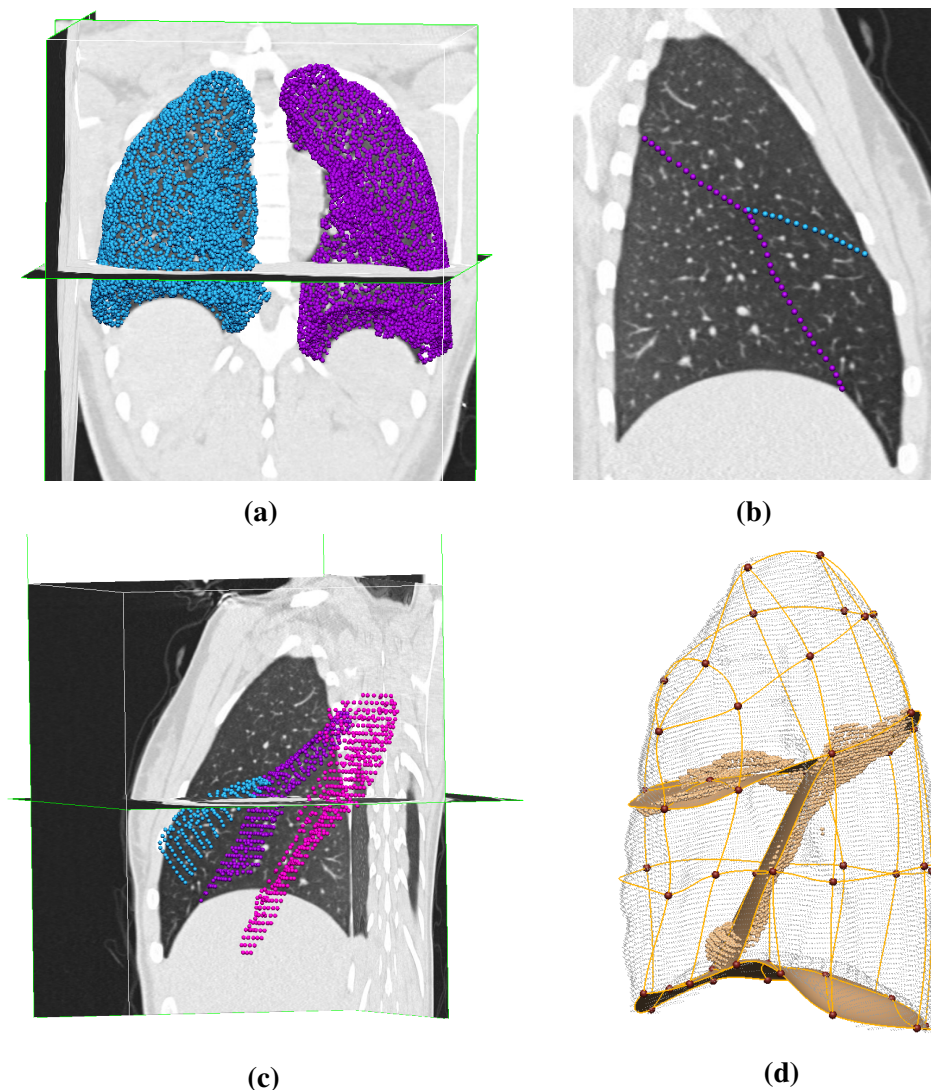


Figure 3.7: Finite element modeling of lung lobe shape. (a) Lung surface data extracted from segmented lung masks (purple points for left lung, blue points for right lung). (b) Manual digitized fissure points in 2D sagittal image of right lung (purple points for right oblique fissure, blue points for right horizontal fissure). (c) Manual digitized fissure points shown in 3D (pink points for left oblique fissure, purple points for right oblique fissure, blue points for right horizontal fissure). (d) Lobe shape fitting with lung surface data and digitized fissure data of right lung.

lation were removed. The generalized procrustes alignment can be represented as an affine transformation in mathematical terms

$$\bar{S} = \alpha RS + T, \quad (3.1)$$

where \bar{S} represents the aligned shape vector to the reference shape from the subject shape vector S , R is the rotation matrix and T is the translation vector. Figure 3.8a shows the procrustes aligned meshes of all the 50 subjects. For each subject, the aligned lung shape can also be represented as

$$\bar{S} = [\bar{x}_1 \ \bar{x}_2 \ \bar{x}_3 \ \cdots \ \bar{x}_{p-1}; \bar{x}_p], \quad (3.2)$$

where \bar{x} are the nodal parameters which contain coordinates and derivatives (12 DoFs), and p represents the number of nodes for both left and right lung ($p = 225$ in this study). The data vector \bar{S} of each lung was then assembled as the concatenation of all lungs, termed \bar{S}_{whole} . \bar{S}_{whole} is an $n \times N$ matrix, where n is the number of nodal parameters for each lung ($n = 12 \times 225 = 2700$ in this study), and N is the number of training subjects ($N = 50$). Thus, \bar{S}_{whole} can be regarded as a cloud of N points in the constructed $n \times N$ space. This matrix was decomposed into modes of variation using PCA. PCA is a commonly used technique in statistical feature space to reduce the dimension of the dataset. It uses an orthogonal transformation to convert a number of (possibly) correlated variables into a set of values of linearly uncorrelated variables called principal components. The number of distinct principal components is equal to the smaller of the number of original variables or the number of observations minus one. The resulting vectors are an uncorrelated orthogonal basis set.

In order to perform PCA, each shape parameter was centred by subtracting the mean

value \bar{x} . Then the covariance matrix was built based on the mean-centred matrix S by $C = SS^T$. After the PCA technique was performed on the covariance matrix C , we obtain a set of eigenvectors $\mathbf{u}_1, \mathbf{u}_2, \dots$, corresponding to a set of non-negative eigenvalues $\lambda_1, \lambda_2, \dots$. Each eigenvalue represents how much variation or variance in the data is captured by the corresponding eigenvector. Each lung shape variation $m_i(w)$ can be approximated by a linear combination of the eigenvector and its corresponding eigenvalue

$$m_i(w) \approx S_{mean} + \mathbf{u}_i w_i, \quad (3.3)$$

where w_i is a weight factor given to each mode of variation, and $i = 1, \dots, L$ ($L \leq 49$ in this study). S_{mean} is the average shape across all the subjects, which is obtained by

$$S_{mean} = \frac{1}{N} \sum_{i=1}^N s_i, \quad (3.4)$$

where s_i is the i th lung shape model from the training set, here $i = 1, \dots, N$ ($N=50$ in this study). The average shape model is shown in Figure 3.8b.

3.3.3 Initial prediction of lobar location in an individual

Using the method described in section 3.3.2, the lung shape variation across the training set can be decomposed into a series of modes, and each specific lung shape can be represented with the corresponding mode weight values. In this study each mode represents one type of lung and fissure surface shape variation. In order to predict the fissure location, two PCA-based SSMs were constructed using the same training dataset. The first lobe SSM was built using both the lung surface parameters and fissure surface parame-

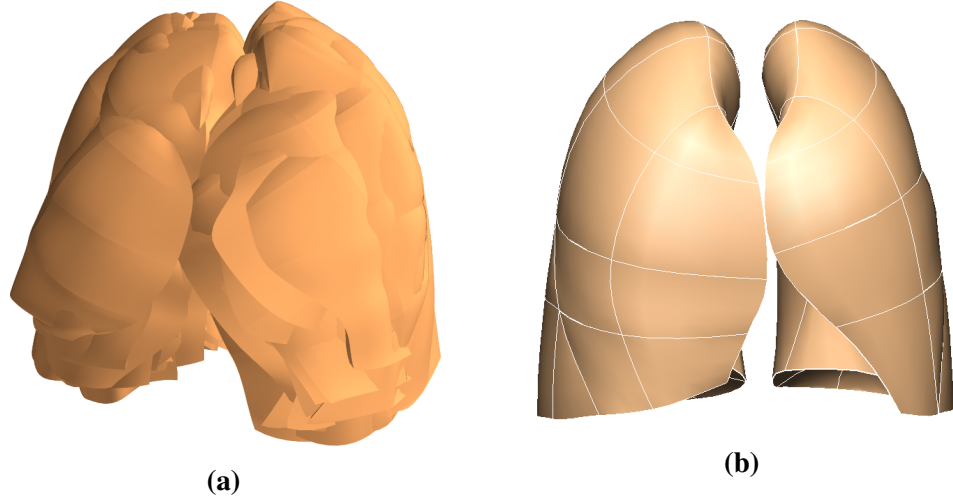


Figure 3.8: Statistical shape model construction based on principal component analysis. (a) Procrustes aligned meshes of 50 subjects. (b) Average shape model of 50 training subjects. All the weight values are zero for this shape model.

ters. The second lung SSM was derived for the same training set but did not include the fissure surfaces and so only described the shape of the lung surface.

The two SSMs were used to predict the fissure locations for subjects that were not part of the training set, using only the definition of the lung surface for the subject as input. A finite element mesh of the lung surface (without fissure information) was generated for each new subject. The new fitted lung mesh was procrustes aligned to the same reference model as the training subjects were aligned to. Then this aligned lung surface mesh was projected on to the lung surface SSM (with no fissure surfaces). The principal component weight values were calculated from the projection, which was represented as $w_{new} = [w_{new1}, w_{new2}, \dots, w_{newL}]$ ($L \leq 49$) here. The first seven principal components accounted for over 90% of the total lung shape variation in the training set. Therefore, the first seven mode weights were used on the lobe SSM (which includes both lung and fissure surfaces) to reconstruct the projected lobe mesh for this new subject

$$S_{new} = S_{mean} + \sum_{i=1}^7 \mathbf{u}_i w_{newi}, \quad (3.5)$$

where S_{mean} is the average lobe shape model across all the subjects, \mathbf{u}_i is the first seven eigenvectors of the covariance matrix C corresponding to the lobe SSM, and w_{newi} is the projected weight values from the lung SSM. An initial estimation of fissure locations was then made (Figure 3.9). This initial prediction of lobar fissures provides a reduced search area for subsequent image analysis and ensures an estimation of complete lobar structures even if a fissure is incomplete or is difficult to detect.

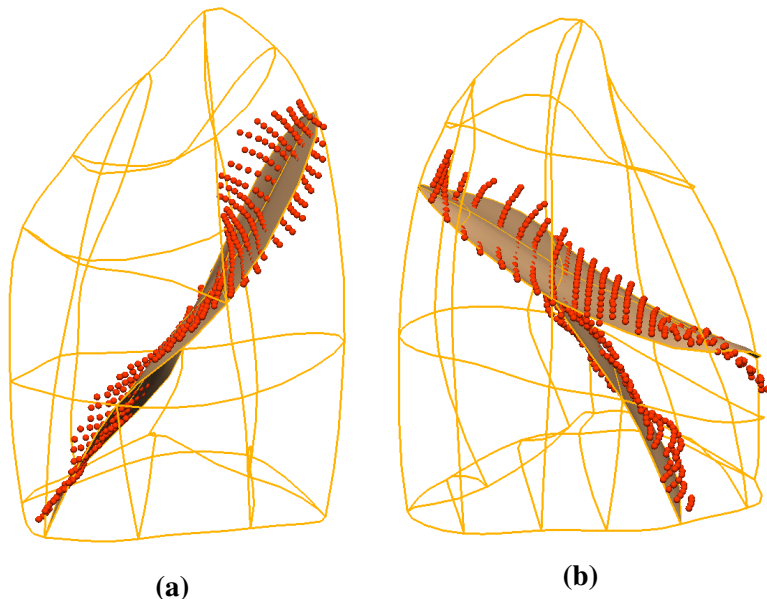


Figure 3.9: Fissure prediction results compared to ground truth fissure points for one subject. The fissure surface meshes are estimated fissure locations and the red points are manual tracing fissure points by an expert. (a) Left lung. (b) Right lung.

3.3.4 Multi-scale Hessian-based fissure detection

The final fissure detection was accomplished using an enhancement filter. Conventional enhancement filters are typically based on first (structure tensor) or second (Hessian matrix) order image information (Frangi et al., 1998; Lorenz et al., 1997). This study used the Hessian matrix based on gray-scale curvature information combined with Gaussian smoothing as a basic operator to enhance the fissure structure. In 3D space, fissures are free-form surfaces in the lungs that locally resemble plate-like structures, since the grey-value increases rapidly from the structure border to the centre and decreases again to the opposite border. Hessian-based filters are typically used to enhance and differentiate structures with specific shapes, i.e., blobs, sheets and tubes (Frangi et al., 1998; Lorenz et al., 1997).

A common approach to analyse the local behaviour of an image, L , is to consider the local grey-value variations in the neighbourhood of a point x_o modelled by a Taylor expansion to the second order

$$L(x_o + \delta x_o, s) \approx L(x_o, s) + \delta x_o^T \nabla_{o,s} + \delta x_o^T H_{o,s} \delta x_o, \quad (3.6)$$

where $\nabla_{o,s}$ and $H_{o,s}$ are the gradient vector and Hessian matrix, respectively, of the image computed in x_o at scale s .

To calculate these differential operators of L , concepts of linear scale space theory are used (Koenderink, 1984; Florack et al., 1992). In this framework, differentiation is defined as a convolution with derivatives of Gaussians

$$\frac{\partial L(x, s)}{\partial x} = s^\gamma L(x) * \frac{\partial G(x, s)}{\partial x}, \quad (3.7)$$

where the D-dimensional Gaussian is defined as

$$G(x, s) = \frac{1}{\sqrt{2\pi s^2}^D} e^{-\frac{\|x\|^2}{2s^2}}, \quad (3.8)$$

where s is the kernel size of the Gaussian. The second derivative of a Gaussian is in many cases a good approximation to the optimal filter for a plane-like structure. Through using the second derivative operator combined with Gaussian smoothing as the basic operator (Hessian matrix), we are able to make the non-supervised fissure filter scale-dependent (Lorenz et al., 1997; Li et al., 2003). In order to make sure a variety of sizes of fissures can be captured by the Hessian, a range of kernel sizes was implemented from 0.5 mm to 2.5 mm in 0.5 mm increments as the kernel size of the Gaussian to obtain a final estimate of 'fissureness'

$$F_{output} = \max_{s_{min} \leq s \leq s_{max}} F_0(s), \quad (3.9)$$

where s_{min} and s_{max} are the minimum scale (0.5 mm) and maximum scale (2.5 mm). Each scale s gets a response. In the final output of the multiscale enhancement filter, the maximum output over all scales is assigned to each voxel.

At each image voxel, the Hessian matrix was constructed from the six independent second order derivatives as a symmetric matrix

$$\text{Hessian} = \begin{bmatrix} H_{xx} & H_{xy} & H_{xz} \\ H_{yx} & H_{yy} & H_{yz} \\ H_{zx} & H_{zy} & H_{zz} \end{bmatrix}, \quad (3.10)$$

where $H_{ij} = \left| \frac{\partial^2 H}{\partial r_i \partial r_j} \right|$, and r represents the gradient direction.

The idea behind eigenvalue analysis of the Hessian is to extract the principal directions in which the local second order structure of the image can be decomposed. The eigenvalue decomposition extracts three orthonormal directions which are invariant up to a scaling factor when mapped by the Hessian matrix. In this chapter, λ_k will be the eigenvalue with the k-th smallest magnitude ($|\lambda_1| \leq |\lambda_2| \leq |\lambda_3|$). Under this assumption, Table 3.4 summarizes different structures distinguished by an analysis of the eigenvalues of the Hessian.

Table 3.4: Possible structures on images in 2D and 3D, and its corresponding eigenvalues λ_k . H and L describe the absolute value of λ_k , H is high, L is low, +/- indicate the sign of the eigenvalue. The eigenvalues relationship here is: $|\lambda_1| \leq |\lambda_2| \leq |\lambda_3|$.

2D		3D			Orientation structure
λ_1	λ_2	λ_1	λ_2	λ_3	
L L		L	L	L	noisy structure
		L	L	H-	bright plane-like structure
		L	L	H+	dark plane-like structure
L H-		L	H-	H-	bright tubular-like structure
		L	H+	H+	dark tubular-like structure
H- H-		H-	H-	H-	bright blob-like structure
H+ H+		H+	H+	H+	dark blob-like structure

As shown in Table 3.4, an eigenvector analysis of the Hessian matrix can thus be used to detect fissure-like structures, and the respective eigenvectors point out singular directions. In 3D space, a light plane on a dark background is characterized by one large positive second derivative (λ_3) perpendicular to the fissure plane, since the grey-value increases rapidly from the plane-structure border to the centreline and decreases again to the opposite border. And two small second derivatives of either sign (λ_1 and λ_2) parallel to the plane should occur (shown in Fig 3.10). Thus, on the bright fissures, the ideal relationship is defined as $|\lambda_1| = |\lambda_2| = 0$ and $\lambda_3 \ll 0$, $|\lambda_1| \leq |\lambda_2| \leq |\lambda_3|$. From

these characteristics, we can get a fissure probability of each voxel defined as

$$F_0(s) = \Theta S_{plane} S_{noise}. \quad (3.11)$$

The parameter Θ suppresses points whose largest eigenvalue λ_3 is positive, since fissures are locally bright, and is defined as

$$\Theta = \begin{cases} 1, & \lambda_3 < 0 \\ 0, & \lambda_3 \geq 0. \end{cases} \quad (3.12)$$

Since the largest eigenvalue $|\lambda_3|$ should be much larger than the other two eigenvectors, the second factor S_{plane} uses the ratio between $|\lambda_2|$ and $|\lambda_3|$ to search sheet-like structures, so that the voxels where $|\lambda_3|$ and $|\lambda_2|$ are significantly different.

S_{plane} is defined as

$$S_{plane} = \exp\left(-\frac{R_{plane}^2}{2\alpha^2}\right), \quad (3.13)$$

$$R_{plane} = \frac{|\lambda_2|}{|\lambda_3|}, \quad (3.14)$$

where α was set to 0.5 in this study. The third factor S_{noise} aims to suppress noise voxels such as blob-like structures. Unlike plane-like structures which have relatively large $|\lambda_2|$ and $|\lambda_3|$ ratio, the noise voxels usually have low $|\lambda_1|$, $|\lambda_2|$ and $|\lambda_3|$ (as shown in Table 3.4). Therefore, here we use

$$S_{noise} = 1 - \exp\left(-\frac{R_{noise}^2}{2\beta^2}\right), \quad (3.15)$$

$$R_{noise} = \sqrt{\lambda_1^2 + \lambda_2^2 + \lambda_3^2}, \quad (3.16)$$

with β set to 0.5 for thresholding. $F_0(s)$ then gives a high response to local plane-like structures (fissures) and suppresses other pulmonary structures (noise). An example of this enhancement filter applied in an individual is shown in Figure 3.12a.

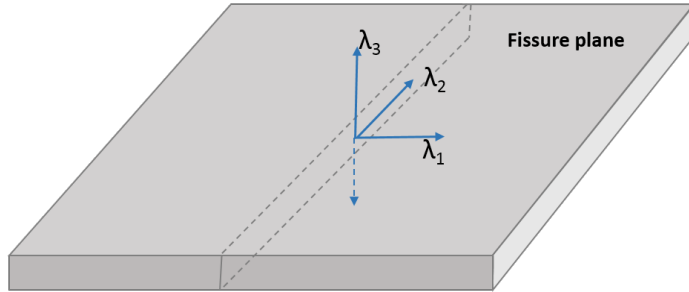


Figure 3.10: The three eigenvectors of the Hessian matrix representing plane-like structure (fissure). λ_1 and λ_2 are parallel to fissure plane, λ_3 is perpendicular to fissure plane.

Blood vessel voxels were subsequently filtered from the fissure enhanced result. The segmentation of vessels was achieved using a classical vessel segmentation method (Frangi et al., 1998). This method uses a multiple scale (from 0.5 mm to 3.0 mm in 0.5 mm increments as the kernel size of Gaussian) Hessian-based enhanced filter, which is similar to the fissure detection filter described previously. The main difference is here the aim is to search for the tube structure (vessels). In a 3D image, the relationship of Hessian eigenvalues λ_1 , λ_2 and λ_3 of an ideal bright tubular structure in a dark background should be described as $|\lambda_1| \approx 0$, $|\lambda_1| \ll |\lambda_2|$, $\lambda_2 \approx \lambda_3$ (see Figure 3.11). Therefore, the following equations were used as the enhancement filter to detect vesselness structures

$$V_0(s) = \begin{cases} 0, & \text{if } \lambda_2 > 0, \\ (1 - \exp(-\frac{R_A^2}{a^2})) \exp(-\frac{R_B^2}{2b^2})(1 - \exp(-\frac{S^2}{2c^2})), & \text{otherwise} \end{cases} \quad (3.17)$$

where a and b were both set to 0.5, and c was set to 500 in this study. R_A , R_B and S are defined as

$$R_A = \frac{|\lambda_2|}{|\lambda_3|}, \quad (3.18)$$

$$R_B = \frac{|\lambda_1|}{\sqrt{|\lambda_2||\lambda_3|}}, \quad (3.19)$$

$$S = \|H\|_F = \sqrt{\sum_{j \leq D} \lambda_j^2}, \quad (3.20)$$

where D is the dimension of the image. $V_0(s)$ gives a probability of vesselness for each voxel. Then segmented blood vessels were selected through detecting the voxels whose vesselness value was larger than a specific threshold (threshold = 10 in this study (Frangi et al., 1998)). D_{vessel} was used to represent the distance transform to the segmented vessel line, thus the final fissureness after decreasing the values of vessel voxels was defined as

$$F_{final}(s) = F_0(s)S_{vessels}, \quad (3.21)$$

$$S_{vessels} = \exp(1 - \frac{D_{vessel}^2}{2d^2}), \quad (3.22)$$

where d was set to 5mm in this study. High vesselness voxels were therefore suppressed

and not detected as fissure points in the final result. Fig 3.12b shows the result after eliminating the vessel voxels.

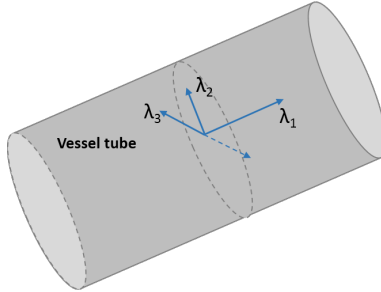


Figure 3.11: The three eigenvectors of the Hessian matrix representing tube-like structure (vessel). λ_1 is parallel to vessel tube, λ_2 and λ_3 are perpendicular to vessel tube.

The initial fissure location predicted by average SSM deformation gives a region of interest (ROI) for an accurate fissure detection, see Figure 3.12c. The candidate points are selected within a certain distance of the initial fissure approximation: the search distance was set to 20 voxels (default value) for the initially projected left and right oblique fissures and 15 voxels for the initially projected right horizontal fissure. To remove some spurious responses such as small plane-like structures on the result, a 2D 4-neighbourhood connected component filter and a 3D 6-neighbourhood vector-based connected component filter were employed successively to eliminate noise arising from small plane-like structures in this search region (Fig 3.12d). A 2D filter was used to eliminate 4-neighbour connected components that were smaller than a minimum small size (set to 10 voxels initially) slice by slice. The 3D vector-based connected component filter used the inner product of the normalized largest eigenvector of the Hessian matrix in adjacent voxels. These largest eigenvectors are perpendicular to the fissure plane, and their inner product provides a criterion for component connection. As the curvature of a fissure is locally low, adjacent fissure voxels should have similar largest eigenvectors

and thus the inner product value of their largest eigenvectors should equal to 1 or slightly smaller than 1. Connected boundary condition was set as an inner product ≤ 0.8 to connected component, then 3D 6-neighbour connected component with a volume less than 100 mm³ was removed as noise from the result.

The detected points were then divided into a set of small subsections corresponding to different x, y intervals. For each subsection, the point of the highest fissure probability (the highest S value) was selected as the final candidate fissure point (Fig 3.12e). Once the maximum fissureness candidates were found, a morphological dilation with a 3 × 3 × 3 voxel cube as structure element was applied iteratively until the largest connected fissure plane was big enough, so that all the other unconnected outliers could be filtered subsequently. Finally, a continuous smooth fissure surface was generated based on the maximum fissure points using a β -spline method with a thin-plane spline (Lee et al., 1997) and extrapolated to the lung boundaries, see Fig 3.12f.

3.3.5 Interactive user control interface

As discussed above, a series of parameter values need to be chosen correctly to ensure a successful lobar segmentation. However, a fixed parameter value is usually not suitable for all the subjects due to a wide variation of lung tissue and fissure appearances across the population. Therefore, a fast and convenient manual interaction to control the segmentation procedure is reasonable and acceptable. Based on an open source software, Pulmonary Toolkit (PTK, <https://github.com/tomdoel/pulmonarytoolkit>), an improved user-friendly interactive interface was developed to control the segmentation parameters as input (improved version: <https://github.com/qiuyufly/pulmonarytoolkit/tree/yuwen>). PTK is a software developed on Matlab for the analysis of 3D medical lung images

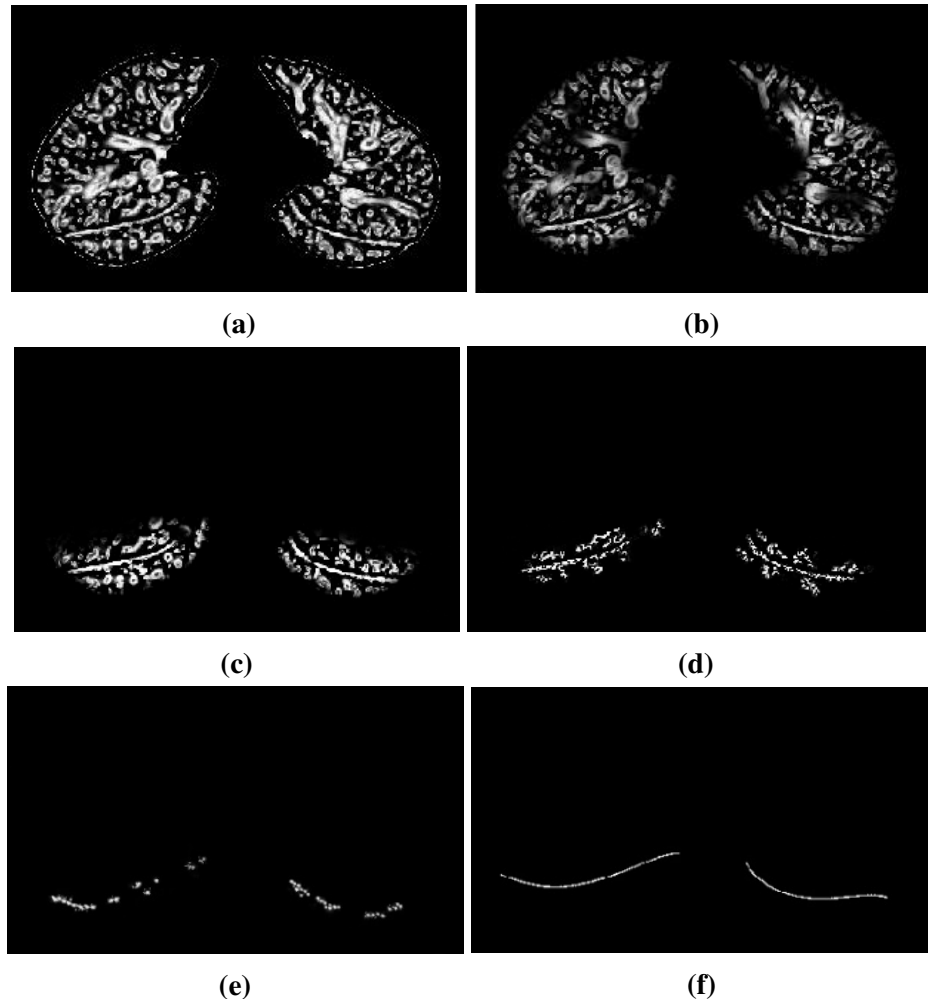


Figure 3.12: Hessian-based multiscale fissure detection results. (a) Hessian-based plane-like structure enhancement filter. (b) Remove vessel voxels (tube-like structures). (c) Selected search regions for fissure detection based on SSM initial fissure prediction. (d) 2D and 3D eigenvector based connected component filter. (e) Fissure candidate points. (f) β -spline curve fissure surface fitting.

for academic research use. It comprises a library of lung analysis algorithms, a GUI application for visualising and analysing clinical lung images and a rapid prototyping framework for users to develop their new algorithms in an easy way. By making use of some built-in objects and the visualisation system of PTK, the lobar segmentation algorithm was added into the algorithm package and parameter control buttons were made available on the interface. Table 3.5 summarises the interactive user control parameters.

Figure 3.13 shows the user interface of PTK.

Table 3.5: Summary of interactive user control parameters

Parameters	Default values	Notes
Search region for left oblique fissure	20 voxels	Increase the value if there are not enough positive candidate points; decrease the value if there is too much noise
Search region for right horizontal fissure	20 voxels	
Search region for right oblique fissure	15 voxels	
Connected component size for left oblique fissure	30 voxels	Decrease the value if there are not enough positive candidate points; increase the value if there is too much noise
Connected component size for right horizontal fissure	30 voxels	
Connected component size for right oblique fissure	30 voxels	
Total connected component size	300 voxels	

Search region control

Fissure candidate points were detected within a certain distance of the initial fissure approximation. The default distance was set to 20 voxels for left and right oblique fissures and 15 voxels for right horizontal fissure. However, with a fixed search distance, fissure detection sometimes could not be implemented efficiently and accurately. The proba-

3.3. METHODS: AUTOMATIC STATISTICAL SHAPE MODEL BASED LOBAR SEGMENTATION METHOD

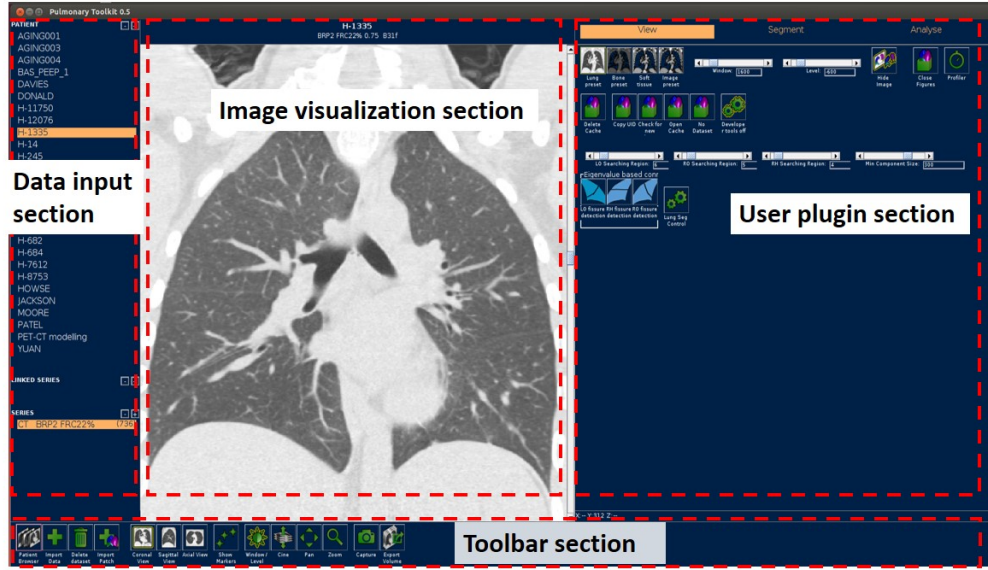


Figure 3.13: PTK User interactive interface. It consists of data input section, image visualization section, user plugin section and toolbar section.

bility of error detection may increase if the search distance is too large, as more noise will be included in the initial search region. In contrast some positive fissure points will be missed if the search distance is too small. Accurate fissure candidate points are an important prerequisite for good fissure surface fitting. Therefore, user interactive slide buttons were developed on the PTK interface to control the search distance. Through inputting SSM based initial fissure prediction mesh, the estimated fissures can be visualized to overlap on the raw images in the PTK visualization section. Then it is possible for users to select a suitable search region for each fissure depending on the accuracy of the initial fissure estimate. The better the initial fissure approximation, the lower the search region that should be selected. Figure 3.14 shows the lobe segmentation result before and after change to the search region.

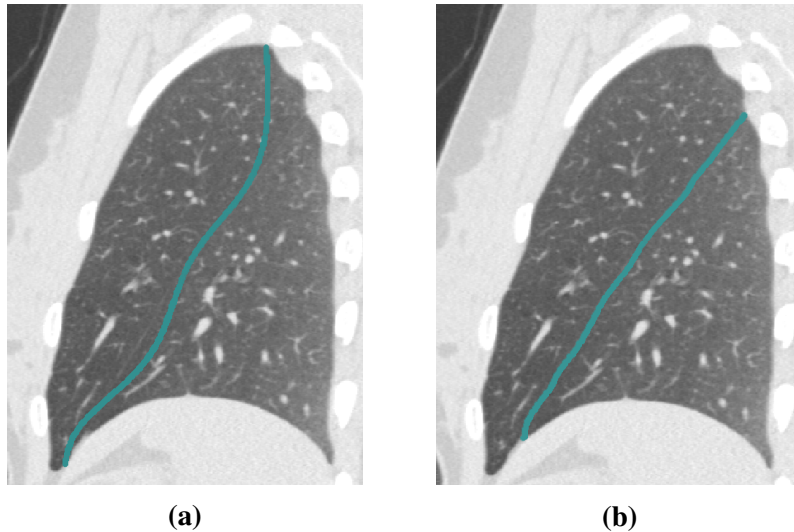


Figure 3.14: Fissure detection results before and after control the search regions. (a) Fissure detection result with a search distance of default 20 voxels. (b) Fissure detection result after setting a specific search distance depending on the accuracy of initial fissure guessing.

Connected component analysis filter control

Connected component analysis is an important operation to help with noise elimination during fissure detection. A suitable connected component size is able to remove most of the small connected structures as outliers and in the meantime retain true fissure structures as much as possible. In order to improve the filter performance, a slide button was used to control the connected component size on the PTK user interface. Through changing the component size threshold, it is possible for us to find a balance between spurious response elimination and target points retainment.

Manual correction

Manual correction remains an essential part of lobe segmentation processing. A manual correction tool was available in the PTK software, but in this method only one correct

landmark could be selected at a time. Here, a multiple landmark correction method was developed based on PTK built-in packages, and the improved correction tool allows users to modify three fissure points at the same time. By selecting a series of correction landmarks, the corresponding fissure plane is deformed to a new curved surface which passes through all the correct landmarks. The correction region was calculated based on the distance between the landmark and its corresponding fissure plane, and a 3D Gaussian filter with the landmark as the centre was also used to specify the corrected boundary. The correction happens in 3D space so that users don't need to do the correction slice by slice. The whole correction can be finished in a few minutes even when automatic fissure is not complete. Figure 3.15 shows the fissure detection results before and after manual correction.

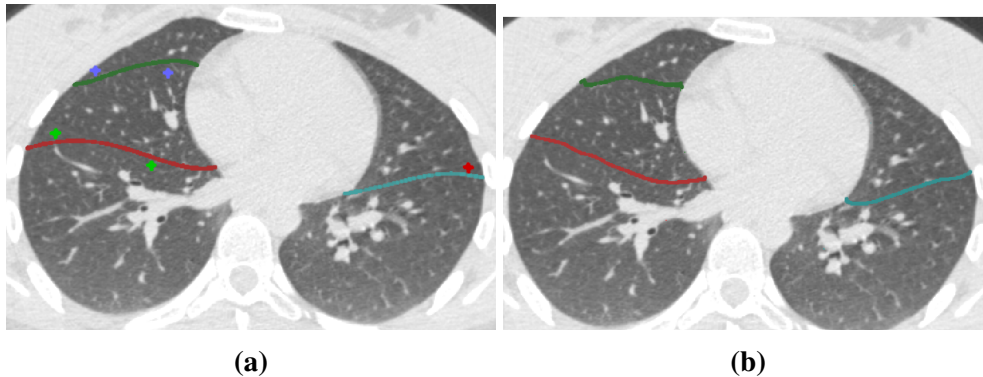


Figure 3.15: Manual correction on automatic fissure detection results (a) Manually select a set of landmarks on real fissure lines shown in raw images to correct automatic fissure detection results (red landmarks are for left oblique fissure, green landmarks are for right oblique fissure, blue landmarks are for right horizontal fissure). (b) Corrected fissure detection results shown with raw images. The corrected fissure lines can match the real fissure locations.

3.4 Results for SMM segmentation

3.4.1 Testing CT dataset

The semi-automatic SSM lobe segmentation method was tested on two datasets: 1) CT images from five young normal subjects taken at different lung volumes (end inspiration and end expiration), in the supine posture, from the HLA dataset (introduced in Section 3.3.2). The selected dataset consists of five end expiration images and five end inspiration images, which were not part of the SSM training set; 2) CT images from older patients (slice thickness 1.25-3.00 mm) acquired during routine diagnostic inspection for idiopathic pulmonary fibrosis (IPF). Data from these subjects were acquired from the Auckland District Health Board (ADHB). Access to clinical data was approved by the Southern Health and Disability Ethics Committee.

3.4.2 Test and results

Figure 3.16 shows raw images, initial SSM based fissure predicted locations, and the final automatic SSM-based lobar segmentation results (no manual correction) for a normal healthy subject. Figure 3.17 shows the results for an IPF subject.

To evaluate the performance of the automatic SSM lobe segmentation, the SSM based method was compared with two anatomical-based lobar segmentation methods. A "gold-standard" manual segmentation of the fissures was used for a quantitative evaluation of the performance. The efficiency of manual correction on the segmentation result was also tested.

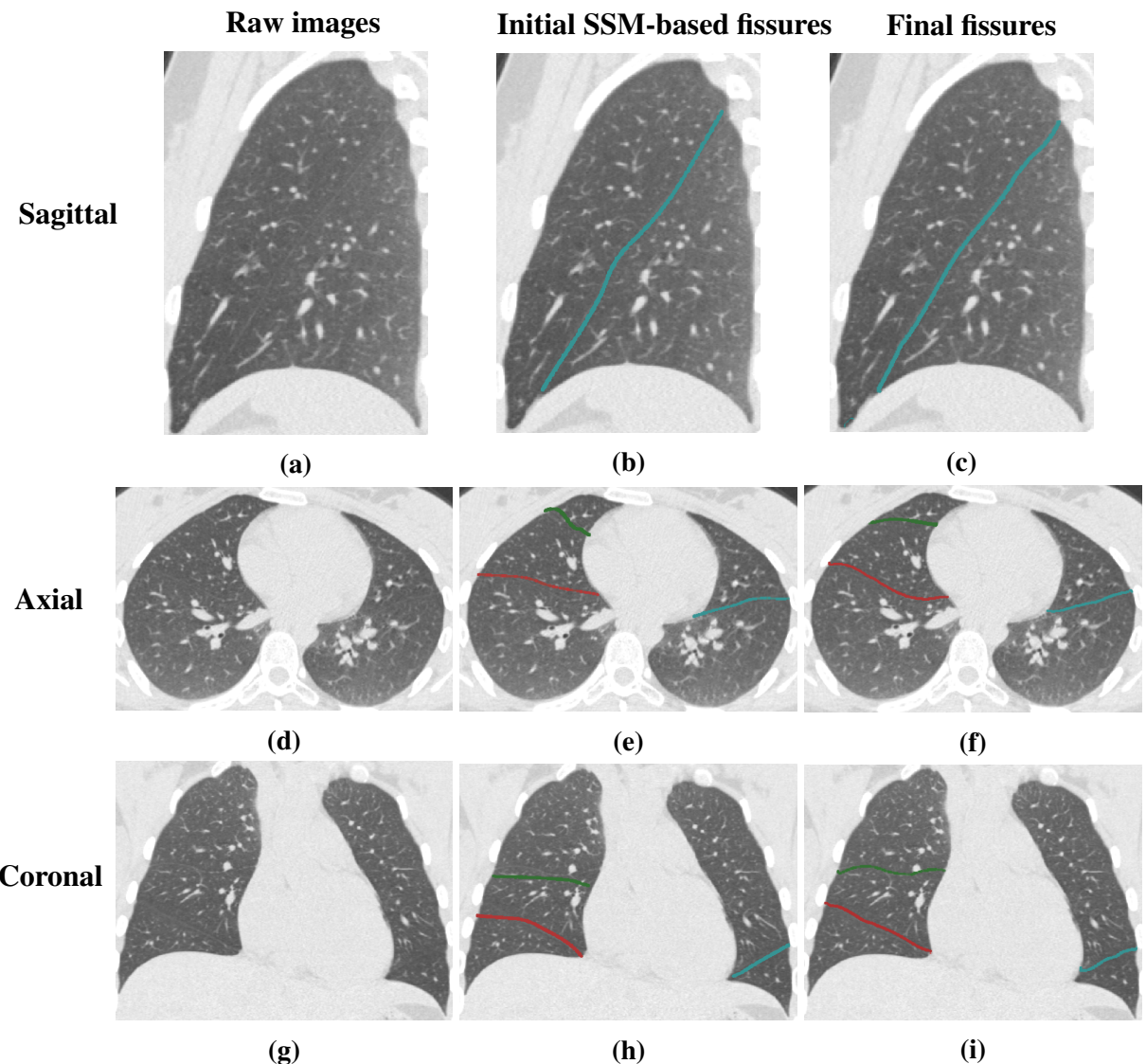


Figure 3.16: Sagittal, axial, and coronal views illustrating raw image, SSM based initial fissure guessing and final automatic fissure detection results of a normal healthy subject. (a), (d), (g) are sagittal, axial and coronal raw images. (b), (e), (h) are sagittal, axial and coronal SSM based initial fissure guessing results. (c), (f), (i) are sagittal, axial and coronal automatic fissure detection results.

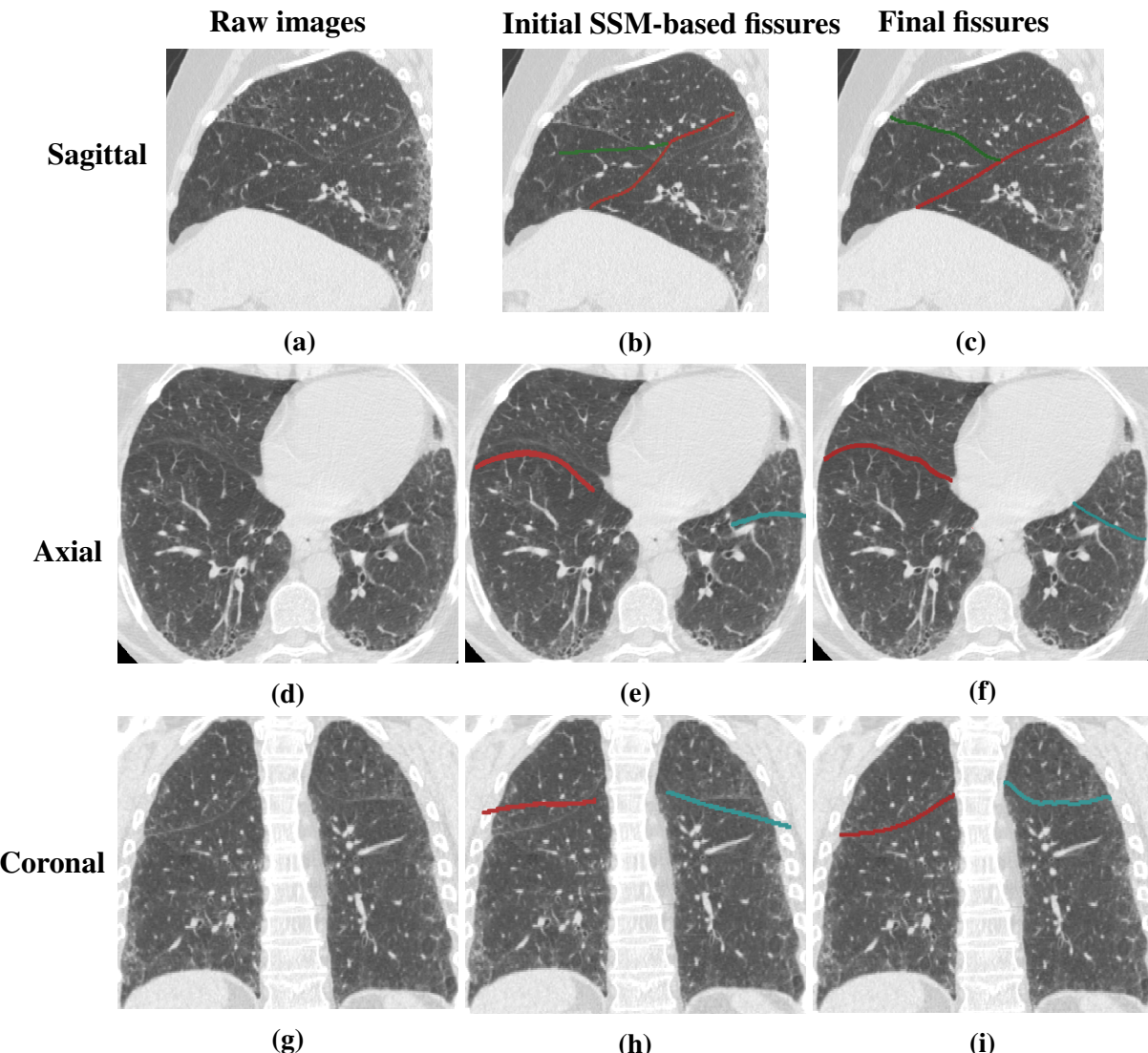


Figure 3.17: Sagittal, axial, and coronal views illustrating raw image, SSM based initial fissure guessing and automatic fissure detection results of an IPF subject. (a), (d), (g) are sagittal, axial and coronal raw images. (b), (e), (h) are sagittal, axial and coronal SSM based initial fissure guessing results. (c), (f), (i) are sagittal, axial and coronal automatic fissure detection results.

The gold standard and quantitative evaluations

To allow for a quantitative evaluation of the performance in a healthy normal dataset and an IPF dataset, the automatic segmentation results were compared with "gold-standard" manual segmentations of the fissures. The "gold-standard" segmentations were acquired by an experienced researcher manually tracing all the three fissures for each subject by digitizing a series of points. The tracing was done on transverse, sagittal and coronal slices to maximise visualisation of the fissures using a custom-written configuration of the open source visualization software CMGUI. The observer can select any of the slice section when digitizing the fissure which can give the best contrast, see Figure 3.7 in section 3.3.2. Fissure detection accuracy was assessed by computing the mean distance between manually-defined fissures points and automatic segmented fissures (with a few manual parameter controls, but without manual correction). For each point in the manual "gold-standard" segmentations, the distance was defined between this point and its closest point in the automatic segmentations as follows:

$$d_i = \min_j \left\{ \sqrt{(x_j^A - x_i^M)^2 + (y_j^A - y_i^M)^2} \right\}, \quad (3.23)$$

where (x_i^A, x_i^M) is the manually traced fissure point, and (x_j^A, x_j^M) is the automatic segmented fissure point. Then the mean error was calculated as:

$$d_{mean} = \frac{\sum_{i=1}^N d_i}{N}, \quad (3.24)$$

where N is the number of points in the manually traced fissure. In addition, the accuracy of the algorithm was evaluated using a percentile measurement. The percentile accuracy is defined as the percentage of the distance between manual and automatic points under

a 3 mm criteria, following the equation:

$$\sqrt{(x_i^A - x_i^M)^2 + (y_i^A - y_i^M)^2} \leq 3 \text{ mm}, \quad (3.25)$$

since 3 mm approximates the thickness of clinical CT images that surgeons and radiologists read in clinical settings (Wei et al., 2009).

For normal subjects, the average mean differences (and accuracies) were 1.76 mm (81%), 3.66 mm (65%), and 2.55 mm (74%), for left oblique, right horizontal and right oblique fissures, respectively. For IPF subjects, the average mean differences (and accuracies) were 2.82 mm (70%), 5.39 mm (59%), and 4.71 mm (63%), for left oblique, right horizontal and right oblique fissures, respectively (shown in Table 3.6).

Table 3.6: Mean error and percentile accuracy of normal healthy and IPF subjects (mean value \pm standard deviation).

	Normal healthy subjects		IPF subjects	
	Mean error (mm)	Accuracy (%)	Mean error (mm)	Accuracy (%)
Left oblique	1.76 \pm 0.68	81.19 \pm 6.61	2.82 \pm 0.71	70.26 \pm 9.10
Right horizontal	3.66 \pm 1.37	64.81 \pm 13.19	5.39 \pm 1.90	58.43 \pm 14.53
Right oblique	2.55 \pm 0.90	73.81 \pm 7.96	4.71 \pm 1.60	62.86 \pm 11.21

Figure 3.18 shows the spatial distribution of error for three representative subjects. Error was highest in regions close to the hilum (where the anatomical structures are complex, and/or the fissure is often incomplete), and where the right fissures meet.

Comparison to anatomical based lobar segmentation method

A marker-based interactive watershed transformation algorithm is a commonly used lobe segmentation method in the current literature (Ukil and Reinhardt, 2009; Pu et al., 2009b; Lassen et al., 2011, 2013). This method mainly relies on anatomical information of the lung which integrates fissures, bronchi and vessels into a cost image

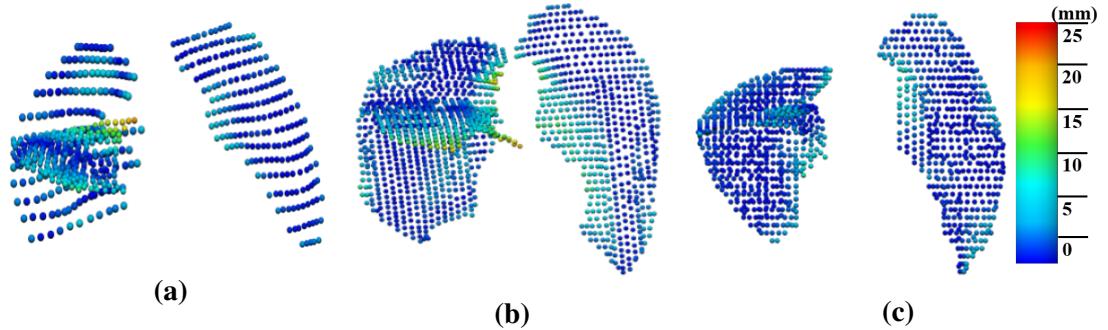


Figure 3.18: The spatial distribution of error between the gold-standard and semi-automatic methods for three representative subjects, highlighting localized regions of low accuracy.

to obtain the lobar boundaries. In the current method, a lobar statistical shape model constructed based on principal component analysis was used to provide an initial estimation of fissure locations. This method gets rid of the dependence on prior segmentation of anatomical structures. To investigate the contribution of using the approximated lobe borders from the deformation of SSM, here the method is compared to two interactive watershed-based pulmonary lobe segmentation softwares: 1. Pulmonary Toolkit, PTK, <https://github.com/tomdoel/pulmonarytoolkit> (introduced in Section 3.3.5); 2. Pulmonary Analysis Software Suite, PASS (Guo et al., 2008). PASS is custom-written software developed at the University of Iowa, that integrates quantitative measurements of lung function and structure analysis. Both of these softwares have a built-in lobe segmentation method which is guided by vessel tree and airway tree.

The two segmentation softwares PASS and PTK tested for comparison were unable to segment the lobes for 9/20 and 7/20 subjects respectively (1/10 and 1/10 normal and 8/10 and 6/10 IPF subjects). In contrast, the model-based method gave an initial estimate for all subjects at all volumes. The main reason for the failure of segmentation is that the airway trees can't be segmented or labelled as lobar branches correctly. Figure

3.19 shows an example of an IPF subject in which airway branches are mislabelled.

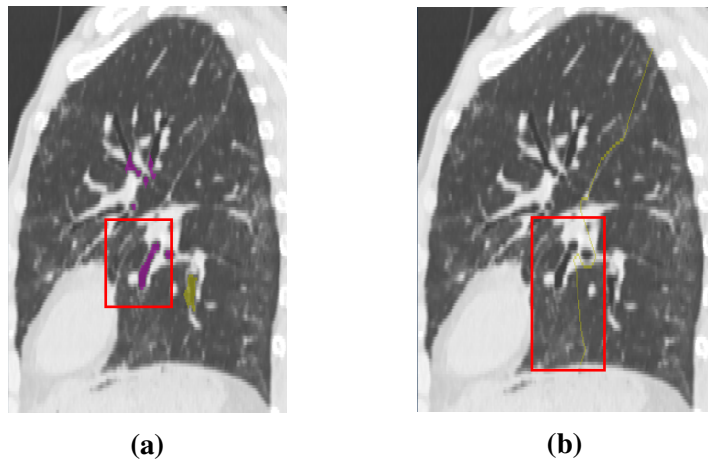


Figure 3.19: An inaccurate initial fissure estimate for an IPF subject caused by mislabeling of lobular airway branches using marker-based interactive watershed transformation algorithm (sagittal view, left lung). (a) The mislabeling of lobular airway branches. Purple is for left upper branches and yellow is for left lower branches. The lower branches in the red box are mis-detected as upper branches. (b) The initial fissure guessing based on the erroneous airway branch labelling result. The approximate fissure has a significant erroneous shift in the red box where mislabelling of lobular airway branches occurs.

The mean square error and percentile accuracy of each fissure for each subject segmented using PTK, PASS and the new method are listed in Table 3.7, 3.8 and 3.9. Although the SSM-based method was able to segment all the subjects (whereas PASS and PTK can't), PASS could sometimes perform better on some young healthy subjects. That is probably because in the healthy lungs, it is possible to extract airways and vessels accurately, therefore these structures are able to provide reliable anatomical information. The SSM-based method had lower error and higher percentage accuracy than PTK for all three fissures for both IPF and normal. Error and accuracy for the SSM-based method were similar to PASS for the healthy subjects, whereas error was much lower and accuracy higher for the SSM-based method applied to IPF data.

Table 3.7: Mean error and percentile accuracy of left oblique fissure for each subject

Subject	SSM-based		PTK		PASS	
	Mean error (mm)	Accuracy (%)	Mean error (mm)	Accuracy (%)	Mean error (mm)	Accuracy (%)
HLA1	0.96	91.3	1.98	77.3	1.14	89.7
HLA2	1.17	85.6	1.58	82.7	0.57	95.9
HLA3	1.74	79.8	3.18	72.9	0.93	92.2
HLA4	2.61	81.2	Fail	Fail	2.65	82.0
HLA5	1.44	81.6	1.25	90.7	Fail	Fail
HLA6	3.31	68.1	3.78	53.6	0.92	96.0
HLA7	1.67	80.2	1.75	77.0	3.54	66.4
HLA8	1.52	83.3	2.99	66.2	2.68	68.0
HLA9	1.20	88.7	5.69	44.3	2.61	70.6
HLA10	2.03	72.2	5.55	49.6	1.89	77.1
Mean ± Std (HLA)	1.76±0.68	81.2±6.6	3.08±1.56	68.2±15.0	1.88±0.98	82.0±11.3
IPF1	1.91	82.0	Fail	Fail	Fail	Fail
IPF2	3.15	62.3	17.90	22.9	Fail	Fail
IPF3	2.71	79.0	Fail	Fail	Fail	Fail
IPF4	3.21	61.8	Fail	Fail	4.21	56.2
IPF5	1.93	78.7	Fail	Fail	Fail	Fail
IPF6	3.27	63.2	6.71	39.2	4.54	58.8
IPF7	4.24	57.7	4.97	44.7	Fail	Fail
IPF8	2.65	62.8	Fail	Fail	Fail	Fail
IPF9	3.27	73.0	Fail	Fail	Fail	Fail
IPF10	1.91	82.1	3.13	71.5	2.96	73.3
Mean ± Std (IPF)	2.82±0.72	70.3±9.1	8.18±5.76	44.6±17.5	3.90±0.68	62.8±7.5

Table 3.8: Mean error and percentile accuracy of right horizontal fissure for each subject

Subject	SSM-based		PTK		PASS	
	Mean error (mm)	Accuracy (%)	Mean error (mm)	Accuracy (%)	Mean error (mm)	Accuracy (%)
HLA1	2.61	72.8	2.32	73.7	1.77	81.6
HLA2	1.55	84.1	3.21	58.3	1.59	86.7
HLA3	3.34	60.9	2.68	72.6	1.31	88.3
HLA4	1.67	84.9	Fail	Fail	1.61	88.6
HLA5	4.89	57.9	10.01	41.7	Fail	Fail
HLA6	3.57	62.6	2.64	65.4	6.38	56.2
HLA7	6.02	39.0	4.20	54.1	Fail	Fail
HLA8	4.09	69.9	6.61	22.8	4.48	39.2
HLA9	5.02	52.9	21.74	21.9	Fail	Fail
HLA10	3.86	63.3	18.04	11.6	13.11	14.5
Mean \pm Std (HLA)	3.66 \pm 1.37	64.8 \pm 13.2	7.94 \pm 6.85	55.5 \pm 16.8	4.32 \pm 3.99	65.0 \pm 27.1
IPF1	3.91	75.1	Fail	Fail	Fail	Fail
IPF2	4.99	67.0	10.60	12.2	Fail	Fail
IPF3	2.19	82.1	Fail	Fail	Fail	Fail
IPF4	4.95	58.7	Fail	Fail	10.09	19.2
IPF5	6.99	49.2	Fail	Fail	Fail	Fail
IPF6	6.21	38.5	41.01	0.5	Fail	Fail
IPF7	6.47	53.6	9.2	19.6	Fail	Fail
IPF8	8.04	41.2	Fail	Fail	Fail	Fail
IPF9	7.52	45.4	Fail	Fail	Fail	Fail
IPF10	2.67	73.6	9.31	34.9	7.56	49.4
Mean \pm Std (IPF)	5.39 \pm 1.90	58.4 \pm 14.5	17.53 \pm 13.57	16.8 \pm 12.4	8.83 \pm 1.26	34.3 \pm 15.1

Table 3.9: Mean error and percentile accuracy of right oblique fissure for each subject

Subject	SSM-based		PTK		PASS	
	Mean error (mm)	Accuracy (%)	Mean error (mm)	Accuracy (%)	Mean error (mm)	Accuracy (%)
HLA1	1.99	79.9	2.54	69.9	1.12	87.7
HLA2	2.03	75.1	2.98	58.1	0.64	96.0
HLA3	1.64	82.4	2.48	72.3	0.66	96.5
HLA4	2.15	82.2	Fail	Fail	1.37	96.4
HLA5	2.07	78.5	3.23	61.4	Fail	Fail
HLA6	4.98	75.7	8.31	45.4	4.93	94.5
HLA7	3.02	55.3	3.17	57.1	3.47	57.8
HLA8	2.33	74.0	3.97	58.9	2.40	71.3
HLA9	3.01	66.6	5.72	50.4	2.89	73.5
HLA10	2.32	68.4	8.61	35.4	2.53	70.7
Mean ± Std (HLA)	2.56±0.91	73.8±7.9	4.56±2.78	56.5±10.9	2.23±1.35	82.7±13.7
IPF1	2.52	81.7	Fail	Fail	Fail	Fail
IPF2	2.94	82.5	3.56	55.4	Fail	Fail
IPF3	3.68	59.5	Fail	Fail	Fail	Fail
IPF4	6.23	59.0	Fail	Fail	49.16	6.1
IPF5	4.14	62.0	Fail	Fail	Fail	Fail
IPF6	5.43	48.4	15.88	23.7	6.86	41.6
IPF7	5.07	57.0	11.66	19.3	Fail	Fail
IPF8	7.33	47.8	Fail	Fail	Fail	Fail
IPF9	6.69	63.5	Fail	Fail	Fail	Fail
IPF10	3.06	67.3	4.53	47.8	3.57	67.1
Mean ± Std (IPF)	4.71±1.60	62.9±11.2	8.91±5.10	36.6±15.4	19.87±20.76	38.3±25.0

Manual correction

In order to test the efficiency of manual correction for segmented fissures, three students (who were able to recognize lobe fissures on raw images accurately) were asked to perform manual corrections on an automatic segmented fissure result, spending no more than ten minutes per subject. Table 3.10 lists the comparison of the segmentation accuracy before and after the ten-minute manual correction.

Table 3.10: Mean square error (MSE) (mm) and percentile accuracy(%) of segmented left oblique (LO), right horizontal (RH), and right oblique (RO) fissures before and after manual correction

	Before correction		After correction					
	MSE	Accuracy	Student 1		Student 2		Student 3	
			MSE	Accuracy	MSE	Accuracy	MSE	Accuracy
LO	3.19	57.55	1.35	89.59	1.21	91.84	1.17	93.47
RH	5.02	39.09	1.85	85.28	1.61	90.36	1.64	87.31
RO	4.83	47.80	1.37	92.67	1.18	89.52	0.98	96.88

3.5 Discussion

In this chapter, a novel pulmonary lobar segmentation method was presented and compared against two existing softwares (PTK and PASS). Results show that the method outperforms both PTK and PASS with respect to the proportion of subjects for whom a segmentation was possible, and the new method had lower error and higher percentage accuracy than both comparison softwares for IPF data. Segmentation error and accuracy for data from healthy subjects was similar to PASS, but outperformed PTK. Due to lower imaging resolution and tissue abnormalities, the accuracy of the method was lower for the IPF subjects than the healthy subjects. However, the method was able to detect a fissure in each case, whereas existing research-focussed software can not,

especially for the abnormal subjects. Automated segmentation of anatomical structures is still challenging in cases with abnormalities, however, the method did not fail, and it provides a robust basis for segmentation even in abnormal cohorts.

For fissure detection, there are usually two types of errors, false negative detection and false positive detection. False negative detection indicates the leak detection of some true fissure points where fissures are incomplete or have fuzzy appearance. False positive detection indicates the mis-detection of some false fissure points where tissues with small plane-like structures are incorrectly identified as fissures. For IPF subjects, both of the errors may occur during fissure detection. The first type of error exists for most of the subjects, since CT-visualized complete pulmonary fissures are rare, especially for IPF CT imaging, which makes automatic lobe segmentation challenging due to the absence of a physical border. In the current method, the β -spline method with thin plane spline-based surface fitting is able to provide an automated correction of the first type of error, since the fitting operation may help to estimate "incomplete" fissures in the correct direction through extrapolating "complete" fissures to lung borders. This fissure fitting method is a commonly used fitting algorithm (Lee et al., 1997; Doel et al., 2012), however the accuracy of the fitting performance is heavily reliant on the correct detection of complete fissures and a good initial approximation of fissure. Therefore, for some IPF subjects with lower fissure completeness, more manual operations may be needed.

For the second type of error, incorrect detection is usually caused by accessory fissures and interstitial lung disease tissues such as scarring or fibrosis. The 2D connected component filter and 3D eigenvector based connected component filter are able to eliminate most of the non-fissure structures within the search region. However, for IPF subjects, it is still difficult to remove all the noise, since fibrosis usually appears surround-

ing the fissures and may even be connected to the main fissure plane. For some terminal stage IPF patients, severe honeycomb and reticular regions make lung parenchyma really fuzzy and low contrast from the fissures which increases the difficulty of avoiding mis-detection.

The new SSM-based method performed better on the left oblique fissure than the other two fissures, likely because the left lung has a simpler anatomic structure with only one fissure. In contrast, error detection happens more often in the area of the right lung where the two fissures come into contact. This is illustrated in Fig 5, which shows the error distribution over the three fissures for three subjects. It can be seen that the method results in higher error in the lung boundary area, since the fissures here are commonly incomplete on CT scans, thus few fissure candidate points can be detected accurately. There is also a high error around the junction area of the right oblique fissure and right horizontal fissure, since the two fissures are too closed in this region and the search regions may overlap with each other.

In the new method, a statistical shape model was used to provide an initial fissure estimate. Compared to the current published anatomical structure-based methods, the model-based method can predict the fissure location without requiring a preliminary analysis of other anatomical features other than lung shape. For example, traditional anatomical knowledge-based methods such as the watershed-based lobar segmentation relies on the success of the automatic segmentations of the vessel and airway tree and need to label the airway trees to the five main lobar bronchi to get an initial fissure approximation. When one of those segmentations fails, the method is likely to perform worse (as shown in Figure 3.19). Vessels are distributed all over the lung and due to the high contrast to the lung parenchyma a good segmentation of the vessels is feasible. But in some cases vessels cross the lobar boundaries. Thus, the assumption that there are no

vessels at the lobar boundary is not always correct (Pu et al., 2009b). On the other hand, due to the complex radiological appearance of pathological lungs, it is usually difficult to get a reliable airway and vessel tree segmentation (Lassen et al., 2011, 2013). In the current method, no watershed-based lobe segmentation can be performed in the case of a failed bronchi segmentation because the required lobe markers are generated from the labelled bronchi tree. In those cases, the approximated lobar borders might be at the wrong location in the scan. In contrast, the new method is largely independent of the knowledge of lung anatomy, so in the comparison of the model-based estimation of fissure location with a watershed-based method, the latter failed for nearly half of the subjects.

The accuracy of the initial fissure prediction is a very important basis for a good segmentation. However, the model-based fissure prediction method still has some limitations. A main disadvantage is that it can only produce lobar shapes close to the shapes represented in the training set, which leads to a larger error in cases where pathological processes had altered the lobe shapes. As shown in Figure 3.16 and 3.17, the SSM based initial fissure estimate usually performs worse in IPF subjects than in normal healthy subjects. In the following chapters, a statistical shape analysis shows that there is a significant shape difference of right middle lobe and right upper lobe between IPF lungs and normal old lungs. That would be a reasonable explanation for the poor estimation of right horizontal fissure and right oblique fissure of the IPF subject shown in Figure 3.17. In the future, a statistical lobar shape model dataset for a variety of pathologies could be developed. A dataset containing a wide range of statistical models for different ages, sexes, lung volume or diseases would be able to help predict a more accurate ROI for fissure detection.

Due to variation in lung anatomy and pulmonary disease, no automatic segmentation

method can ensure a satisfying lobe segmentation result for all cases. Even for a widely used robust lobe segmentation method, it may be impossible to get a highly accurate segmentation result for all subjects, especially for some abnormal subjects. Therefore, manually interactive operation is usually acceptable and involved in a lot of lobe segmentation processing. A combination of an automatic algorithm and manual interaction is an effective way to obtain accurate segmentation. On the one hand, an automatic segmentation algorithm would help researchers save considerable time from laborious and time consuming manual tasks. On the other hand, a fast and intuitive correction is able to improve the automatic segmentation performance within a few minutes.

3.6 Summary

In this chapter, an SSM based lobe segmentation method was developed. Results show that the method can provide a relatively accurate result for most of the IPF subjects, although manual interaction is still needed for some subjects. In the next chapter, the segmented lobe results will be used to construct an FE mesh to describe the lobe shape for each IPF subject. The patient-specific lobe mesh will work as a basic geometry structure to guide a further disease distribution analysis and functional simulation.

List of References

- Agustí, A. G., Roca, J., Gea, J., Wagner, P. D., Xaubet, A., and Rodriguez-Roisin, R. (1991). Mechanisms of gas-exchange impairment in idiopathic pulmonary fibrosis. *American Review of Respiratory Disease*, 143(2):219–225. [Cited on pages 30 and 32.]
- Agusti, C., Xaubet, A., Agusti, A., Roca, J., Ramirez, J., and Rodriguez-Roisin, R. (1994). Clinical and functional assessment of patients with idiopathic pulmonary fibrosis: results of a 3 year follow-up. *European Respiratory Journal*, 7(4):643–650. [Cited on page 30.]
- Ahluwalia, N., Shea, B. S., and Tager, A. M. (2014). New therapeutic targets in idiopathic pulmonary fibrosis. aiming to rein in runaway wound-healing responses. *American journal of respiratory and critical care medicine*, 190(8):867–878. [Cited on page 8.]
- Alder, J. K., Chen, J. J.-L., Lancaster, L., Danoff, S., Su, S.-c., Cogan, J. D., Vulto, I., Xie, M., Qi, X., Tuder, R. M., et al. (2008). Short telomeres are a risk factor for idiopathic pulmonary fibrosis. *Proceedings of the National Academy of Sciences*, 105(35):13051–13056. [Cited on page 12.]
- Allam, J. S. and Limper, A. H. (2006). Idiopathic pulmonary fibrosis: is it a familial disease? *Current opinion in pulmonary medicine*, 12(5):312–317. [Cited on page 12.]
- Ambrosini, V., Cancellieri, A., Chilosi, M., Zompatori, M., Trisolini, R., Saragoni, L.,

- and Poletti, V. (2003). Acute exacerbation of idiopathic pulmonary fibrosis: report of a series. *European Respiratory Journal*, 22(5):821–826. [Cited on page 20.]
- Armato, S. G. and Sensakovic, W. F. (2004). Automated lung segmentation for thoracic ct: Impact on computer-aided diagnosis1. *Academic Radiology*, 11(9):1011–1021. [Cited on page 43.]
- Azuma, A., Nukiwa, T., Tsuboi, E., Suga, M., Abe, S., Nakata, K., Taguchi, Y., Nagai, S., Itoh, H., Ohi, M., et al. (2005). Double-blind, placebo-controlled trial of pirfenidone in patients with idiopathic pulmonary fibrosis. *American journal of respiratory and critical care medicine*, 171(9):1040–1047. [Cited on page 20.]
- Baumgartner, K. B., Samet, J. M., Stidley, C. A., Colby, T. V., and Waldron, J. A. (1997). Cigarette smoking: a risk factor for idiopathic pulmonary fibrosis. *American journal of respiratory and critical care medicine*, 155(1):242–248. [Cited on page 11.]
- Bjoraker, J. A., Ryu, J. H., Edwin, M. K., Myers, J. L., Tazelaar, H. D., Schroeder, D. R., and Offord, K. P. (1998). Prognostic significance of histopathologic subsets in idiopathic pulmonary fibrosis. *American journal of respiratory and critical care medicine*, 157(1):199–203. [Cited on page 19.]
- Bradley, C., Pullan, A., and Hunter, P. (1997). Geometric modeling of the human torso using cubic hermite elements. *Annals of biomedical engineering*, 25(1):96–111. [Cited on page 59.]
- Carrington, C. B., Gaensler, E. A., Coutu, R. E., FitzGerald, M. X., and Gupta, R. G. (1978). Natural history and treated course of usual and desquamative interstitial pneumonia. *New England Journal of Medicine*, 298(15):801–809. [Cited on page 19.]
- Cherniack, R. M., Colby, T. V., Flint, A., Thurlbeck, W. M., Waldron Jr, J. A., Ackerson, L., Schwarz, M. I., and King Jr, T. E. (1995). Correlation of structure and function

- in idiopathic pulmonary fibrosis. *American journal of respiratory and critical care medicine*, 151(4):1180–1188. [Cited on page 27.]
- Chilosi, M., Poletti, V., Murer, B., Lestani, M., Cancellieri, A., Montagna, L., Piccoli, P., Cangi, G., Semenzato, G., and Doglioni, C. (2002). Abnormal re-epithelialization and lung remodeling in idiopathic pulmonary fibrosis: the role of δ n-p63. *Laboratory investigation*, 82(10):1335. [Cited on page 27.]
- Cootes, T. F., Taylor, C. J., Cooper, D. H., and Graham, J. (1995). Active shape models—their training and application. *Computer vision and image understanding*, 61(1):38–59. [Cited on page 56.]
- Corte, T. J., Collard, H., and Wells, A. U. (2015). Idiopathic interstitial pneumonias in 2015: A new era. *Respirology*, 20(5):697–698. [Cited on page 9.]
- Cortes-Telles, A., Forkert, L., O'Donnell, D. E., and Morán-Mendoza, O. (2014). Idiopathic pulmonary fibrosis: New insights to functional characteristics at diagnosis. *Canadian respiratory journal*, 21(3):e55–e60. [Cited on pages 24 and 30.]
- Cosgrove, G. P., Brown, K. K., Schiemann, W. P., Serls, A. E., Parr, J. E., Geraci, M. W., Schwarz, M. I., Cool, C. D., and Worthen, G. S. (2004). Pigment epithelium-derived factor in idiopathic pulmonary fibrosis: a role in aberrant angiogenesis. *American journal of respiratory and critical care medicine*, 170(3):242–251. [Cited on page 28.]
- Cottin, V., Le Pavec, J., Prévot, G., Mal, H., Humbert, M., Simonneau, G., Cordier, J.-F., et al. (2010). Pulmonary hypertension in patients with combined pulmonary fibrosis and emphysema syndrome. *European Respiratory Journal*, 35(1):105–111. [Cited on page 22.]
- Cottin, V., Nunes, H., Brillet, P., Delaval, P., Devouassoux, G., Tillie-Leblond, I., Israel-Biet, D., Valeyre, D., Cordier, J., et al. (2005). Combined pulmonary fibro-

- sis and emphysema: a distinct underrecognised entity. *European Respiratory Journal*, 26(4):586–593. [Cited on page 22.]
- Coxson, H. (2007). Computed tomography and monitoring of emphysema. [Cited on page 38.]
- Crapo, R. (1993). The aging lung. *Lung biology in health and disease*, 63:1–25. [Cited on page 55.]
- Crystal, R. G., Fulmer, J. D., Roberts, W. C., Moss, M. L., Line, B. R., and Reynolds, H. Y. (1976). Idiopathic pulmonary fibrosis: clinical, histologic, radiographic, physiologic, scintigraphic, cytologic, and biochemical aspects. *Annals of internal medicine*, 85(6):769–788. [Cited on pages 24, 28, 29, 30, 31, and 32.]
- Diaz, A. A., Valim, C., Yamashiro, T., EstŠpar, R. S. J., Ross, J. C., Matsuoka, S., Bartholmai, B., Hatabu, H., Silverman, E. K., and Washko, G. R. (2010). Airway count and emphysema assessed by chest ct imaging predicts clinical outcome in smokers. *CHEST Journal*, 138(4):880–887. [Cited on page 38.]
- Doel, T., Gavaghan, D. J., and Grau, V. (2015). Review of automatic pulmonary lobe segmentation methods from ct. *Computerized Medical Imaging and Graphics*, 40:13–29. [Cited on pages xiii, 36, 37, and 40.]
- Doel, T., Matin, T. N., Gleeson, F. V., Gavaghan, D. J., and Grau, V. (2012). Pulmonary lobe segmentation from ct images using fissureness, airways, vessels and multilevel b-splines. In *Biomedical Imaging (ISBI), 2012 9th IEEE International Symposium on*, pages 1491–1494. IEEE. [Cited on pages 48, 49, 50, 51, 52, and 89.]
- Doherty, M., Pearson, M., O’grady, E., Pellegrini, V., and Calverley, P. (1997). Cryptogenic fibrosing alveolitis with preserved lung volumes. *Thorax*, 52(11):998–1002. [Cited on page 27.]

- Douglas, W. W., Ryu, J. H., and Schroeder, D. R. (2000). Idiopathic pulmonary fibrosis: impact of oxygen and colchicine, prednisone, or no therapy on survival. *American journal of respiratory and critical care medicine*, 161(4):1172–1178. [Cited on pages 13 and 14.]
- Dryden, I. L. and Mardia, K. V. (1998). *Statistical shape analysis*, volume 4. Wiley Chichester. [Cited on pages 56 and 59.]
- Du Bois, R. M., Weycker, D., Albera, C., Bradford, W. Z., Costabel, U., Kartashov, A., Lancaster, L., Noble, P. W., Raghu, G., Sahn, S. A., et al. (2011). Ascertainment of individual risk of mortality for patients with idiopathic pulmonary fibrosis. *American journal of respiratory and critical care medicine*, 184(4):459–466. [Cited on page 27.]
- Ebina, M., Shimizukawa, M., Shibata, N., Kimura, Y., Suzuki, T., Endo, M., Sasano, H., Kondo, T., and Nukiwa, T. (2004). Heterogeneous increase in cd34-positive alveolar capillaries in idiopathic pulmonary fibrosis. *American journal of respiratory and critical care medicine*, 169(11):1203–1208. [Cited on page 28.]
- Ecabert, O., Peters, J., Schramm, H., Lorenz, C., von Berg, J., Walker, M. J., Vembar, M., Olszewski, M. E., Subramanyan, K., Lavi, G., et al. (2008). Automatic model-based segmentation of the heart in ct images. *IEEE transactions on medical imaging*, 27(9):1189–1201. [Cited on page 56.]
- El-Baz, A., Beache, G. M., Gimel'farb, G., Suzuki, K., Okada, K., Elnakib, A., Soliman, A., and Abdollahi, B. (2013). Computer-aided diagnosis systems for lung cancer: challenges and methodologies. *International journal of biomedical imaging*, 2013. [Cited on page 38.]
- Fernandez, J. W. (2004). An anatomically based finite element model of patella articulation: towards a diagnostic tool. PhD thesis, University of Auckland. [Cited on page 59.]

- Finley, T., Swenson, E., and Comroe, J. (1962). The cause of arterial hypoxemia at rest in patients with “alveolar-capillary block syndrome”. *The Journal of clinical investigation*, 41(3):618–622. [Cited on page 32.]
- Flaherty, K., Thwaite, E., Kazerooni, E., Gross, B., Toews, G., Colby, T. V., Travis, W., Mumford, J., Murray, S., Flint, A., et al. (2003). Radiological versus histological diagnosis in uip and nsip: survival implications. *Thorax*, 58(2):143–148. [Cited on page 17.]
- Flaherty, K., Toews, G., Travis, W., Colby, T., Kazerooni, E., Gross, B., Jain, A., Strawderman, R., Paine, R., Flint, A., et al. (2002). Clinical significance of histological classification of idiopathic interstitial pneumonia. *European Respiratory Journal*, 19(2):275–283. [Cited on page 19.]
- Flaherty, K. R., King Jr, T. E., Raghu, G., Lynch III, J. P., Colby, T. V., Travis, W. D., Gross, B. H., Kazerooni, E. A., Toews, G. B., Long, Q., et al. (2004). Idiopathic interstitial pneumonia: what is the effect of a multidisciplinary approach to diagnosis? *American journal of respiratory and critical care medicine*, 170(8):904–910. [Cited on page 12.]
- Florack, L. M., ter Haar Romeny, B. M., Koenderink, J. J., and Viergever, M. A. (1992). Scale and the differential structure of images. *Image and vision computing*, 10(6):376–388. [Cited on page 65.]
- Frangi, A. F., Niessen, W. J., Vincken, K. L., and Viergever, M. A. (1998). Multiscale vessel enhancement filtering. In *International Conference on Medical Image Computing and Computer-Assisted Intervention*, pages 130–137. Springer. [Cited on pages 48, 51, 65, 69, and 70.]
- Fulmer, J., Roberts, W., von Gal, E. R., and Crystal, R. (1979). Morphologic-physiologic correlates of the severity of fibrosis and degree of cellularity in idiopathic

- pulmonary fibrosis. *The Journal of clinical investigation*, 63(4):665–676. [Cited on page 26.]
- Fulmer, J. D., Crystal, R. G., and Roberts, W. C. (1976). Diffuse fibrotic lung disease: a correlative study. *Chest*, 69(2):263–265. [Cited on page 30.]
- Graham, B. L., Brusasco, V., Burgos, F., Cooper, B. G., Jensen, R., Kendrick, A., MacIntyre, N. R., Thompson, B. R., and Wanger, J. (2017). 2017 ers/ats standards for single-breath carbon monoxide uptake in the lung. *European Respiratory Journal*, 49(1):1600016. [Cited on page 30.]
- Graham, M. W., Gibbs, J. D., Cornish, D. C., and Higgins, W. E. (2010). Robust 3-d airway tree segmentation for image-guided peripheral bronchoscopy. *IEEE transactions on medical imaging*, 29(4):982–997. [Cited on page 38.]
- Gross, P. (1962). The concept of the hamman-rich syndrome: a critique. *American Review of Respiratory Disease*, 85(6):828–832. [Cited on page 20.]
- Gross, T. J. and Hunninghake, G. W. (2001). Idiopathic pulmonary fibrosis. *New England Journal of Medicine*, 345(7):517–525. [Cited on page 19.]
- Gülsün, M., Arıyürek, O. M., Cömert, R. B., and Karabulut, N. (2006). Variability of the pulmonary oblique fissures presented by high-resolution computed tomography. *Surgical and Radiologic Anatomy*, 28(3):293–299. [Cited on page 40.]
- Gunther, A., Schmidt, R., Nix, F., Yabut-Perez, M., Guth, C., Rousseau, S., Siebert, C., Grimminger, F., Morr, H., Velcovsky, H., et al. (1999). Surfactant abnormalities in idiopathic pulmonary fibrosis, hypersensitivity pneumonitis and sarcoidosis. *European Respiratory Journal*, 14(3):565–573. [Cited on pages 24 and 26.]
- Guo, J., Fuld, M., Alford, S., Reinhardt, J., and Hoffman, E. (2008). Pulmonary analysis software suite 9.0: Integrating quantitative measures of function with structural anal-

- yses. In First International Workshop on Pulmonary Image Analysis, pages 283–292. [Cited on page 83.]
- Hamada, K., Nagai, S., Tanaka, S., Handa, T., Shigematsu, M., Nagao, T., Mishima, M., Kitaichi, M., and Izumi, T. (2007). Significance of pulmonary arterial pressure and diffusion capacity of the lung as prognosticator in patients with idiopathic pulmonary fibrosis. *Chest*, 131(3):650–656. [Cited on page 30.]
- Hansell, D. M., Bankier, A. A., MacMahon, H., McLoud, T. C., Muller, N. L., and Remy, J. (2008). Fleischner society: glossary of terms for thoracic imaging. *Radiology*, 246(3):697–722. [Cited on page 14.]
- Harari, S., Madotto, F., Caminati, A., Conti, S., and Cesana, G. (2016). Epidemiology of idiopathic pulmonary fibrosis in northern italy. *PLoS One*, 11(2):e0147072. [Cited on page 21.]
- Hayes Jr, D., Black, S. M., Tobias, J. D., Kirkby, S., Mansour, H. M., and Whitson, B. A. (2016). Influence of pulmonary hypertension on patients with idiopathic pulmonary fibrosis awaiting lung transplantation. *The Annals of thoracic surgery*, 101(1):246–252. [Cited on page 23.]
- Hedlund, L., Anderson, R. F., Goulding, P., Beck, J., Effmann, E., and Putman, C. (1982). Two methods for isolating the lung area of a ct scan for density information. *Radiology*, 144(2):353–357. [Cited on pages 42 and 43.]
- Heimann, T. and Meinzer, H.-P. (2009). Statistical shape models for 3d medical image segmentation: a review. *Medical image analysis*, 13(4):543–563. [Cited on page 56.]
- Hempleman, S. C. and Hughes, J. (1991). Estimating exercise dlo₂ and diffusion limitation in patients with interstitial fibrosis. *Respiration physiology*, 83(2):167–178. [Cited on page 32.]

- Hoffman, E. A. (1985). Effect of body orientation on regional lung expansion: a computed tomographic approach. *Journal of Applied Physiology*, 59(2):468–480. [Cited on page 43.]
- Hoffman, E. A. and McLennan, G. (1997). Assessment of the pulmonary structure-function relationship and clinical outcomes measures: quantitative volumetric ct of the lung. *Academic radiology*, 4(11):758–776. [Cited on page 37.]
- Hoffman, E. A. and Ritman, E. L. (1985). Effect of body orientation on regional lung expansion in dog and sloth. *Journal of Applied Physiology*, 59(2):481–491. [Cited on pages 42 and 43.]
- Hoffman, E. A., Simon, B. A., and McLennan, G. (2006). State of the art. a structural and functional assessment of the lung via multidetector-row computed tomography: phenotyping chronic obstructive pulmonary disease. *Proceedings of the American Thoracic Society*, 3(6):519–532. [Cited on page 38.]
- Hoffman, E. A., Sinak, L., Robb, R. A., and Ritman, E. L. (1983). Noninvasive quantitative imaging of shape and volume of lungs. *Journal of Applied Physiology*, 54(5):1414–1421. [Cited on pages 42 and 43.]
- Hu, S., Hoffman, E. A., and Reinhardt, J. M. (2001). Automatic lung segmentation for accurate quantitation of volumetric x-ray ct images. *IEEE transactions on medical imaging*, 20(6):490–498. [Cited on pages 38, 40, 42, and 43.]
- Hughes, J., Lockwood, D., Jones, H., and Clark, R. (1991). Dlco/q and diffusion limitation at rest and on exercise in patients with interstitial fibrosis. *Respiration physiology*, 83(2):155–166. [Cited on page 32.]
- Hunninghake, G. W., Zimmerman, M. B., Schwartz, D. A., KING JR, T. E., Lynch, J., Hegele, R., Waldron, J., Colby, T., Muller, N., Lynch, D., et al. (2001). Utility of a

- lung biopsy for the diagnosis of idiopathic pulmonary fibrosis. *American journal of respiratory and critical care medicine*, 164(2):193–196. [Cited on page 17.]
- Hwang, J.-H., Misumi, S., Sahin, H., Brown, K. K., Newell, J. D., and Lynch, D. A. (2009). Computed tomographic features of idiopathic fibrosing interstitial pneumonitis: comparison with pulmonary fibrosis related to collagen vascular disease. *Journal of computer assisted tomography*, 33(3):410–415. [Cited on page 14.]
- Hyldgaard, C., Hilberg, O., Muller, A., and Bendstrup, E. (2014). A cohort study of interstitial lung diseases in central denmark. *Respiratory medicine*, 108(5):793–799. [Cited on page 10.]
- Jacob, J., Bartholmai, B. J., Rajagopalan, S., Brun, A. L., Egashira, R., Karwoski, R., Kokosi, M., Wells, A. U., and Hansell, D. M. (2016a). Evaluation of computer-based computer tomography stratification against outcome models in connective tissue disease-related interstitial lung disease: a patient outcome study. *Bmc Medicine*, 14(1):190. [Cited on page 28.]
- Jacob, J., Bartholmai, B. J., Rajagopalan, S., Kokosi, M., Nair, A., Karwoski, R., Walsh, S. L., Wells, A. U., and Hansell, D. M. (2016b). Mortality prediction in ipf: evaluation of automated computer tomographic analysis with conventional severity measures. *European Respiratory Journal*, 49(1):ERJ–01011–2016. [Cited on page 29.]
- Jeffery, P. K. (1998). Structural and inflammatory changes in copd: a comparison with asthma. *Thorax*, 53(2):129. [Cited on page 38.]
- Johkoh, T., Muller, N. L., Cartier, Y., Kavanagh, P. V., Hartman, T. E., Akira, M., Ichikado, K., Ando, M., and Nakamura, H. (1999). Idiopathic interstitial pneumonias: diagnostic accuracy of thin-section ct in 129 patients. *Radiology*, 211(2):555–560. [Cited on page 14.]

- Jones, N., McHardy, G., Naimark, A., and Campbell, E. (1966). Physiological dead space and alveolar-arterial gas pressure differences during exercise. *Clinical science*, 31(1):19–29. [Cited on page 31.]
- Kalender, W. A., Fichte, H., Bautz, W., and Skalej, M. (1991). Semiautomatic evaluation procedures for quantitative ct of the lung. *Journal of computer assisted tomography*, 15(2):248–255. [Cited on pages 42 and 43.]
- Katzenstein, A.-L. A. and Myers, J. L. (1998). Idiopathic pulmonary fibrosis: clinical relevance of pathologic classification. *American journal of respiratory and critical care medicine*, 157(4):1301–1315. [Cited on page 9.]
- Kelemen, A., Székely, G., and Gerig, G. (1999). Elastic model-based segmentation of 3-d neuroradiological data sets. *IEEE Transactions on medical imaging*, 18(10):828–839. [Cited on page 56.]
- Keller, J. M., Edwards, F. M., and Rundle, R. (1981). Automatic outlining of regions on ct scans. *Journal of Computer Assisted Tomography*, 5(2):240–245. [Cited on pages 42 and 43.]
- Kemerink, G. J., Lamers, R. J., Pellis, B. J., Kruize, H. H., and Van Engelshoven, J. (1998). On segmentation of lung parenchyma in quantitative computed tomography of the lung. *Medical Physics*, 25(12):2432–2439. [Cited on pages 42 and 43.]
- Kim, D., Park, J., Park, B., Lee, J., Nicholson, A., and Colby, T. (2006a). Acute exacerbation of idiopathic pulmonary fibrosis: frequency and clinical features. *European Respiratory Journal*, 27(1):143–150. [Cited on page 20.]
- Kim, D. S., Collard, H. R., and King Jr, T. E. (2006b). Classification and natural history of the idiopathic interstitial pneumonias. *Proceedings of the American Thoracic Society*, 3(4):285–292. [Cited on pages 19 and 20.]

- Kim, H. J., Perlman, D., and Tomic, R. (2015). Natural history of idiopathic pulmonary fibrosis. *Respiratory medicine*, 109(6):661–670. [Cited on pages 8 and 21.]
- King, C. S. and Nathan, S. D. (2017). Idiopathic pulmonary fibrosis: effects and optimal management of comorbidities. *The Lancet Respiratory Medicine*, 5(1):72–84. [Cited on pages 21 and 23.]
- King Jr, T. E., Pardo, A., and Selman, M. (2011). Idiopathic pulmonary fibrosis. *The Lancet*, 378(9807):1949–1961. [Cited on pages xiii, 1, 7, 8, 12, 13, 14, 16, 19, 20, 21, 22, 23, and 24.]
- KING JR, T. E., Schwarz, M. I., Brown, K., Tooze, J. A., Colby, T. V., WALDRON JR, J. A., Flint, A., Thurlbeck, W., and Cherniack, R. M. (2001). Idiopathic pulmonary fibrosis: relationship between histopathologic features and mortality. *American journal of respiratory and critical care medicine*, 164(6):1025–1032. [Cited on page 19.]
- King Jr, T. E., Tooze, J. A., Schwarz, M. I., BROWN, K. R., and CHERNIACK, R. M. (2001). Predicting survival in idiopathic pulmonary fibrosis: scoring system and survival model. *American journal of respiratory and critical care medicine*, 164(7):1171–1181. [Cited on page 13.]
- Kitasaka, T., Mori, K., Hasegawa, J.-i., and Toriwaki, J.-i. (2003). Lung area extraction from 3d chest x-ray ct images using a shape model generated by a variable bézier surface. *Systems and Computers in Japan*, 34(4):60–71. [Cited on pages 42 and 45.]
- Kitasaka, T., Nakada, Y., Mori, K., Suenaga, Y., Mori, M., Takabatake, H., and Natori, H. (2006). Recognition of lung lobes and its application to the bronchial structure analysis. In *Pattern Recognition, 2006. ICPR 2006. 18th International Conference on*, volume 3, pages 288–291. IEEE. [Cited on page 51.]
- Koenderink, J. J. (1984). The structure of images. *Biological cybernetics*, 50(5):363–370. [Cited on page 65.]

- Kondoh, Y., Taniguchi, H., Kataoka, K., Keisuke, K., Suzuki, R., Ogura, T., Johkoh, T., Yokoi, T., Wells, A. U., and Kitaichi, M. (2010). Prognostic factors in rapidly progressive interstitial pneumonia. *Respirology*, 15(2):257–264. [Cited on page 20.]
- Kondoh, Y., Taniguchi, H., Kawabata, Y., Yokoi, T., Suzuki, K., and Takagi, K. (1993). Acute exacerbation in idiopathic pulmonary fibrosis: analysis of clinical and pathologic findings in three cases. *Chest*, 103(6):1808–1812. [Cited on page 20.]
- Korfiatis, P., Kalogeropoulou, C., Karahaliou, A., Kazantzi, A., Skiadopoulos, S., and Costaridou, L. (2008). Texture classification-based segmentation of lung affected by interstitial pneumonia in high-resolution ct. *Medical physics*, 35(12):5290–5302. [Cited on page 45.]
- Kornbluth, R. and Turino, G. (1980). Respiratory control in diffuse interstitial lung disease and diseases of the pulmonary vasculature. *Clinics in chest medicine*, 1(1):91–102. [Cited on page 28.]
- Kreuter, M., Ehlers-Tenenbaum, S., Palmowski, K., Bruhwyler, J., Oltmanns, U., Muley, T., Heussel, C. P., Warth, A., Kolb, M., and Herth, F. J. (2016). Impact of comorbidities on mortality in patients with idiopathic pulmonary fibrosis. *PLoS One*, 11(3):e0151425. [Cited on page 21.]
- Krumpe, P. E., Knudson, R. J., Parsons, G., and Reiser, K. (1985). The aging respiratory system. *Clinics in geriatric medicine*, 1(1):143–175. [Cited on page 55.]
- Kuhnigk, J., Dicken, V., Zidowitz, S., Bornemann, L., Kuemmerlen, B., Krass, S., Peitgen, H., Yuval, S., Jend, H., Rau, W., et al. (2005). Informatics in radiology (inforad): New tools for computer assistance in thoracic ct. part 1. functional analysis of lungs. Lung Lobes, and Bronchopulmonary Segments. *RadioGraphics* 2005; 25: 525, 536. [Cited on pages 48, 49, and 50.]

- Kuhnigk, J.-M., Hahn, H., Hindennach, M., Dicken, V., Krass, S., and Peitgen, H.-O. (2003). Lung lobe segmentation by anatomy-guided 3 d watershed transform. In Proceedings of SPIE, volume 5032, pages 1482–1490. [Cited on pages 48, 49, and 50.]
- Lassen, B., Kuhnigk, J.-M., Friman, O., Krass, S., and Peitgen, H.-O. (2010). Automatic segmentation of lung lobes in ct images based on fissures, vessels, and bronchi. In Biomedical Imaging: From Nano to Macro, 2010 IEEE International Symposium on, pages 560–563. IEEE. [Cited on pages 36, 48, 49, and 50.]
- Lassen, B., Kuhnigk, J.-M., Van Rikxoort, E. M., and Peitgen, H.-O. (2011). Interactive lung lobe segmentation and correction in tomographic images. In Medical Imaging 2011: Computer-Aided Diagnosis, volume 7963, page 79631S. International Society for Optics and Photonics. [Cited on pages 35, 48, 51, 52, 82, and 91.]
- Lassen, B., van Rikxoort, E. M., Schmidt, M., Kerkstra, S., van Ginneken, B., and Kuhnigk, J.-M. (2013). Automatic segmentation of the pulmonary lobes from chest ct scans based on fissures, vessels, and bronchi. IEEE transactions on medical imaging, 32(2):210–222. [Cited on pages 48, 51, 52, 82, and 91.]
- Leader, J. K., Zheng, B., Rogers, R. M., Sciurba, F. C., Perez, A., Chapman, B. E., Patel, S., Fuhrman, C. R., and Gur, D. (2003). Automated lung segmentation in x-ray computed tomography: development and evaluation of a heuristic threshold-based scheme1. Academic radiology, 10(11):1224–1236. [Cited on pages 42 and 43.]
- Lee, H.-L., Ryu, J. H., Wittmer, M. H., Hartman, T. E., Lymp, J. F., Tazelaar, H. D., and Limper, A. H. (2005). Familial idiopathic pulmonary fibrosis: clinical features and outcome. Chest, 127(6):2034–2041. [Cited on page 12.]
- Lee, S., Wolberg, G., and Shin, S. Y. (1997). Scattered data interpolation with multilevel b-splines. IEEE transactions on visualization and computer graphics, 3(3):228–244. [Cited on pages 72 and 89.]

- Lettieri, C. J., Nathan, S. D., Barnett, S. D., Ahmad, S., and Shorr, A. F. (2006). Prevalence and outcomes of pulmonary arterial hypertension in advanced idiopathic pulmonary fibrosis. *Chest*, 129(3):746–752. [Cited on pages 19, 20, and 23.]
- Leung, A. N. (1999). Pulmonary tuberculosis: the essentials. *Radiology*, 210(2):307–322. [Cited on page 38.]
- Ley, B., Collard, H. R., and King Jr, T. E. (2011). Clinical course and prediction of survival in idiopathic pulmonary fibrosis. *American journal of respiratory and critical care medicine*, 183(4):431–440. [Cited on pages xii, 19, 20, and 21.]
- Ley-Zaporozhan, J., Ley, S., Weinheimer, O., Iliyushenko, S., Erdugan, S., Eberhardt, R., Fuxa, A., Mews, J., and Kauczor, H.-U. (2008). Quantitative analysis of emphysema in 3d using mdct: influence of different reconstruction algorithms. *European journal of radiology*, 65(2):228–234. [Cited on page 38.]
- Li, Q., Sone, S., et al. (2003). Selective enhancement filters for nodules, vessels, and airway walls in two-and three-dimensional ct scans. *Medical physics*, 30(8):2040–2051. [Cited on page 66.]
- Lin, H. and Jiang, S. (2015). Combined pulmonary fibrosis and emphysema (cpfe): an entity different from emphysema or pulmonary fibrosis alone. *Journal of thoracic disease*, 7(4):767. [Cited on pages 22 and 38.]
- Lorenz, C., Carlsen, I.-C., Buzug, T. M., Fassnacht, C., and Weese, J. (1997). Multi-scale line segmentation with automatic estimation of width, contrast and tangential direction in 2d and 3d medical images. In *CVRMed-MRCAS'97*, pages 233–242. Springer. [Cited on pages 65 and 66.]
- Lynch, J. P., Saggar, R., Weigt, S. S., Zisman, D. A., and White, E. S. (2006). Usual interstitial pneumonia. In *Seminars in respiratory and critical care medicine*, vol-

- ume 27, pages 634–651. Copyright© 2006 by Thieme Medical Publishers, Inc., 333 Seventh Avenue, New York, NY 10001, USA. [Cited on page 18.]
- Martinez, F. J., Collard, H. R., Pardo, A., Raghu, G., Richeldi, L., Selman, M., Swigris, J. J., Taniguchi, H., and Wells, A. U. (2017). Idiopathic pulmonary fibrosis. *Nature Reviews Disease Primers*, 3:17074. [Cited on pages xi, 8, 15, 21, and 22.]
- Martinez, F. J. and Flaherty, K. (2006). Pulmonary function testing in idiopathic interstitial pneumonias. *Proceedings of the American Thoracic Society*, 3(4):315–321. [Cited on page 27.]
- Mejía, M., Carrillo, G., Rojas-Serrano, J., Estrada, A., Suárez, T., Alonso, D., Barrientos, E., Gaxiola, M., Navarro, C., and Selman, M. (2009). Idiopathic pulmonary fibrosis and emphysema: decreased survival associated with severe pulmonary arterial hypertension. *Chest*, 136(1):10–15. [Cited on pages 19, 22, and 23.]
- Meltzer, E. B. and Noble, P. W. (2008). Idiopathic pulmonary fibrosis. *Orphanet journal of rare diseases*, 3(1):8. [Cited on pages 1, 7, 8, 9, 10, 11, 19, 20, and 22.]
- Miki, K., Maekura, R., Hiraga, T., Hashimoto, H., Kitada, S., Miki, M., Yoshimura, K., Tateishi, Y., Fushitani, K., and Motone, M. (2009). Acidosis and raised norepinephrine levels are associated with exercise dyspnoea in idiopathic pulmonary fibrosis. *Respirology*, 14(7):1020–1026. [Cited on page 30.]
- Mura, M., Zompatori, M., Pacilli, A. M. G., Fasano, L., Schiavina, M., and Fabbri, M. (2006). The presence of emphysema further impairs physiologic function in patients with idiopathic pulmonary fibrosis. *Respiratory care*, 51(3):257–265. [Cited on page 27.]
- Musk, A., Zilko, P., Manners, P., Kay, P., and Kamboh, M. (1986). Genetic studies in familial fibrosing alveolitis: possible linkage with immunoglobulin allotypes (gm). *Chest*, 89(2):206–210. [Cited on page 12.]

- Nadrous, H. F., Pellikka, P. A., Krowka, M. J., Swanson, K. L., et al. (2005). The impact of pulmonary hypertension on survival in patients with idiopathic pulmonary fibrosis. *Chest*, 128(6):616S. [Cited on page 23.]
- Naidich, D. P. (2005). Imaging of the airways: functional and radiologic correlations. *Lippincott Williams & Wilkins*. [Cited on page 38.]
- Nava, S. and Rubini, F. (1999). Lung and chest wall mechanics in ventilated patients with end stage idiopathic pulmonary fibrosis. *Thorax*, 54(5):390–395. [Cited on page 26.]
- Nicholson, A. G., Colby, T. V., Dubois, R. M., Hansell, D. M., and Wells, A. U. (2000). The prognostic significance of the histologic pattern of interstitial pneumonia in patients presenting with the clinical entity of cryptogenic fibrosing alveolitis. *American journal of respiratory and critical care medicine*, 162(6):2213–2217. [Cited on page 19.]
- Nishimura, K., Kitaichi, M., Izumi, T., Nagai, S., Kanaoka, M., and Itoh, H. (1992). Usual interstitial pneumonia: histologic correlation with high-resolution ct. *Radiology*, 182(2):337–342. [Cited on page 14.]
- Ochs, R. A., Goldin, J. G., Abtin, F., Kim, H. J., Brown, K., Batra, P., Roback, D., McNitt-Gray, M. F., and Brown, M. S. (2007). Automated classification of lung bronchovascular anatomy in ct using adaboost. *Medical image analysis*, 11(3):315–324. [Cited on pages 48, 51, and 52.]
- Okada, T., Shimada, R., Hori, M., Nakamoto, M., Chen, Y.-W., Nakamura, H., and Sato, Y. (2008). Automated segmentation of the liver from 3d ct images using probabilistic atlas and multilevel statistical shape model. *Academic radiology*, 15(11):1390–1403. [Cited on page 56.]

- Orens, J. B., Kazerooni, E. A., Martinez, F. J., Curtis, J. L., Gross, B. H., Flint, A., and Lynch III, J. P. (1995). The sensitivity of high-resolution ct in detecting idiopathic pulmonary fibrosis proved by open lung biopsy: a prospective study. *Chest*, 108(1):109–115. [Cited on page 26.]
- Organ, L., Bacci, B., Koumoundouros, E., Barcham, G., Milne, M., Kimpton, W., Samuel, C., and Snibson, K. (2015). Structural and functional correlations in a large animal model of bleomycin-induced pulmonary fibrosis. *BMC pulmonary medicine*, 15(1):81. [Cited on page 26.]
- Parambil, J. G., Myers, J. L., and Ryu, J. H. (2005). Histopathologic features and outcome of patients with acute exacerbation of idiopathic pulmonary fibrosis undergoing surgical lung biopsy. *Chest*, 128(5):3310–3315. [Cited on page 20.]
- Pastre, J., Plantier, L., Planes, C., Borie, R., Nunes, H., Delclaux, C., and Israël-Biet, D. (2015). Different k_{co} and va combinations exist for the same dl_{co} value in patients with diffuse parenchymal lung diseases. *BMC pulmonary medicine*, 15(1):100. [Cited on pages 27 and 30.]
- Plantier, L., Cazes, A., Dinh-Xuan, A.-T., Bancal, C., Marchand-Adam, S., and Crestani, B. (2018). Physiology of the lung in idiopathic pulmonary fibrosis. *European Respiratory Review*, 27(147):170062. [Cited on pages xix, 24, 25, 26, 27, 28, 29, 30, and 32.]
- Plantier, L., Debray, M.-P., Estellat, C., Flamant, M., Roy, C., Bancal, C., Borie, R., Israël-Biet, D., Mal, H., Crestani, B., et al. (2016). Increased volume of conducting airways in idiopathic pulmonary fibrosis is independent of disease severity: a volumetric capnography study. *Journal of breath research*, 10(1):016005. [Cited on pages 27, 28, and 30.]

- Prasad, M. N., Brown, M. S., Ahmad, S., Abtin, F., Allen, J., da Costa, I., Kim, H. J., McNitt-Gray, M. F., and Goldin, J. G. (2008). Automatic segmentation of lung parenchyma in the presence of diseases based on curvature of ribs. *Academic radiology*, 15(9):1173–1180. [Cited on pages 42, 45, and 46.]
- Pu, J., Leader, J. K., Zheng, B., Knollmann, F., Fuhrman, C., Sciurba, F. C., and Gur, D. (2009a). A computational geometry approach to automated pulmonary fissure segmentation in ct examinations. *IEEE transactions on medical imaging*, 28(5):710–719. [Cited on pages 39, 41, and 49.]
- Pu, J., Paik, D. S., Meng, X., Roos, J., and Rubin, G. D. (2011). Shape “break-and-repair” strategy and its application to automated medical image segmentation. *IEEE transactions on visualization and computer graphics*, 17(1):115–124. [Cited on pages 42, 45, and 46.]
- Pu, J., Roos, J., Chin, A. Y., Napel, S., Rubin, G. D., and Paik, D. S. (2008). Adaptive border marching algorithm: automatic lung segmentation on chest ct images. *Computerized Medical Imaging and Graphics*, 32(6):452–462. [Cited on pages 40, 42, and 45.]
- Pu, J., Zheng, B., Leader, J. K., Fuhrman, C., Knollmann, F., Klym, A., and Gur, D. (2009b). Pulmonary lobe segmentation in ct examinations using implicit surface fitting. *IEEE transactions on medical imaging*, 28(12):1986–1996. [Cited on pages 82 and 91.]
- Quadrelli, S., Molinari, L., Ciallella, L., Spina, J. C., Sobrino, E., and Chertcoff, J. (2010). Radiological versus histopathological diagnosis of usual interstitial pneumonia in the clinical practice: does it have any survival difference? *Respiration*, 79(1):32–37. [Cited on page 17.]

- Raghu, G. (1987). Idiopathic pulmonary fibrosis: a rational clinical approach. *Chest*, 92(1):148–154. [Cited on page 19.]
- Raghu, G., Amatto, V. C., Behr, J., and Stowasser, S. (2015). Comorbidities in idiopathic pulmonary fibrosis patients: a systematic literature review. *European Respiratory Journal*, 46(4):1113–1130. [Cited on page 22.]
- Raghu, G., Collard, H. R., Egan, J. J., Martinez, F. J., Behr, J., Brown, K. K., Colby, T. V., Cordier, J.-F., Flaherty, K. R., Lasky, J. A., et al. (2011). An official ATS/ERS/JRS/ALAT statement: idiopathic pulmonary fibrosis: evidence-based guidelines for diagnosis and management. *American journal of respiratory and critical care medicine*, 183(6):788–824. [Cited on pages xii, 1, 2, 7, 8, 10, 11, 12, 13, 14, 15, 16, 17, 18, 19, 20, 21, 23, and 24.]
- Raghu, G., Mageto, Y. N., Lockhart, D., Schmidt, R. A., Wood, D. E., and Godwin, J. D. (1999). The accuracy of the clinical diagnosis of new-onset idiopathic pulmonary fibrosis and other interstitial lung disease: a prospective study. *Chest*, 116(5):1168–1174. [Cited on page 17.]
- Raghu, G., Weycker, D., Edelsberg, J., Bradford, W. Z., and Oster, G. (2006). Incidence and prevalence of idiopathic pulmonary fibrosis. *American journal of respiratory and critical care medicine*, 174(7):810–816. [Cited on pages 10 and 14.]
- Rees, D. and Murray, J. (2007). Silica, silicosis and tuberculosis [state of the art series. occupational lung disease in high-and low-income countries, edited by m. chan-yeung. number 4 in the series]. *The International Journal of Tuberculosis and Lung Disease*, 11(5):474–484. [Cited on page 38.]
- Renzi, G., Milic-Emili, J., and Grassino, A. (1982). The pattern of breathing in diffuse lung fibrosis. *Bulletin europeen de physiopathologie respiratoire*, 18(3):461–472. [Cited on page 28.]

- Richeldi, L., Collard, H. R., and Jones, M. G. (2017). Idiopathic pulmonary fibrosis. *The Lancet*, 389(10082):1941–1952. [Cited on pages 1, 2, 8, 10, 11, 12, 13, 14, 15, and 16.]
- Rohlf, F. J. (1999). Shape statistics: Procrustes superimpositions and tangent spaces. *Journal of Classification*, 16(2):197–223. [Cited on page 59.]
- Rosenberg, E. (1996). The 1995 update of recommendations for a standard technique for measuring the single-breath carbon monoxide diffusing capacity (transfer factor). *American journal of respiratory and critical care medicine*, 154(3):827–828. [Cited on page 29.]
- Ross, J. C., Estépar, R. S. J., Kindlmann, G., Díaz, A., Westin, C.-F., Silverman, E. K., and Washko, G. R. (2010). Automatic lung lobe segmentation using particles, thin plate splines, and maximum a posteriori estimation. In *International Conference on Medical Image Computing and Computer-Assisted Intervention*, pages 163–171. Springer. [Cited on pages 48, 51, and 52.]
- Ross, J. C., Kindlmann, G. L., Okajima, Y., Hatabu, H., Díaz, A. A., Silverman, E. K., Washko, G. R., Dy, J., and Estépar, R. S. J. (2013). Pulmonary lobe segmentation based on ridge surface sampling and shape model fitting. *Medical physics*, 40(12). [Cited on pages 48 and 52.]
- Rudd, R. M., Prescott, R. J., Chalmers, J., and Johnston, I. D. (2007). British thoracic society study on cryptogenic fibrosing alveolitis: response to treatment and survival. *Thorax*, 62(1):62–66. [Cited on page 19.]
- Ryu, J. H., Moua, T., Daniels, C. E., Hartman, T. E., Eunhee, S. Y., Utz, J. P., and Limper, A. H. (2014). Idiopathic pulmonary fibrosis: evolving concepts. In *Mayo Clinic proceedings*, volume 89, pages 1130–1142. Elsevier. [Cited on pages 19 and 20.]

- Saita, S., Kubo, M., Kawata, Y., Niki, N., Ohmatsu, H., and Moriyama, N. (2006). An algorithm for the extraction of pulmonary fissures from low-dose multislice ct image. *Systems and Computers in Japan*, 37(9):63–76. [Cited on pages 48, 49, and 51.]
- Sakamoto, K., Taniguchi, H., Kondoh, Y., Ono, K., Hasegawa, Y., and Kitaichi, M. (2009). Acute exacerbation of idiopathic pulmonary fibrosis as the initial presentation of the disease. *European Respiratory Review*, 18(112):129–132. [Cited on page 20.]
- Schmidt, R., Meier, U., Markart, P., Grimminger, F., Velcovsky, H., Morr, H., Seeger, W., and Gunther, A. (2002). Altered fatty acid composition of lung surfactant phospholipids in interstitial lung disease. *American Journal of Physiology-Lung Cellular and Molecular Physiology*, 283(5):L1079–L1085. [Cited on page 24.]
- Seibold, M. A., Wise, A. L., Speer, M. C., Steele, M. P., Brown, K. K., Loyd, J. E., Fingerlin, T. E., Zhang, W., Gudmundsson, G., Groshong, S. D., et al. (2011). A common muc5b promoter polymorphism and pulmonary fibrosis. *New England Journal of Medicine*, 364(16):1503–1512. [Cited on page 12.]
- Selman, M., Carrillo, G., Estrada, A., Mejia, M., Becerril, C., Cisneros, J., Gaxiola, M., Pérez-Padilla, R., Navarro, C., Richards, T., et al. (2007). Accelerated variant of idiopathic pulmonary fibrosis: clinical behavior and gene expression pattern. *PloS one*, 2(5):e482. [Cited on page 19.]
- Shikata, H., McLennan, G., Hoffman, E. A., and Sonka, M. (2009). Segmentation of pulmonary vascular trees from thoracic 3d ct images. *Journal of Biomedical Imaging*, 2009:24. [Cited on page 38.]
- Silva, C. I. S., Muller, N. L., Lynch, D. A., Curran-Everett, D., Brown, K. K., Lee, K. S., Chung, M. P., and Churg, A. (2008a). Chronic hypersensitivity pneumonitis: differentiation from idiopathic pulmonary fibrosis and nonspecific interstitial pneumonia by using thin-section ct. *Radiology*, 246(1):288–297. [Cited on page 18.]

- Silva, D. R., Gazzana, M. B., Barreto, S. S. M., and Knorst, M. M. (2008b). Idiopathic pulmonary fibrosis and emphysema in smokers. *Jornal Brasileiro de Pneumologia*, 34(10):779–786. [Cited on page 22.]
- Sluimer, I., Prokop, M., and Van Ginneken, B. (2005). Toward automated segmentation of the pathological lung in ct. *IEEE transactions on medical imaging*, 24(8):1025–1038. [Cited on page 45.]
- Society, A. T. et al. (2000). Idiopathic pulmonary fibrosis: diagnosis and treatment: international consensus statement. *Am J Respir Crit Care Med*, 161:646–664. [Cited on pages 16, 24, 26, 28, 29, 31, and 32.]
- Souza, C. A., Muller, N. L., Lee, K. S., Johkoh, T., Mitsuhiro, H., and Chong, S. (2006). Idiopathic interstitial pneumonias: prevalence of mediastinal lymph node enlargement in 206 patients. *American Journal of Roentgenology*, 186(4):995–999. [Cited on page 14.]
- Steele, M. P., Speer, M. C., Loyd, J. E., Brown, K. K., Herron, A., Slifer, S. H., Burch, L. H., Wahidi, M. M., Phillips III, J. A., Sporn, T. A., et al. (2005). Clinical and pathologic features of familial interstitial pneumonia. *American journal of respiratory and critical care medicine*, 172(9):1146–1152. [Cited on page 12.]
- Stegmann, M. B. and Gomez, D. D. (2002). A brief introduction to statistical shape analysis. *Informatics and mathematical modelling*, Technical University of Denmark, DTU, 15(11). [Cited on page 56.]
- Strickland, N., Hughes, J., Hart, D., Myers, M., and Lavender, J. (1993). Cause of regional ventilation-perfusion mismatching in patients with idiopathic pulmonary fibrosis: a combined ct and scintigraphic study. *AJR. American journal of roentgenology*, 161(4):719–725. [Cited on pages 30 and 31.]

- Styner, M., Gerig, G., Lieberman, J., Jones, D., and Weinberger, D. (2003). Statistical shape analysis of neuroanatomical structures based on medial models. *Medical image analysis*, 7(3):207–220. [Cited on page 56.]
- Sumikawa, H., Johkoh, T., Colby, T. V., Ichikado, K., Suga, M., Taniguchi, H., Kondoh, Y., Ogura, T., Arakawa, H., Fujimoto, K., et al. (2008). Computed tomography findings in pathological usual interstitial pneumonia: relationship to survival. *American journal of respiratory and critical care medicine*, 177(4):433–439. [Cited on page 28.]
- Sun, S., Bauer, C., and Beichel, R. (2012). Automated 3-d segmentation of lungs with lung cancer in ct data using a novel robust active shape model approach. *IEEE transactions on medical imaging*, 31(2):449–460. [Cited on pages 42, 45, and 47.]
- Sun, X., Zhang, H., and Duan, H. (2006). 3d computerized segmentation of lung volume with computed tomography. *Academic radiology*, 13(6):670–677. [Cited on pages 40, 42, 43, and 44.]
- Swigris, J. J., Han, M., Vij, R., Noth, I., Eisenstein, E. L., Anstrom, K. J., Brown, K. K., and Fairclough, D. (2012). The ucsd shortness of breath questionnaire has longitudinal construct validity in idiopathic pulmonary fibrosis. *Respiratory medicine*, 106(10):1447–1455. [Cited on page 30.]
- Taskar, V. S. and Coultas, D. B. (2006). Is idiopathic pulmonary fibrosis an environmental disease? *Proceedings of the American Thoracic Society*, 3(4):293–298. [Cited on page 11.]
- Tawhai, M. H. and Burrowes, K. S. (2003). Developing integrative computational models of pulmonary structure. *The Anatomical Record*, 275(1):207–218. [Cited on page 59.]
- Taylor, C., Cootes, T., Hill, A., and Haslam, J. (1995). Medical image segmentation

- using active shape models. *STUDIES IN HEALTH TECHNOLOGY AND INFORMATICS*, 19:121–144. [Cited on page 56.]
- Trahan, S., Hanak, V., Ryu, J. H., and Myers, J. L. (2008). Role of surgical lung biopsy in separating chronic hypersensitivity pneumonia from usual interstitial pneumonia/idiopathic pulmonary fibrosis*: Analysis of 31 biopsies from 15 patients. *Chest*, 134(1):126–132. [Cited on page 18.]
- Travis, W. D., Costabel, U., Hansell, D. M., King Jr, T. E., Lynch, D. A., Nicholson, A. G., Ryerson, C. J., Ryu, J. H., Selman, M., Wells, A. U., et al. (2013). An official american thoracic society/european respiratory society statement: update of the international multidisciplinary classification of the idiopathic interstitial pneumonias. *American journal of respiratory and critical care medicine*, 188(6):733–748. [Cited on page 10.]
- Travis, W. D., King, T. E., Bateman, E. D., Lynch, D. A., Capron, F., Center, D., Colby, T. V., Cordier, J. F., DuBois, R. M., Galvin, J., et al. (2002). American thoracic society/european respiratory society international multidisciplinary consensus classification of the idiopathic interstitial pneumonias. *American journal of respiratory and critical care medicine*, 165(2):277–304. [Cited on page 16.]
- Troy, L. and Corte, T. J. (2012). Management of the idiopathic interstitial pneumonias. *Australian Prescriber*, 35(6):202–6. [Cited on pages xi and 9.]
- Tsai, A., Yezzi, A., Wells, W., Tempany, C., Tucker, D., Fan, A., Grimson, W. E., and Willsky, A. (2003). A shape-based approach to the segmentation of medical imagery using level sets. *IEEE transactions on medical imaging*, 22(2):137–154. [Cited on page 56.]
- Tukiainen, P., Taskinen, E., Holsti, P., Korhola, O., and Valle, M. (1983). Prognosis of cryptogenic fibrosing alveolitis. *Thorax*, 38(5):349–355. [Cited on page 19.]

- Ukil, S. and Reinhardt, J. M. (2005). Smoothing lung segmentation surfaces in three-dimensional x-ray ct images using anatomic guidance1. *Academic radiology*, 12(12):1502–1511. [Cited on pages 40, 42, 43, and 55.]
- Ukil, S. and Reinhardt, J. M. (2009). Anatomy-guided lung lobe segmentation in x-ray ct images. *IEEE transactions on medical imaging*, 28(2):202–214. [Cited on pages xiii, xiv, 35, 36, 39, 40, 41, 48, 49, 50, and 82.]
- van Rikxoort, E. M., de Hoop, B., Viergever, M. A., Prokop, M., and van Ginneken, B. (2009). Automatic lung segmentation from thoracic computed tomography scans using a hybrid approach with error detection. *Medical physics*, 36(7):2934–2947. [Cited on page 45.]
- Van Rikxoort, E. M. and Van Ginneken, B. (2013). Automated segmentation of pulmonary structures in thoracic computed tomography scans: a review. *Physics in medicine and biology*, 58(17):R187. [Cited on pages xiv, 39, 40, 41, and 45.]
- van Rikxoort, E. M., van Ginneken, B., Klik, M., and Prokop, M. (2008). Supervised enhancement filters: Application to fissure detection in chest ct scans. *IEEE Transactions on Medical Imaging*, 27(1):1–10. [Cited on pages 48, 51, and 52.]
- Vuorinen, K., Ohlmeier, S., Leppäranta, O., Salmenkivi, K., Myllärniemi, M., and Kinula, V. L. (2008). Peroxiredoxin ii expression and its association with oxidative stress and cell proliferation in human idiopathic pulmonary fibrosis. *Journal of Histochemistry & Cytochemistry*, 56(10):951–959. [Cited on page 27.]
- Wagner, P., Dantzker, D., Dueck, R., De Polo, J., Wasserman, K., and West, J. (1976). Distribution of ventilation-perfusion ratios in patients with interstitial lung disease. *Chest*, 69(2):256–257. [Cited on pages 31 and 32.]
- Wallaert, B., Wemeau-Stervinou, L., Salleron, J., Tillie-Leblond, I., and Perez, T.

- (2012). Do we need exercise tests to detect gas exchange impairment in fibrotic idiopathic interstitial pneumonias? *Pulmonary medicine*, 2012. [Cited on page 30.]
- Walsh, S. L., Wells, A. U., Sverzellati, N., Devaraj, A., von der Thüsen, J., Yousem, S. A., Colby, T. V., Nicholson, A. G., and Hansell, D. M. (2015). Relationship between fibroblastic foci profusion and high resolution ct morphology in fibrotic lung disease. *BMC medicine*, 13(1):241. [Cited on page 28.]
- Wang, J., Betke, M., and Ko, J. P. (2004). Shape-based curve growing model and adaptive regularization for pulmonary fissure segmentation in ct. In *International Conference on Medical Image Computing and Computer-Assisted Intervention*, pages 541–548. Springer. [Cited on pages 48 and 51.]
- Wang, J., Betke, M., and Ko, J. P. (2006). Pulmonary fissure segmentation on ct. *Medical Image Analysis*, 10(4):530–547. [Cited on pages 48 and 51.]
- Wang, J., Li, F., and Li, Q. (2009). Automated segmentation of lungs with severe interstitial lung disease in ct. *Medical physics*, 36(10):4592–4599. [Cited on pages 40, 42, 45, and 46.]
- Wasserman, K. and Whipp, B. J. (1975). Exercise physiology in health and disease. *American Review of Respiratory Disease*, 112(2):219–249. [Cited on page 31.]
- Wei, Q., Hu, Y., Gelfand, G., and Macgregor, J. H. (2009). Segmentation of lung lobes in high-resolution isotropic ct images. *IEEE Transactions on biomedical engineering*, 56(5):1383–1393. [Cited on page 82.]
- Wells, A. U., Desai, S. R., Rubens, M. B., Goh, N. S., Cramer, D., Nicholson, A. G., Colby, T. V., Du Bois, R. M., and Hansell, D. M. (2003). Idiopathic pulmonary fibrosis: a composite physiologic index derived from disease extent observed by computed tomography. *American journal of respiratory and critical care medicine*, 167(7):962–969. [Cited on pages 19 and 22.]

- Wells, A. U., King, A. D., Rubens, M. B., Cramer, D., Du Bois, R., and Hansell, D. M. (1997). Lone cryptogenic fibrosing alveolitis: a functional-morphologic correlation based on extent of disease on thin-section computed tomography. *American journal of respiratory and critical care medicine*, 155(4):1367–1375. [Cited on pages 22 and 30.]
- Wiemker, R., Bülow, T., and Blaffert, T. (2005). Unsupervised extraction of the pulmonary interlobar fissures from high resolution thoracic ct data. In *International Congress Series*, volume 1281, pages 1121–1126. Elsevier. [Cited on pages 48, 51, and 52.]
- Wootton, S. C., Kim, D. S., Kondoh, Y., Chen, E., Lee, J. S., Song, J. W., Huh, J. W., Taniguchi, H., Chiu, C., Boushey, H., et al. (2011). Viral infection in acute exacerbation of idiopathic pulmonary fibrosis. *American journal of respiratory and critical care medicine*, 183(12):1698–1702. [Cited on page 20.]
- Xaubet, A., Ancochea, J., and Molina-Molina, M. (2017). Idiopathic pulmonary fibrosis. *Medicina Clínica (English Edition)*, 148(4):170–175. [Cited on pages 2, 8, 10, 11, 12, 19, 21, 22, and 23.]
- Yamamoto, T., Kabus, S., Klinder, T., Lorenz, C., Von Berg, J., Blaffert, T., Loo Jr, B. W., and Keall, P. J. (2011). Investigation of four-dimensional computed tomography-based pulmonary ventilation imaging in patients with emphysematous lung regions. *Physics in medicine and biology*, 56(7):2279. [Cited on page 38.]
- Zhang, J. (2013). Development of an automated system for building a large population-based statistical model of femur morphology. PhD thesis, ResearchSpace@ Auckland. [Cited on page 56.]
- Zhang, L., Hoffman, E. A., and Reinhardt, J. M. (2006). Atlas-driven lung lobe segmentation in volumetric x-ray ct images. *IEEE transactions on medical imaging*, 25(1):1–16. [Cited on page 49.]

- Zhang, X., Smith, N., and Webb, A. (2011). Medical imaging. In Feng, D. D., editor, Biomedical Information Technology. Elsevier Science, Oxford. [Cited on page 37.]
- Zhou, X., Hayashi, T., Hara, T., Fujita, H., Yokoyama, R., Kiryu, T., and Hoshi, H. (2004). Automatic recognition of lung lobes and fissures from multislice ct images. In Proceedings of SPIE, volume 5370, pages 1629–1633. [Cited on pages 48, 49, and 51.]
- Zhu, C., Qi, S., van Triest, H., Wang, S., Kang, Y., and Yue, Y. (2010). Automatic 3d segmentation of human airway tree in ct image. In Biomedical Engineering and Informatics (BMEI), 2010 3rd International Conference on, volume 1, pages 132–136. IEEE. [Cited on page 38.]
- Zielonka, T., Demkow, U., Radzikowska, E., Bialas, B., Filewska, M., Zycinska, K., Obrowski, M., Kowalski, J., Wardyn, K., and Skopinska-Rozewska, E. (2010). Angiogenic activity of sera from interstitial lung disease patients in relation to pulmonary function. European journal of medical research, 15(2):229. [Cited on page 26.]